Summer 8-15-2016

Continuum Nuclear Structure Of Light Nuclei

Kyle Wayne Brown
Washington University in St. Louis

WASHINGTON UNIVERSITY IN ST. LOUIS

Department of Chemistry

Dissertation Examination Committee:
Lee Sobotka, Chair
Robert Charity
Willem Dickhoff
Demetrios Sarantites
Jacob Schaefer

CONTINUUM NUCLEAR STRUCTURE OF LIGHT NUCLEI

by

Kyle Wayne Brown

A dissertation presented to the
Graduate School of Arts and Sciences
of Washington University in
partial fulfillment of the
requirements for the degree
of Doctor of Philosophy

August 19, 2016

Saint Louis, Missouri

Contents

List of Figures

List of Tables

Acknowledgments

First and foremost I would like to thank my outstanding advisor, Lee Sobotka, who made my time in graduate school both memorable and enjoyable. His guidance has enabled me to become the scientist I am today. I would also like to thank Bob Charity for being an excellent mentor. I am grateful to him for the use of his analysis and simulation codes which have been utilized heavily for this work. I would like to thank my committee for all of their hard work.

I am eternally grateful to my parents, Karla and Gary Brown, whose constant love and support has been the rock I needed to succeed.

I would like to thank the HiRA collaboration for their assistance during the two invariant-mass experiments in this work. In particular I would like to thank Zbigniew Chajecki, without whom the experiments would not have been possible. The assistance of Alexandra Gade and Dirk Wiesshaar on use of the CAESAR array was greatly appreciated. I would also like to thank the A1900 group at the NSCL for the production of the ^{9}C and ^{17}Ne secondary beams.

The detailed understanding of the $2p$ decay of ^{16}Ne would not have been possible without the calculations of Leonid Grigorenko. His insight and discussions were an integral part of this work. I would also like to thank Robert Wiringa for his calculations on the $A = 7$ isobar.

I would also like to thank my undergraduate advisor, Romualdo deSouza, and my mentor, Sylvie Hudan. They were essential in providing the training needed to succeed early on in my graduate studies.

Abstract

In this work, the continuum decay of proton-rich nuclei with mass number A $\leq$ 17 was studied. The nuclear structure of these nuclei was assessed by measuring the decay energy, width, and momentum correlations between the decay fragments. In particular the Isobaric Analog State in ^{8}B, the ground-state and excited states of ^{16}Ne, the $T = 3/2$ states in the $A = 7$ isobaric chain, and the excited states of ^{9}C and ^{17}Ne were all studied. In addition a first measurement of ^{17}Na was made. These states decay by emission of 1 or more protons and were populated through knockout reactions or inelastic scattering of ^{9}C and ^{17}Ne secondary beams produced at the National Superconducting Cyclotron Laboratory. The charged particles were detected in the High Resolution Array (HiRA) which, in these studies, consisted of 14 Si-CsI(Tl) telescopes. Gamma rays measured in coincidence with charged particles were measured in the 4π array of CsI(Na) called CAESAR.

Chapter 1

Introduction

1.1 Nuclear Stability

The chart of nuclides, Fig. 1.1, is a plot of all known nuclei. Nuclei are displayed according to their number of protons (p) and neutrons (n), with proton number (Z) plotted along the vertical axis and neutron number (N) plotted along the horizontal axis. The stable nuclei, shown as black squares in Fig. 1.1, have roughly equal numbers of protons and neutrons for low mass number (A = N+Z) nuclei, and the highest mass stable nuclei have roughly 40 % protons. This is due to the competition between the increasing Coulomb interaction between protons, that drives stability towards neutron-rich nuclei and the nuclear asymmetry energy

$$E_{asy} \propto C\frac{(N-Z)^2}{A} \tag{1.1}$$

that drives stability towards N = Z. Off the line of stability are radioactive nuclei that can be accessed via nuclear reactions. In general, as one moves away from stability along isotopes (same Z) or isotones (same N) the beta-decay half-lives become shorter (blue and pink squares of Fig. 1.1). The binding energy of the last neutron or proton also decreases as one moves towards neutron-rich or neutron-deficient nuclei, respectively. At some point the binding energy of the last proton or neutron goes to zero, this is referred to as the drip-line.

Nuclei beyond the drip lines exist only as short-lived resonances, and will decay by emission of one or more nucleons (orange and purple squares). At the high mass end of the chart of nuclides are nuclei which decay either by alpha emission or spontaneous fission (yellow and green squares), which are not the subject of this work.

Nuclei with half-lives much shorter than the age of the earth that are not still being produced through some physical process today (i.e. alpha decay chains or atmospheric production), must be created in the laboratory. Knockout and transfer reactions allow us to study nuclei one or a few nucleons from stability. Nuclei further from stability can be produced by fusion or fragmentation reactions or as the products of fission. Due to the decreasing slope of the line of stability, fusion and fission allow us to study neutron-deficient and neutron-rich species, respectively. Fragmentation reactions allow for a much wider range in asymmetry (n/p ratio), but can only be used to study nuclei with mass less than the nucleus being fragmented. Nuclei very far from stability, often called exotic nuclei, are very difficult to produce. The most exotic are those nuclei near or beyond the proton and neutron drip lines. These unstable nuclei can be very short lived (nanoseconds or shorter). Measuring the properties of these nuclei (half-lives, decay modes) plays an important role in our understanding of element production in the universe as nucleosynthesis often progresses through these unstable configurations of neutrons and protons. To produce these nuclei in the laboratory one can use a two-step process. The first step could be fragmentation to produce nuclei which are a few nucleons from stability, with half-lives of milliseconds (particle bound but unstable to β decay), and then a second step (executed proximally to appropriately designed experimental equipment) to produce the very short-lived (particle-unbound) nucleus. This will be the method employed in the present work.

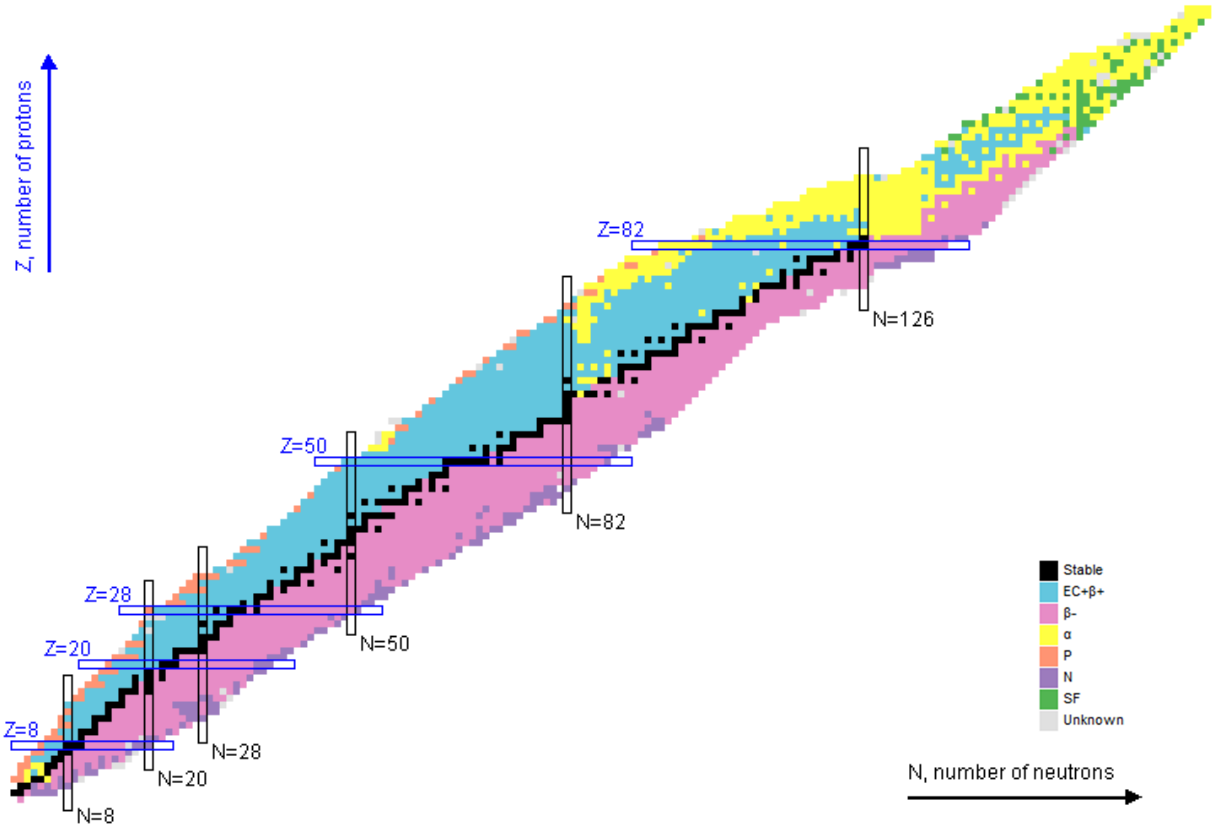

Figure 1.1: Chart of nuclides. Proton number increases towards the top of the figure, and neutron number increases towards the right. Stable nuclei are shown as black squares, and the radioactive nuclei are shown as colored squares, indicating their dominate mode of decay. Neutron and proton closed shells are indicated by the blue rectangles.

1.2 Nucleosynthesis

1.2.1 Big Bang

In the very earliest times in the universe, it was too hot for even protons or neutrons to exist. As the universe expanded and cooled, neutrons and protons formed and were in equilibrium through the following reactions,

$$\overline{\nu}_e + p \rightleftharpoons e^+ + n \tag{1.2}$$

$$\nu_e + n \rightleftharpoons e^- + p. \tag{1.3}$$

When the temperature drops to $T = 10^9$ K, the neutrinos decouple, and the neutrons and protons fall out of equilibrium. While neutrons will beta decay to protons, the half-life is long compared to the time-scale of Big Bang Nucleosynthesis (BBN). This allows neutron reactions to take place during BBN. Figure 1.2 shows the reaction network that takes place during BBN. The net result of this, the first act of nucleosynthesis, is about 75 % protons, 23 % ^{4}He, by mass, and trace amounts of other very light nuclei. The universe continues to expand and cool. When the temperature drops below that corresponding to the electron-proton binding energy (13.6 eV, or at t = 377000 years), electrons bind to make atoms and photons decouple and free stream. For nucleosynthesis the story pauses until the formation of stars.

1.2.2 Stellar

Nucleosynthesis in the modern universe can be broken into two classes, stellar and explosive. For all "main sequence" stars, like the sun, the dominant process is called the *pp*-chain (proton-proton chain). This process converts four protons into an alpha particle (^{4}He nucleus) through a series of reactions, and in the process releases 27 MeV of energy (The

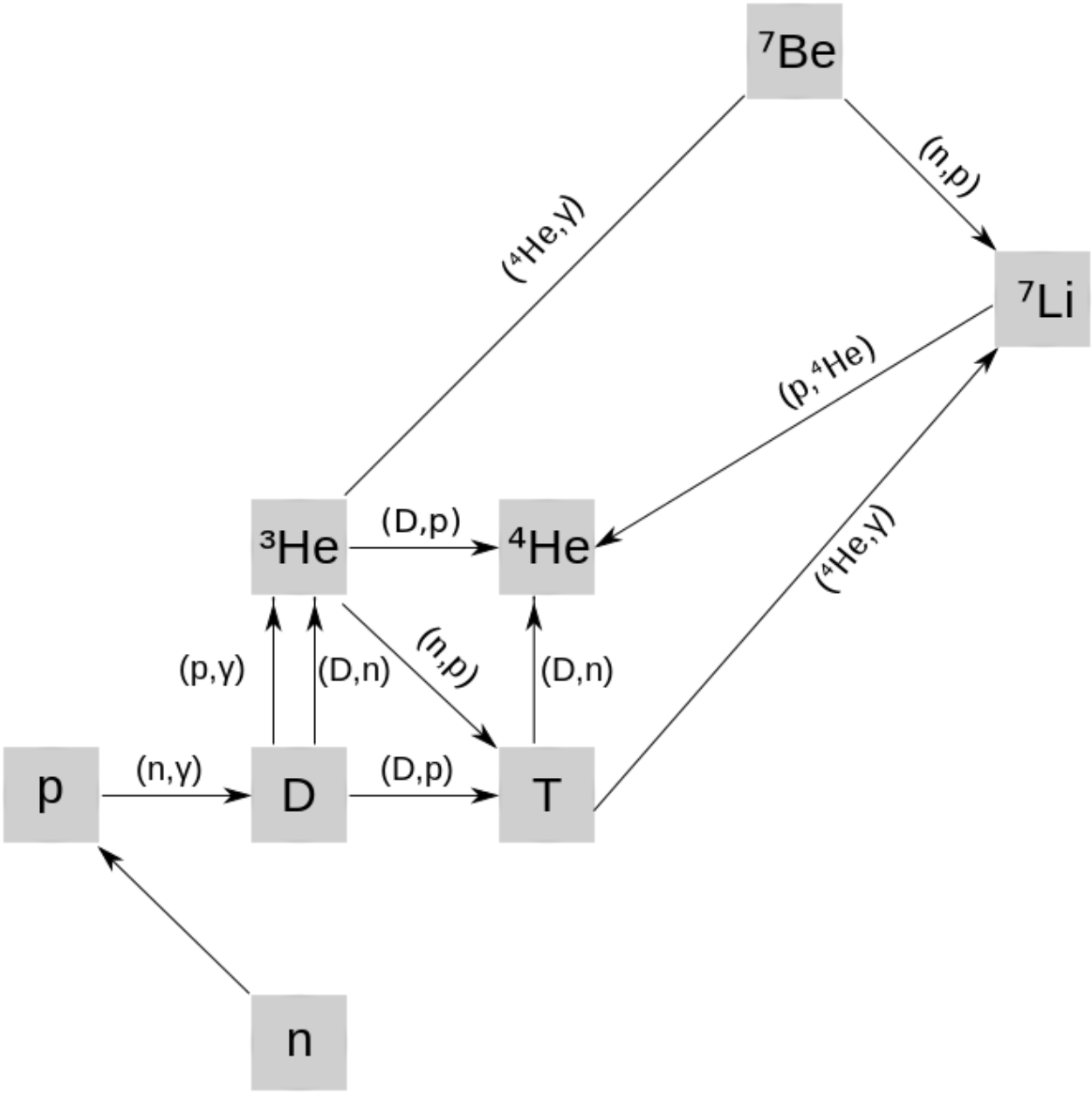

Figure 1.2: Big Bang Nucleosynthesis reaction network. All arrows are labeled by the reaction they represent. Initially only neutrons and protons exist, but deuterium (D) is made through the neutron capture reaction, p(n,γ)D. From there other reactions occur to produce: tritium (T), ^{3,4}He, ^{7}Be, ^{7}Li.

products have that much less mass/energy than the reactants). The net reaction is as follows:

$$4p \rightarrow\rightarrow\rightarrow\ {}^{4}\mathrm{He}^{++} + 2e^{+} + 2\nu + 26.73\ \mathrm{MeV}. \tag{1.4}$$

In stars heavier than the sun, this reaction proceeds through a process known as the CNO cycle. This is a catalytic process that uses ^{12}C "seed" nuclei, Fig. 1.3. This process produces intermediate nuclei such as ^{15}O, which in this cycle beta decays to ^{15}N. Before this happens, it can undergo a CNO breakout alpha capture reaction, $^{15}\mathrm{O}(\alpha,\gamma)^{19}\mathrm{Ne}$, which provides the seeds for the rp-process.

When a star begins to run out of hydrogen, the core of the star collapses and the temperature increases. This rise in temperature leads to the helium burning phase of a star's life, where three alphas come together to make ^{12}C. This is a two step process in which two alphas fuse to create ^{8}Be, which is unbound and will decay back to two alphas rapidly. However if another alpha particle encounters the ^{8}Be before it can decay, they can fuse to create ^{12}C in a special $J^{\pi} = 0^{+}$ excited state called the Holye state. Four times in 10,000 this state will decay by emitting two γ rays, de-exciting to the stable ^{12}C ground state. The rest of the time it will decay back to ^{8}Be and then back to 3α's. For lighter stars, this is the last stage of their productive lives. When the helium is exhausted, they blow off their outer layers to become white dwarfs. For more massive stars, the ^{12}C and the material produced from the CNO cycle can undergo a series of alpha capture reactions $\mathrm{E}^{A}_{Z}(\alpha,\gamma)\mathrm{E}^{A+4}_{Z+2}$ to produce nuclei on or near the line of stability. These reactions are all exothermic until the Fe-Ni region, at which point this process shuts off.

Moving beyond iron nuclei (in normal stellar life) requires a process known as the s-process, or the slow neutron-capture process. This process takes the seeds created from the alpha captures, and produces heavier nuclei through neutron capture, $\mathrm{E}^{A}_{Z}(\mathrm{n},\gamma)\mathrm{E}^{A+1}_{Z}$. The s-process is slow on the time scale of beta decay, so if these new nuclei are beta-unstable, they will decay before another neutron-capture reaction can take place. Therefore only nuclei

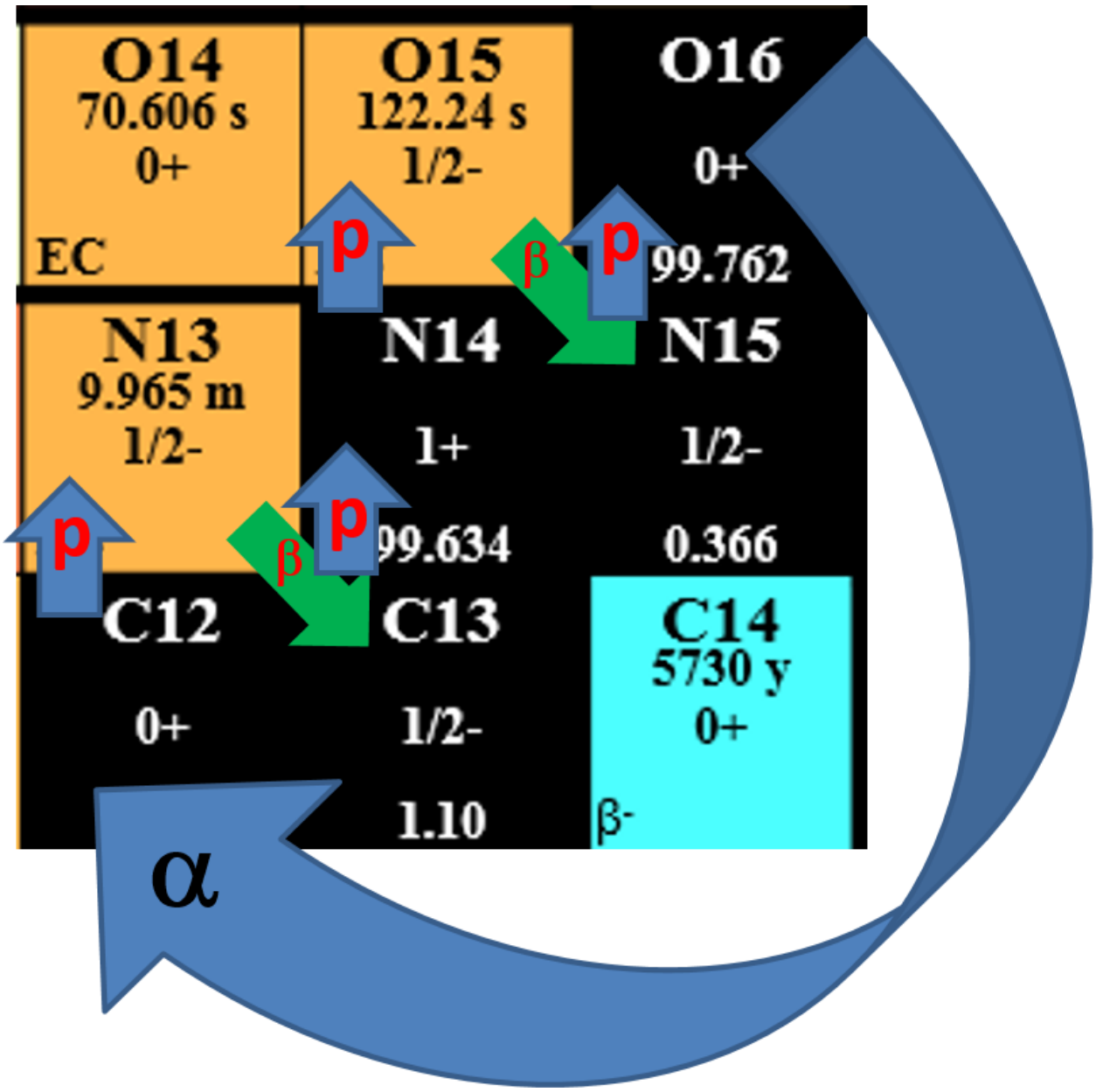

Figure 1.3: Carbon-Nitrogen-Oxygen cycle. The ^{12}C acts as a catalyst to the same net reaction as in the pp-chain. While this process is occurring in stars, 5 carbon, nitrogen and oxygen isotopes are present and available for other nucleosynthetic processes (i.e. alpha capture).

right along the line of stability can be created by this method. The neutron-capture reactions require the presence of free neutrons, which have long since decayed from the time of BBN. Active stars can produce free neutrons from

$$^{13}C(\alpha, n)^{16}O \quad and \quad ^{22}Ne(\alpha, n)^{25}Mg. \tag{1.5}$$

This is the final process which can occur in stars during their normal quasi-stationary life. For further production of heavy nuclei, and nuclei which the s-process cannot produce, more explosive environments are required.

1.2.3 Exotic Processes

There are two main pathways for explosive nucleosynthesis, namely the r-process and the rp-process. The r-process, or rapid-neutron capture process, has inverted kinetics to that of the s-process. Here the neutron captures occur rapidly enough that the beta-unstable nuclei created by this process cannot decay before they themselves undergo neutron capture. For a large neutron-flux, nuclei almost out to the drip line will be produced. This process is retarded when a closed shell is hit as the capture cross-section drops dramatically. While the site of the r-process is not known experimentally, it is thought to be an explosive event like a supernova or neutron-star merger. In both of these astrophysical events, the neutron flux is high enough for this process to occur. When the event is over and the neutron flux dies down, the nuclei created by this process will beta-decay back along an isobar, constant A = N + Z, to the line of stability. The r-process is responsible for the creation of half of the nuclei heavier than iron.

The rp-process can be thought of as the mirror of the r-process. Here a series of rapid proton capture reactions create nuclei out to the proton drip line. Due to the Coulomb barrier of the proton capture reactions, this process must occur in a high-temperature environment.

It is thought to occur in compact, binary systems like a neutron star paired with a main sequence star. There, the intense gravity of the neutron star can pull matter off of the companion star. This accretion of matter, largely protons and helium, builds a layer on the surface of the neutron star that increases in temperature as the density increases. Eventually enough material collects on the surface that a thermonuclear explosion can occur, triggering temperatures high enough for the rp-process.

While the overall mechanisms for the r- and rp-processes are thought to be understood, the majority of nuclei involved in the processes have never been studied experimentally. *By studying these exotic nuclei in the lab, we can better understand the reaction rates in these astrophysical processes.*

1.3 Nuclear Structure

1.3.1 Nuclear Models

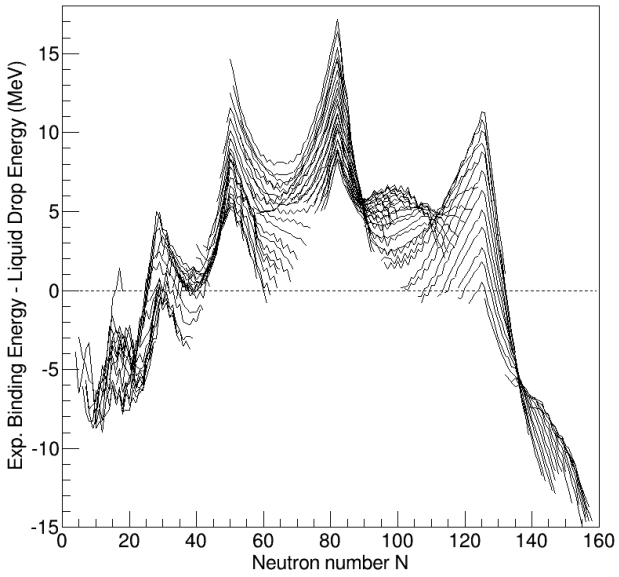

Figure 1.4: Residuals (experimental binding energy - LDM prediction) as a function of neutron number (N). Different curves correspond to different elements (Z). Large deviations from the data are seen at N =28, 50, 82, and 126. To keep these deviations in perspective, the total binding energies are roughly 8 MeV $\times$ the number of nucleons.

In the 1930s, Carl Friedrich von Weizsäcker introduced one of the first successful models of the nucleus, called the Liquid-Drop Model (LDM). The LDM model treats the nucleus as a semi-classical fluid of neutrons and protons, ie this model does not try to solve the quantum mechanical problem. This can be considered a "macroscopic" model of the nucleus because it starts with a term describing the bulk properties of infinite nuclear matter, and then applies corrections due to the finite size of the nucleus. Corrections are needed for the surface (nucleons on the surface do not "feel" the attractive force from all sides), the Coulomb repulsion (every protons repels every other proton), and a correction for a neutron/proton asymmetry . The asymmetry correction is the only quantum mechanical ingredient to the LDM, and accounts for the fact that neutrons and protons should fill single-particle orbitals in the same way that electrons do in atoms. Neutrons and protons fill these orbits separately, and the orbits should be roughly the same for each particle type, so there is an energy penalty for having different numbers of neutrons and protons. There is also a term which accounts for the pairing of like nucleons. The binding energy predicted by the LDM can be summarized in the following equation:

$$B(Z,A) = C_1 A - C_2 A^{2/3} - C_3 \frac{Z^2}{A^{1/3}}(1 - \frac{C_4}{C_3} A^{-2/3}) \\ - C_1 k \frac{(N-Z)^2}{A}(1 - \frac{C_2}{C_1} A^{-1/3}) + \delta \quad (1.6)$$

The terms are: the volume term (bulk binding), surface correction, Coulomb term with surface diffuseness correction, the asymmetry term with surface correction, and the pairing term δ. The C_i coefficients are fit to the empirical binding energies of nuclei. This phenomenological model does a remarkable job of reproducing experimental binding energies across the nuclear chart, Fig. 1.4. However, at certain values of neutron number, N, one can see large deviations with irregular spacing from the liquid drop model, suggesting a need for a better treatment of the quantum mechanical nature of nuclei.

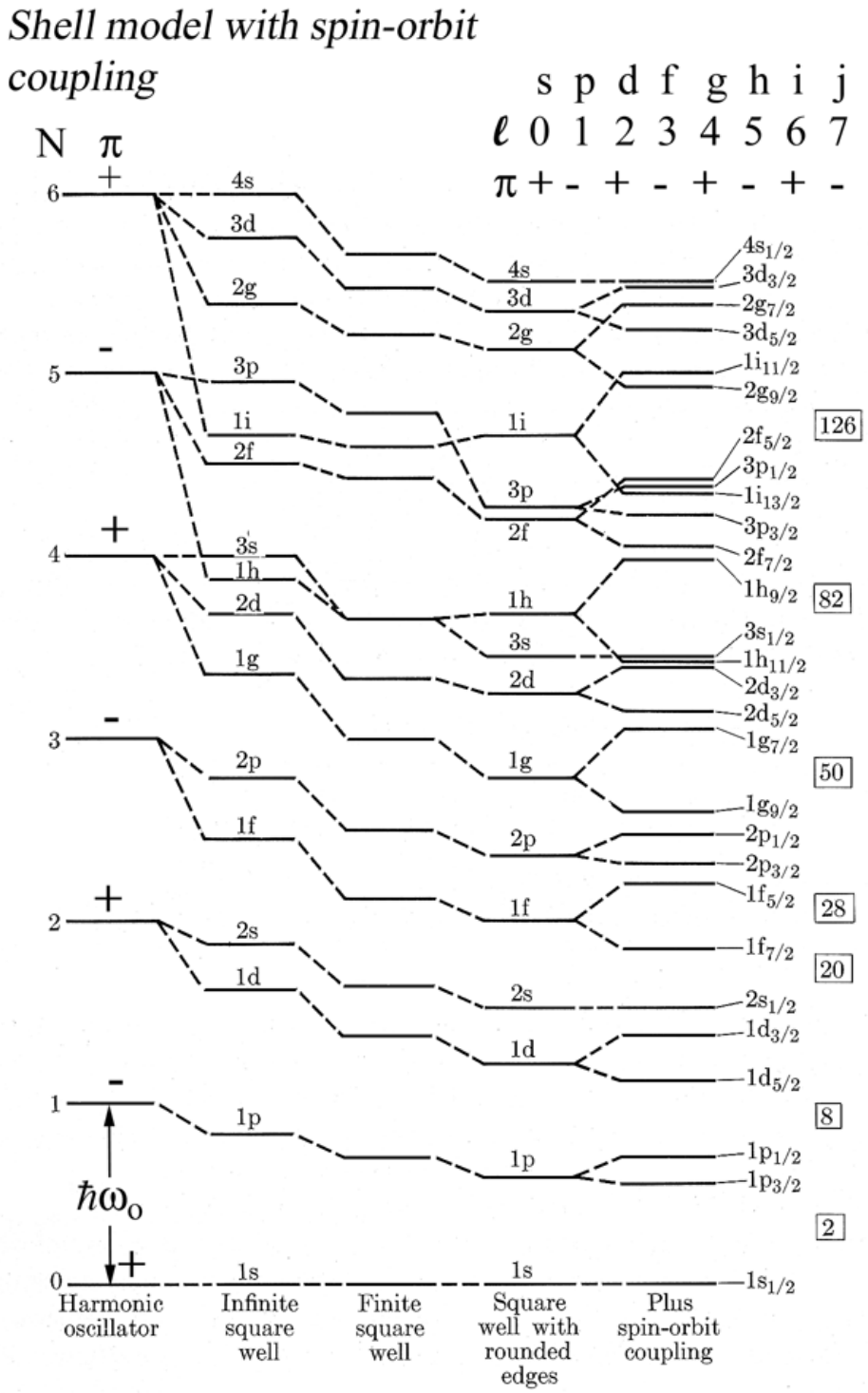

Figure 1.5: Single-particle levels for the IPM with (from left to right) (a) the harmonic oscillator, (b) infinite square well, (c) finite square well and (d) Wood-Saxon potentials. The final column is for a Wood-Saxon potential with the spin-orbit term included.

The most common quantum mechanical approach to the many-body nuclear problem is the independent particle model (IPM). It is a mean-field theory in which the nucleus is approximated by considering each nucleon as an independent particle moving in an average potential well created by all of the other nucleons. This simplifies the N-body problem into N, one-body problems. The result is a shell structure with single-particle levels, completely analogous to what is taught about the electronic structure of atoms in introductory classes. The form of the potential changes the ordering of the levels in energy, with the best choice for nuclei being a square well with rounded edges (Wood-Saxon) potential. The potential well for protons includes a Coulomb interaction in addition to the central potential felt by all nucleons. The addition of spin-orbing ($\ell \cdot s$) coupling to the Wood-Saxon potential reproduces the shell gaps seen experimentally for nuclei, Fig. 1.5. The ordering of these levels works well for light (A<50) nuclei near stability, but some reordering of the levels has been observed in some exotic nuclei.

1.3.2 Isospin

In nuclear physics it is often useful to introduce the quantity known as isospin, t or T, which is an approximate quantum number related to the strong force. This quantum number follows all of the same algebraic rules as spin or angular momentum. A generic nucleon has $t = 1/2$, with the isospin projection $t_Z = -1/2$ for a proton and $t_Z = 1/2$ for a neutron. This definition is arbitrary and different subfields choose different conventions. Using this convention we can define the total isospin projection of a given nucleus as,

$$T_Z = \frac{(N - Z)}{2} \tag{1.7}$$

where N is the number of neutrons and Z is the number of protons. Most nuclear states are characterized by a single isospin, a quantum number with a value greater or equal to its projection. A few states have mixed isospin character which reinforces the fact that isospin

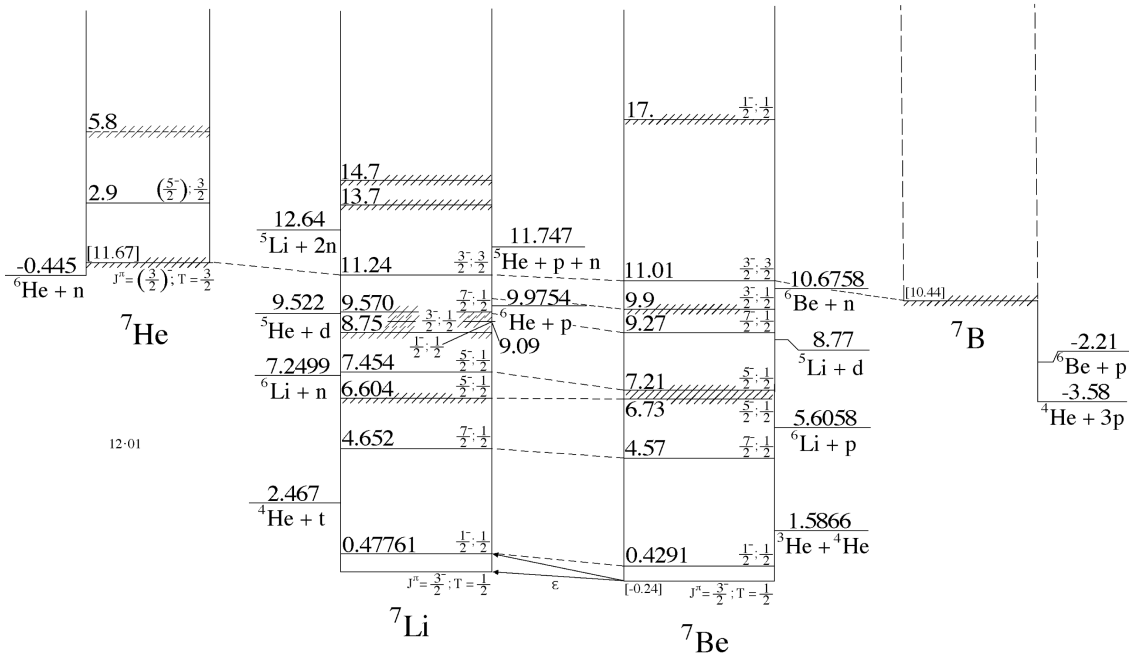

Figure 1.6: Isobar diagram for A=7. Levels are labeled by their energy, spin, and isospin when known, with intrinsic widths indicated by the size of the cross-hatching. States with identical quantum numbers are connected by dashed lines to their analogs. Thresholds for particle decays are labeled with their energy relative to the ground state of the given nucleus. Figure taken from Ref [1].

is only an approximate quantum number. The lowest lying states have the lowest values of isospin (equal to the magnitude of its projection) and with increasing excitation energy, progressive thresholds are passed at which higher isospin states are allowed.

For a given isospin T, there are $2T+1$ projections (referred to as an isospin multiplet), each corresponding to a state in a different nucleus. An example of this can be seen in Fig. 1.6. The ground state of ^{7}He has spin and parity, J^{π}, of $3/2^{-}$. The isospin projection is $T_Z = \frac{5-2}{2} = \frac{3}{2}$, and the total isospin is $T = |\frac{3}{2}| = \frac{3}{2}$. Following the dotted lines along the isobaric chain one can see that in each nucleus one finds a state with the same J^{π} and T as the ^{7}He ground state. These special excited states in ^{7}Li and ^{7}Be are the lowest $T = 3/2$ states in those nuclei and are known as isobaric analog states (IAS). They have all of the same nuclear quantum numbers as their analogs (the ground states of ^{7}He and ^{7}B) with the exception of the projection of the isospin quantum number. Chapters 3, 6, and 7 will focus on these special states.

1.3.3 Proton Decay

Beyond the proton dripline, the proton separation energy becomes negative (energy is released by removing a proton). These proton-unbound nuclei serve as impediments to the rp-process. In general, if element E_Z^A is proton unbound, when element E_{Z-1}^{A-1} tries to capture a proton to form E_Z^A, E_Z^A will decay back to $E_{Z-1}^{A-1} + p$, and the rp-process will not proceed until E_{Z-1}^{A-1} beta decays. For some heavy nuclei, where the proton-decay half-life is sufficiently long, proton-unbound element E_Z^A can capture a second proton to "skip over" this rp-process waiting point.

Thermodynamically, once a nucleus has a negative proton-separation energy, it will one-proton ($1p$) decay. However, kinetically it can compete with beta decay. The Coulomb barrier for proton decay increases with increasing Z. For a fixed decay energy and angular momentum, this means the barrier that the proton must penetrate through becomes higher and thicker, and the half-life of the state increases. If it increases sufficiently, beta decay

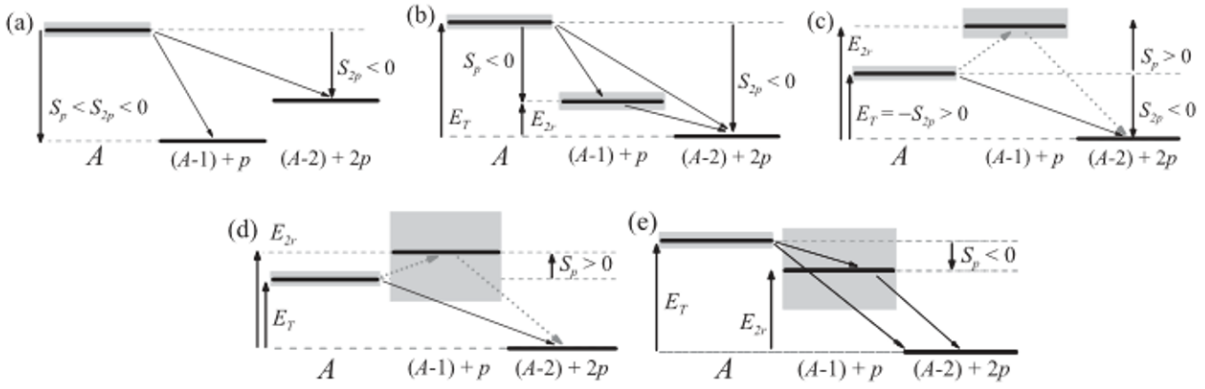

Figure 1.7: Partial levels schemes for the different classifications of $2p$ decay. Direct $2p$ decay is shown in (a) and (c), sequential in (b) and democratic in (d,e). Figure taken from Ref [2].

can become a competitive decay mode. This is true for the first discovered proton emitter, ^{151}Lu [11], where only 60% of the total decay is via proton decay.

Two-proton ($2p$) decay was first proposed by Goldansky in the 1960s for even-Z nuclei [12]. He predicted that nuclei near the proton dripline could undergo $2p$ decay when the pairing interaction made the $1p$ decay energetically forbidden, see Fig. 1.7 (c). This was the case for the discovery of the first $2p$ decaying nucleus, ^{6}Be [13]. A nucleus could in principle $2p$ decay if the only energetically accessible $1p$ intermediate is lower in energy than the $2p$ threshold, Fig. 1.7 (a), however this will only occur if the $1p$ channel is suppressed by nuclear structure. When the $1p$ intermediate is energy accessible and above the $2p$ threshold, a nucleus can $2p$ decay through two sequential steps of $1p$ decay, Fig. 1.7 (b). If the $1p$ intermediate is wide relative to the decay energy, Fig. 1.7 (d,e), then the distinction between direct and sequential $2p$ decay becomes less clear. In these cases, often called democratic decay, the lifetime of the $1p$ is sufficiently short that it has no effect on the kinematics of the decay. To any experiment, these decays appear the same as direct $2p$ decay. All three of these classifications are based entirely on energetics. Chapter 3 will expand these cases and classifications to include the effects of isospin.

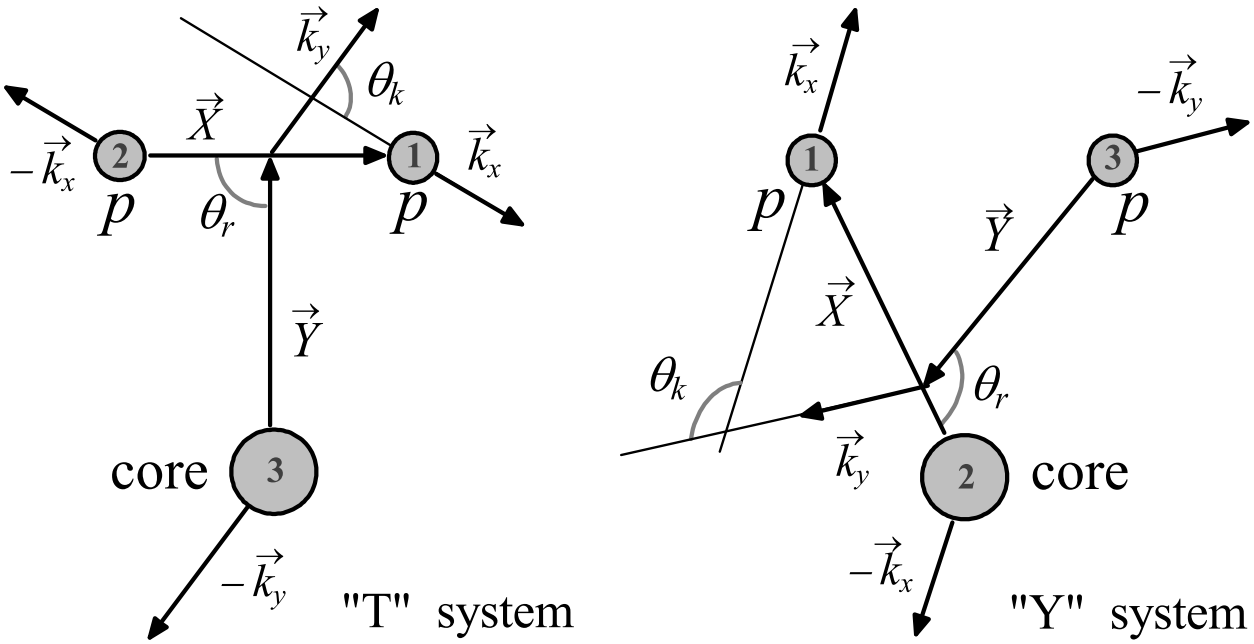

Figure 1.8: Jacobi vectors for three particles in coordinate and momentum spaces in the "T" and "Y" Jacobi system. The $\vec{X}$ and $\vec{Y}$ vectors define each system. Figure taken from Ref [3].

1.3.4 Decay Correlations

In a three-body decay (like $2p$ decay), there are nine degrees-of-freedom needed to describe the momenta of the particles. Three of these are associated with the center-of-mass motion, and can be removed by working in the center-of-mass frame. Three more describe the Euler rotation of the decay plane. For a spin 0 system, these rotation angles can also be ignored. However, if the system has a finite spin these angles contain information about spin alignment of the system. In this work, we will not worry about any alignment as it plays no role on the internal degrees of freedom. One final degree-of-freedom can be constrained because the decay energy is fixed. This leaves only two degrees-of-freedom associated with the relative motion of the three-body system. Two common choices, the Jacobi "T" and "Y" systems, are shown in Fig. 1.8.

The energy and angle parameters for the Jacobi momenta, $\mathbf{k}_x$, $\mathbf{k}_y$, can be described by:

$$\begin{aligned} \varepsilon = E_x/E_T\,, \qquad \cos(\theta_k) = (\mathbf{k}_x \cdot \mathbf{k}_y)/(k_x\, k_y)\,, \\ \mathbf{k}_x = \frac{A_2\mathbf{k}_1 - A_1\mathbf{k}_2}{A_1 + A_2}\,,\ \ \mathbf{k}_y = \frac{A_3(\mathbf{k}_1 + \mathbf{k}_2) - (A_1 + A_2)\mathbf{k}_3}{A_1 + A_2 + A_3}, \\ E_T = E_x + E_y = k_x^2/2M_x + k_y^2/2M_y, \end{aligned} \tag{1.8}$$

where M_x and M_y are the reduced masses of the X and Y subsystems, and A_i are the mass numbers of the particles. For the Jacobi "T" system, k_3 is assigned to be the core. Then the energy parameter, E_{pp}, is the relative energy between the two protons. For the Jacobi "Y" system, $k_3 \to k_p$, and the energy parameter describes the relative energy between the core and the proton, E_{core-p}. The angular parameter, in both systems, describes the angle between $\mathbf{k}_x$, which is the momentum of particle 1 in the center-of-mass frame of particles 1 and 2, and $\mathbf{k}_y$, which is the center-of-mass momentum of particles 1 and 2 in the center-of-mass frame of the whole system. For example, in the Jacobi "Y" frame if the two protons are emitted back-to-back (opposite sides of the core), then $\cos(\theta_k) = 1$. If they are emitted close together, $\cos(\theta_k) \simeq -1$. These are referred to colloquially as "cigar" and "diproton" configurations.

Chapter 2

Experimental Methods

2.1 Overview

There were two separate, but related, goals that motivated the experiments of this thesis. The first goal was to measure the decay energy, intrinsic width, decay mode, and decay correlations for the isobaric analog state (IAS) of ^{8}C ground state (g.s.) in ^{8}B. A previous study [14] found that the ground state of ^{8}C decays via two sequential steps of prompt $2p$ decay (through $^{6}\mathrm{Be}_{g.s.}$). As that experiment was designed to detect the decay products of ^{8}C, namely protons and alphas, the ranges for the silicon ΔE detectors were not set up to measure particles heavier than helium. In a few detectors, a small amount of ^{6}Li was seen that did not over-range the amplifiers. In the invariant-mass spectrum of $2p$+^{6}Li there was a peak at 7.05 MeV. This could either correspond to an unknown state in ^{8}B at 7.05 MeV if the $2p$ decay directly populated the $^{6}\mathrm{Li}_{g.s.}$, or to a state at 10.61 MeV if it decayed to the excited state at 3.5 MeV in ^{6}Li. This state is the T=1 isobaric analog, the analog of ^{6}He, and γ decays to the ground state. As the previous experiment was not sensitive to γ rays, they could not determine this directly, however 10.61 MeV was the known excitation energy of the isobaric analog state (IAS) of ^{8}B, but it was not known how this continuum state decayed. Thus a new experiment was performed with *a)* higher ranges on the silicon

detectors to measure the ^{6}Li fragments without bias and *b)* an array of gamma detectors was added around the target to detect any γ rays in coincidence with the $2p$ decays.

The second goal of these experiments was to measure a second ground-state/ isobaric analog pair, $^{16}\mathrm{Ne}_{gs}$ and $^{16}\mathrm{F}_{IAS}$. While the ground state of ^{16}Ne had been seen in transfer reactions in previous studies [15, 16, 17, 18] and this state was known to be unstable with respect to $2p$ decay, no data existed on the three-body decay correlations. The measured intrinsic width was far wider than theoretical predictions and our experiment would remeasure the width with better resolution than the previous work. Nothing was previously known about the isobaric analog state in ^{16}F, however it was expected to decay by $2p$ emission to the isobaric analog state in ^{14}N. This is analogous to the decay of $^{8}\mathrm{B}_{IAS}$.

These experiments were performed at Michigan State University at the National Superconducting Cyclotron Laboratory. A schematic of the experimental setup is shown in Fig. 2.1. Using a set of coupled cyclotrons (K500 + K1200) a beam of ^{16}O nuclei, accelerated to 150 MeV/A (roughly half the speed of light), was impinged on a ^{9}Be target. The beam underwent reactions with the target and produced numerous light fragments. Using a magnetic separator, these fragments were filtered and a secondary beam of ^{9}C (68 MeV/A, 9.0×10^{4} pps and 50% purity) was produced. This beam was transported to the secondary reaction target where the $^{8}\mathrm{B}_{IAS}$ was produced by proton knockout reactions. For the second experiment a primary beam of ^{20}Ne (170 MeV/A) was used to produce a secondary beam of ^{17}Ne (63 MeV/A, 1.2×10^{5} pps and 11% purity). Then states in ^{16}Ne and ^{16}F were populated following neutron and proton knockout respectively.

2.2 Invariant-mass Method

For particle-decaying states with lifetimes shorter than $\approx$ 10 ns, the invariant-mass method is ideal for measuring the decay energy and, in the case of three-body decay, the momentum correlation between the fragments. The basic idea of the method is to measure the momen-

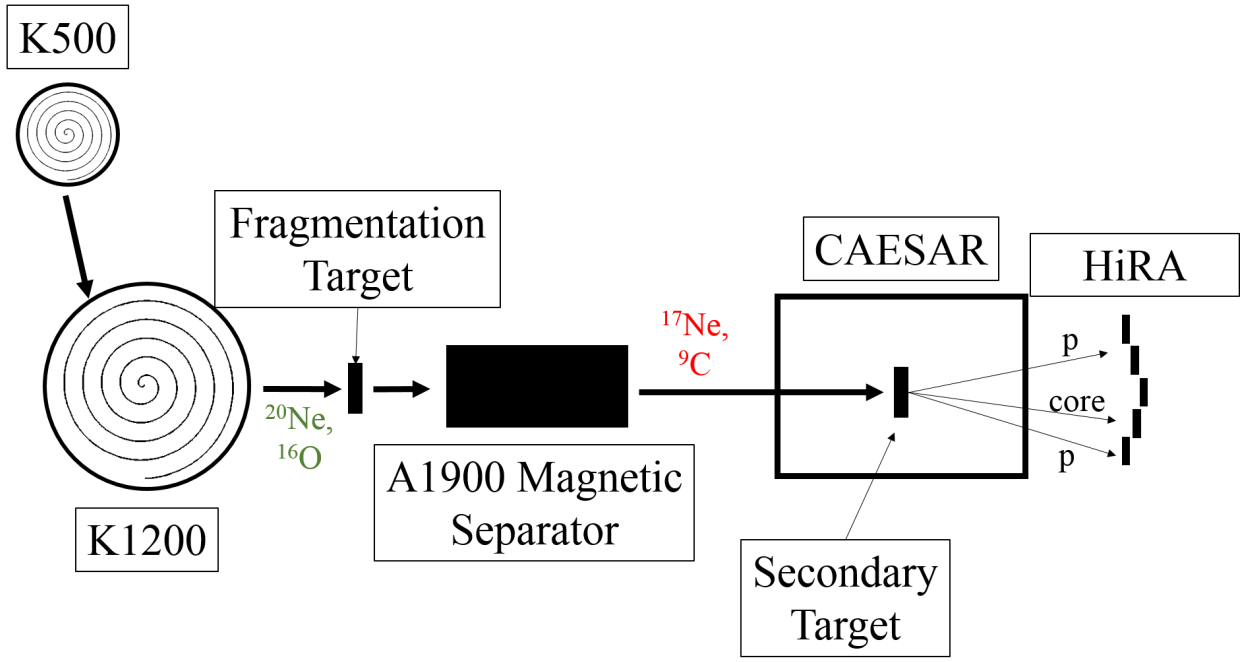

Figure 2.1: Schematic of the experimental setup at Michigan State University. Stable beams (green) are accelerated first by the K500 and then the K1200 cyclotrons. The stable beam impinges on a ^{9}Be target, where it is fragmented. The fragments are separated by the A1900 magnetic fragment separator based on their mass-to-charge ratio. These radioactive beams (red) are transported to the experimental area where they undergo further reaction to create the unbound products. Charged particles are detected with HiRA, and γ rays are detected by CAESAR.

tum vectors and particle type for all of the products of the decay and use that information to reconstruct the mass of the parent state in the rest frame of that particle. The invariant mass (in units of energy) is given by Eq. 2.1

$$Mc^2 = \sqrt{(\sum_i E_i)^2) - (\sum_i \vec{p}_i c^2)^2} \tag{2.1}$$

where E_i and p_i are the total energy and momentum of each fragment. In these experiments the momentum of each particle is determined by measuring the energy deposited in the silicon and CsI(Tl) detectors of HiRA with the direction of each vector determined from the x and y strips of the silicon detector and assuming the reaction took place in the center of the target and the mass extracted using the standard $\Delta E - E$ technique. This method relies on the fact that different particles deposit their energy at different rates based on their stopping power, Eq. 2.2

$$\frac{dE}{dx} \propto \frac{Z^2 A}{E} \tag{2.2}$$

where Z is the ion's charge, A is the ion's mass number, and E is the kinetic energy (At the energies relevant here, light nuclei are fully stripped and thus their charge q = Z.). By plotting the energy lost in a thin transmission detector (ΔE) vs the energy deposited in a thick stopping detector (E), the ions will separate into groups of bands with the same charge, Z, with each band corresponding to a different isotope, Fig. 2.2.

2.3 The Detectors

The charged particles produced in the decay of the nucleon knockout products were detected in the High Resolution Array (HiRA) [19]. For these experiments, HiRA consisted of 14 Si-CsI(Tl) $\Delta E - E$ telescopes located 85 cm downstream of the secondary target, subtending polar angles from 2.0° to 13.9° in the lab. The telescopes were arranged in five towers with

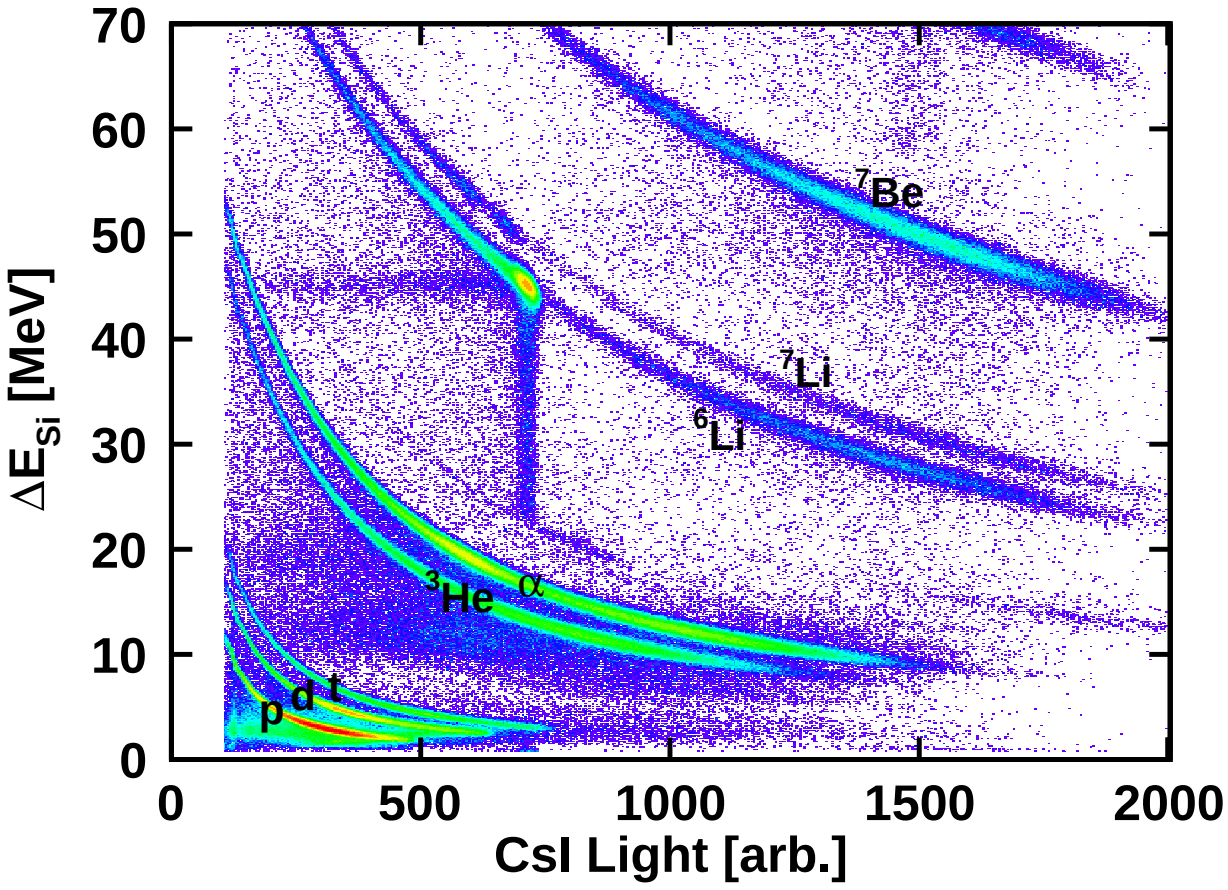

Figure 2.2: Energy deposited in a silicon (ΔE) vs energy deposited in a CsI(Tl) (E) for a typical outer HiRA telescope. The silicon energy has been calibrated and the CsI(Tl) energy is uncalibrated. Different bands are labeled by their corresponding isotope.

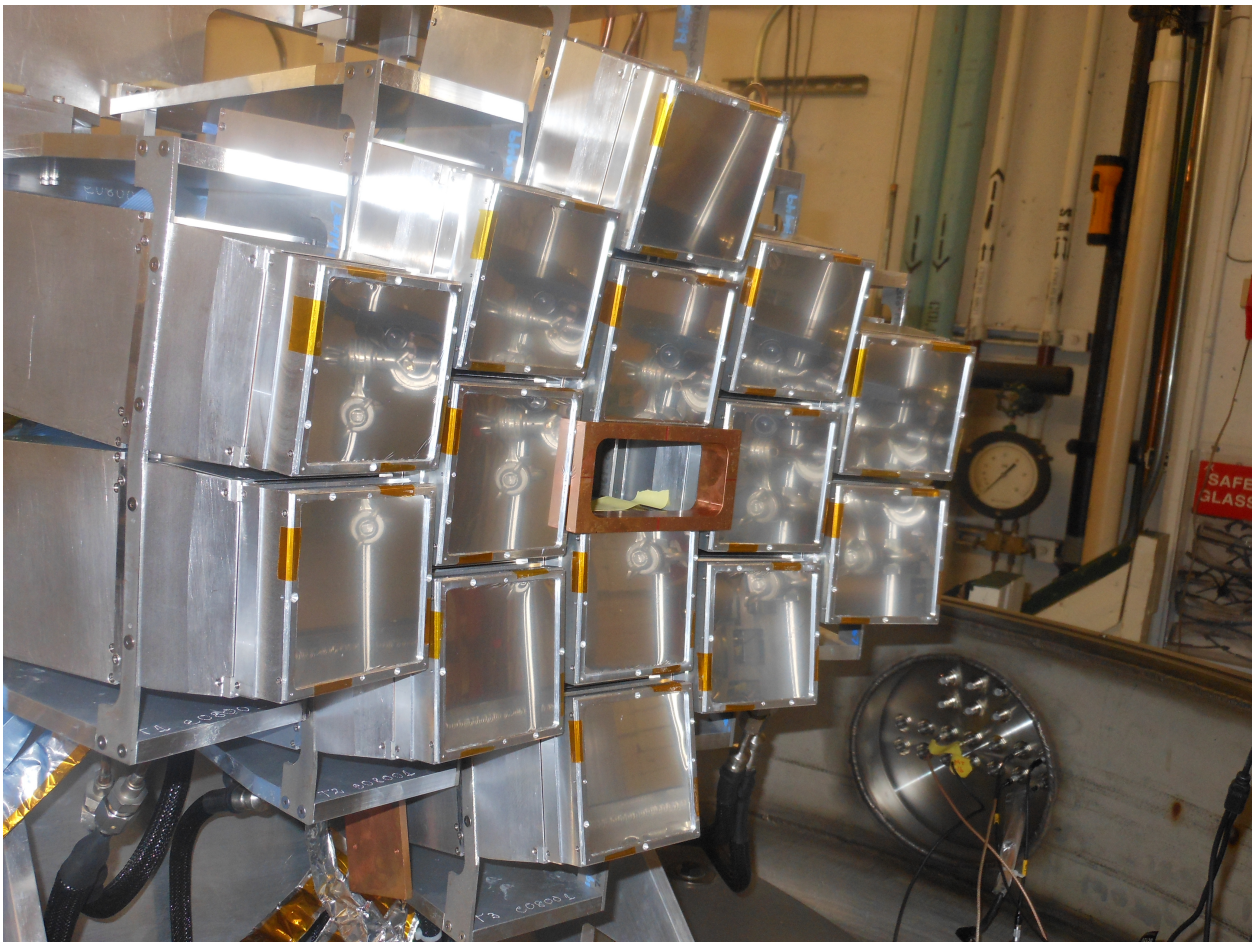

Figure 2.3: HiRA Array viewed from upstream.

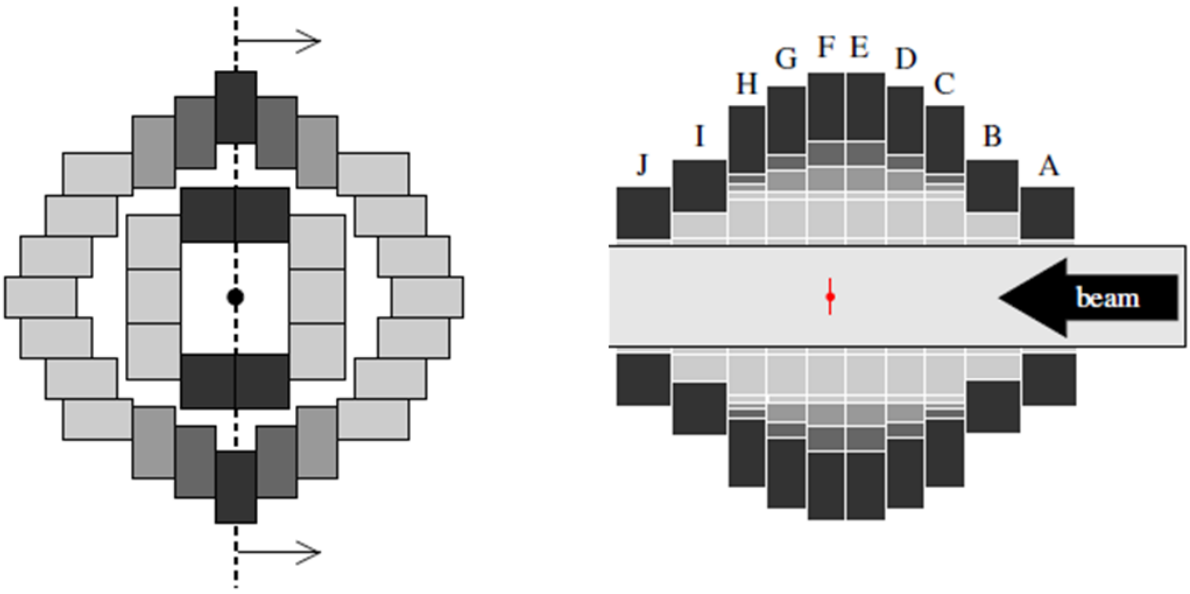

Figure 2.4: Layout of CAESAR detectors. (left) cross-sectional view perpendicular to beam axis showing rings B and F and (right) cross-sectional view parallel to beam axis showing all ten rings and target position (dot with vertical line through it). Taken from Ref. [4].

a 2-3-4-3-2 arrangement, Fig. 2.3. The center tower had a small gap between the two innermost telescopes, centered on the beam axis, to allow for the unreacted beam to pass through. Each telescope consisted of a 1.5-mm-thick double-sided silicon strip ΔE detector followed by a 4-cm-thick CsI(Tl) E detector. Each of the 14 HiRA telescopes has four CsI(Tl) detectors, each spanning a quadrant of the preceding Si ΔE detector. Signals produced in the Si were processed in one of two ways. For the two detectors immediately above and below the beam, the signals were amplified using external charge-sensitive amplifiers (CSAs) and then resistively split into low- and high-gain channels before being processed by the HINP16C ASIC (application-specific integrated circuit) electronics previously designed by our group [20]. This provided roughly six times the dynamic range of the other telescopes. The other Si detectors were processed with the HINP16C chip electronics and amplified with CSAs internal to the chip. Signals from the CsI(Tl) detectors were processed using conventional electronics.

γ rays were measured in coincidence with charged particles using the CAEsium-iodide

scintillator ARray (CAESAR) Ref. [4], Fig. 2.4. In these experiments CAESAR comprised 158 CsI(Na) crystals covering the polar angles between 57.5° and 142.4° in the laboratory with complete coverage in the azimuthal angles. The first ring (A) and the last two rings (I,J) of the full CAESAR array were removed due to space constraints. Ring B consisted of 10, 3" x 3" x 3" crystals and rings C-H consisted of 24, 2" x 2" x 4" crystals in a closely-packed geometry. Signals from the CsI(Na) detectors were processed using conventional electronics.

2.3.1 Silicon

The High Resolution Array (HiRA) is comprised of 14 "stack" telescopes, consisting on a thin transmission detector and a thick stopping detector. The thin detectors of HiRA in this configuration are ion-implanted passivated silicon semiconductor detectors. The silicon detectors, manufactured by Micron Semiconductor [21], are 6.4 cm x 6.4 cm x 1.5-mm-thick with the faces subdivided into 32 strips orthogonal to one another on the front and back. This high segmentation provides good angular resolution ($\Delta\theta/\theta = 0.1°$) and allows multiple particles to be detected in the same detector. The reduced area for each strip also reduces the capacitance of each detector element thus reducing the noise.

Semiconductor detectors work on the following principle. As a charged particle moves through the detector volume, electron-hole pairs are created. The number of pairs created depends on the stopping power, dE/dx, which determines the energy deposited (E_d), and the band gap of the material, which determines the amount of energy needed to create an electron-hole pair. For silicon the average energy required to create a electron-hole pair is 3.7 eV, therefore $E_d = 1$ MeV can produce $10^6/3.7 \approx 270{,}000$ pairs. Normally these pairs will quickly recombine, however by applying a modest electric field ($E \approx 2000$ V/cm for a HiRA detector) the electrons and holes will drift towards opposite surfaces where they can be collected. Since the production of pairs is linearly proportional to the energy deposited, these detectors can be used to measure charged particles over a large range of energies. A standard silicon detector is made of a sandwich of two silicon crystals with different dopants

to make a p-n junction. N-type silicon is made by adding a group V element as an impurity into the bulk and p-type is made by adding group III. In a p-n junction, thermal diffusion will drive electrons from the n-type (donor) region to the p-type (acceptor) region. This leads to a region in the middle which is depleted of charge carriers, which creates a barrier to current flow. By applying a positive potential to the n region and negative to the p region (often called reverse biasing) this barrier across the junction can be enhanced. A silicon detector is a p-n junction that has been reversed biased to the point that the bulk of the detector is "fully depleted" of charge carriers. When a charged particle creates electron-hole pairs, they are swept to the respective surfaces and collected through metal contacts deposited on the surfaces. For a HiRA detector the total energy deposited can be determined through either the electrons or holes collected and the position of the deposited energy can be determined by which strip collects charge on the front and back.

2.3.2 Scintillators

The thick "stopping" detectors in a HiRA telescope are 4-cm-long CsI trapezoidal crystals doped with thallium at the ppt level. These crystals are only slightly hygroscopic, which makes them ideal for applications for which they cannot be placed into air-tight cans, such as charged-particle detection (A can would absorb part of the energy, leading to worse energy resolution). These crystals are 3.5 cm x 3.5 cm in the front and 3.9 cm x 3.9 cm in the back. Behind each CsI(Tl) is a 3.9 cm x 3.9 cm x 1.3 cm light guide optically coupled by BC 600 optical cement. A 1.8 cm x 1.8 cm silicon photodiode was glued to each light guide with RTV615 silicon rubber. The light output of the CsI(Tl) crystal is well suited in wavelength for photodiode readout. To make each crystal optically separated, the crystal is wrapped in cellulose nitrate membrane filter paper on the long sides, with thin aluminized Mylar foil covering the front. The light guides are painted with BC-620 reflective paint. Four crystals are wrapped together with Teflon tape and placed behind a silicon detector.

Unlike a silicon detector, where energy is measured by the number of electron-hole pairs

produced, scintillators like CsI(Tl) measure energy by the light produced. When a charged particle enters a crystal, ionization creates unbound electron-hole pairs or bound electron-hole pairs called excitons. These excitons move freely within a crystal until they are trapped by impurities (sites of dopant atoms) or crystal defects. Once the exciton is trapped, it will radiatively de-excite with the emission of a visible photon. This light is collected by the photodiode where it creates electron-hole pairs which are collected and read out as a current. The excitons can also non-radiatively de-excite, the energy then goes into heat (crystal vibration). The non-radiative channels represent about 75 % of the total de-excitation channels.

CsI doped with sodium has about twice the light output of CsI doped with thallium. This comes at the cost of being highly hygroscopic, so it must be hermetically sealed in a can. The CsI(Na) detectors of the CAESAR array work the same way as CsI(Tl). γ rays can deposit all of their energy into the kinetic energy of a single electron via the photoelectric effect or part of their energy via Compton scattering. This electron further ionizes the medium, and the electron-hole pairs produced de-excite as in CsI(Tl). If the γ ray has energy larger than 1.022 MeV, it can also undergo pair production and spontaneously create a positron-electron pair in the presence of matter. These charged particles lose energy as before, but when the positron is thermalized it will annihilate with an electron and create two 511 keV γ rays. One or both of the annihilation photons can escape the detector reducing the deposited energy, yielding single and double escape peaks. The Compton scattered γ ray and those created from the positron annihilation, if detected in a neighboring crystal, can be added to the energy collected in the crystal with the first interaction.

2.3.3 Calibration

In order to determine the total energy deposited by the charged particles, accurate energy calibrations are needed. The silicon detectors were calibrated using a ^{228}Th multi-line α source. ^{228}Th is part of the natural decay chain beginning with ^{232}Th and will decay with

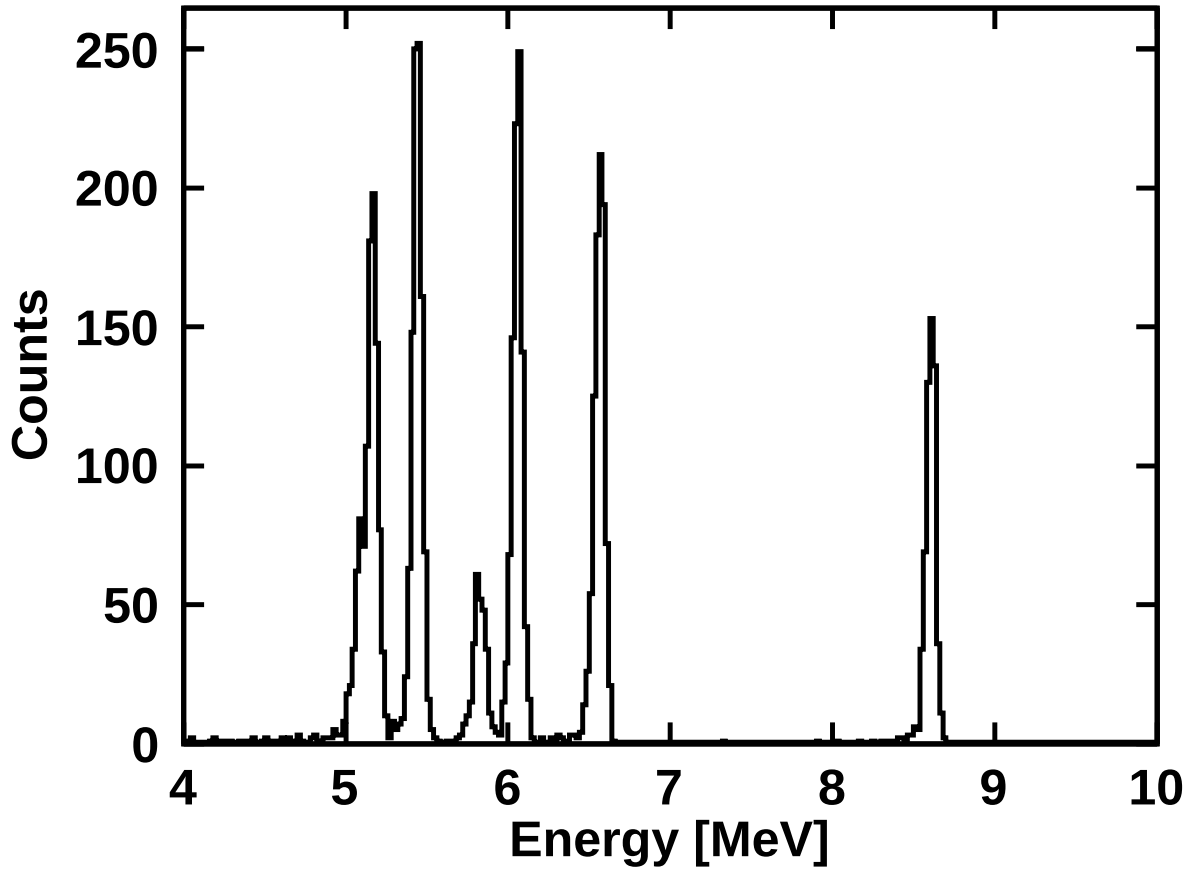

Figure 2.5: Calibrated alpha energy spectrum for a typical silicon strip in the front (hole collecting) side. The FWHM of the 8.785 MeV peak is 72 keV.

Parent	$t_{1/2}$	E_{α_0} (MeV)	E_{α_1} (MeV)	f_{α_0}	f_{α_1}	f_β
^{228}Th	1.912 y	5.423	5.340	0.726	0.274	0
^{224}Ra	3.660 d	5.685	5.449	0.949	0.051	0
^{220}Rn	55.60 s	6.288	–	1	0	0
^{216}Po	0.145 s	6.778	–	1	0	0
^{212}Pb	10.64 h	–	–	0	0	1
^{212}Bi	60.55 m	6.090	6.051	0.098	0.254	0.648
^{212}Po	0.299 μs	8.785	–	1	0	0
^{208}Tl	3.053 m	–	–	0	0	1
^{208}Pb	stable	–	–	–	–	–

Table 2.1: Alpha energies, half-lives, and branching ratios for the ^{228}Th decay chain. $\alpha's$ with less than 5% intensity are not included in this table. α_0 and α_1 denote decay to the ground state and first-excited state of the daughter, respectively.

5 $\alpha's$ and 2 $\beta's$ to ^{208}Pb, with the energies and branching ratios $f_{\alpha,\beta}$ listed in Table 2.1. A fingerprint of the known energies and intensities can be fit to the measured alpha energy spectrum, from which a linear calibration of the ADC channel number to energy can be extracted. A typical calibrated alpha energy spectrum for a HiRA silicon can be found in Fig. 2.5. While the charge output is linear with deposited energy, the electronics can have non-linearities. To test for this, test pulses of a known voltage were injected into the electronics. A spectrum of these pulses can be seen in Fig. 2.6. The electronics were found to be linear at low pulse heights with a compression (more energy per channel) at high pulse height.

Source	E_γ (MeV)	I_γ
Am-Be	4.438	1
^{60}Co	1.332	0.9998
	1.173	0.9985
^{22}Na	0.511	Annihilation
	1.2744	0.9994
^{88}Y	0.898	0.937
	1.836	0.992

Table 2.2: γ-ray energies (E_γ) and gamma fraction per decay (I_γ) for the sources used to calibrate CAESAR. γ rays from the Am-Be source come from the ^{9}Be(α,γ)^{12}C reaction.

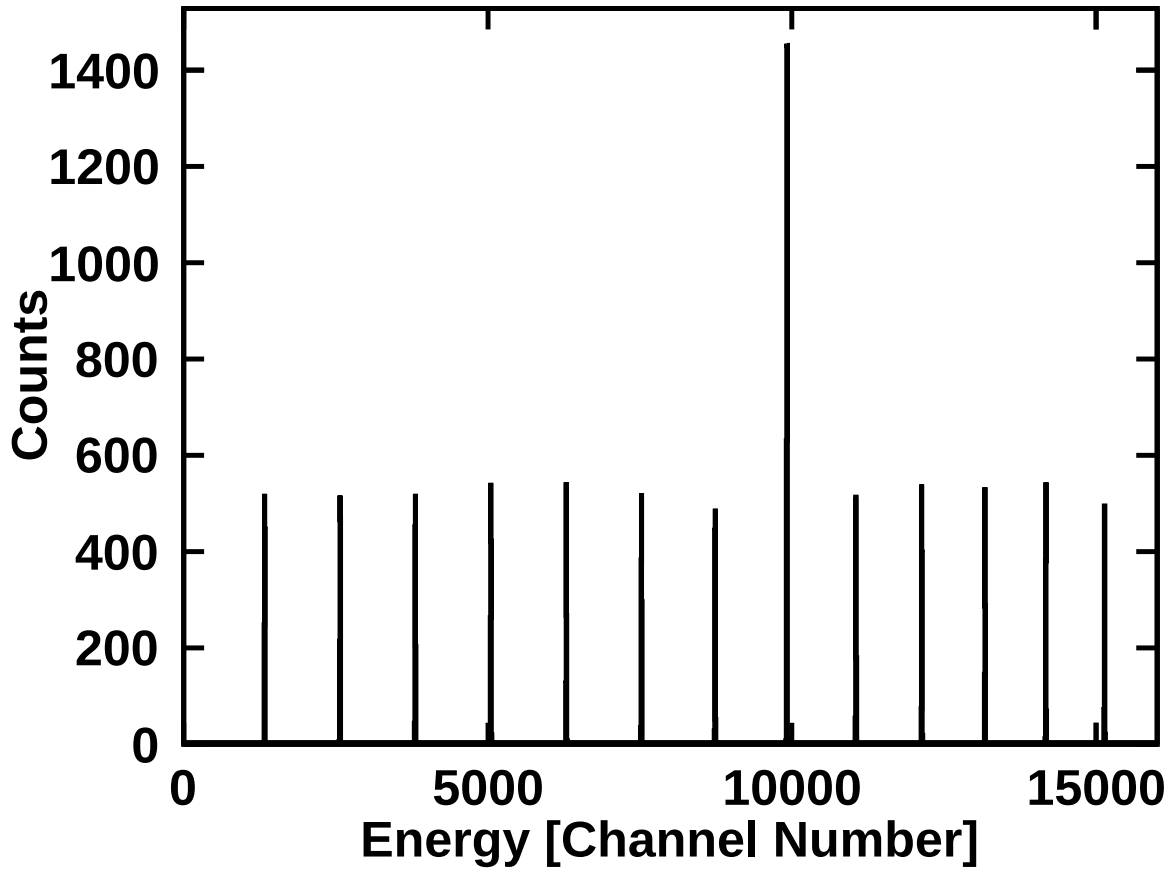

Figure 2.6: Pulser calibration spectrum for a typical silicon strip on the front side. The pulses set in uniform charge increments and a non-linearity of the electronics above half scale is clearly seen. The pulse corresponding to the peak near channel number 10,000 was run for three times as long as the other pulses.

The light output of a CsI(Tl) scintillator is highly dependent on the charge and mass of the incident ion. For a given energy, a heavy ion will deposit more energy into a medium than a light particle, from Eq. 2.2. With a high $\frac{dE}{dx}$, the high density of ionization leads to a quenching of the light. This means that the energy calibration of the CsI(Tl) will be particle dependent. Calibration is accomplished by the use of two "cocktail" beams of different magnetic rigidity containing all of the isotopes of interest. For these experiments we had two calibration beams with energies 55 MeV/A and 75 MeV/A for the N=Z nuclei. Due to the momentum acceptance of the magnetic separator used to filter the beams, separate beams of the same energy containing only protons were needed to calibrate the protons. The CsI(Na) detectors of the CAESAR array were calibrated using a standard set of γ-ray calibration sources. These sources and their γ-ray energies are listed in Table 2.2.

Chapter 3

Isobaric Analog State of ^{8}B

3.1 Background

Proton-rich nuclei beyond the proton drip line will decay by the emission of charged particles. In some cases these nuclei will decay by emitting two protons in a single step, i.e. $2p$ decay. In a recent paper it was found that the ground state of ^{8}C, the mirror of the 4-neutron halo system ^{8}He, has a very unusual decay [14]. It decays by $2p$ emission to the ground state of ^{6}Be, the mirror of another neutron halo system ^{6}He. The ^{6}Be nucleus itself undergoes $2p$ decay, and thus ^{8}C undergoes two sequential steps of $2p$ decay. In this chapter I will examine the decay of the isobaric analog state (IAS) of ^{8}C in ^{8}B. In Ref. [14] our group presented evidence that this state also undergoes $2p$ decay to the isobaric analog state of ^{6}Be in ^{6}Li. This would be the first case of $2p$ decay between IAS states and this decay would be the analog of the first $2p$-decay step of $^8C_{g.s.}$, in both cases the $2p$ decay is between T=2 and T=1 states.

Prompt two-proton emission was originally thought to occur only when one-proton decay was energetically forbidden [12]. However this definition has been extended to democratic $2p$ decay, see Fig. 1.7 (d,e), where $1p$ decay is energetically allowed but where the $1p$ decay energy is of the same magnitude as the width of the $1p$ daughter [22]. *The confirmation of*

the 2p decay of the $^{8}B_{IAS}$ would further extend this to a third class of 2p emitters where 1p decay is energetically allowed, but isospin forbidden.

With increasing mass, ^{12}O is the next known $2p$ emitter after ^{8}C. Its isobaric analog state in ^{12}N has also been ascribed to this new third class of $2p$ emitters [23] decaying to the isobaric analog state in ^{10}B. In both $^{8}\mathrm{B}_{IAS}$ and $^{12}\mathrm{N}_{IAS}$ decay, the daughter isobaric analog states decay by γ emission, but in both studies [14, 23] the γ ray was not detected allowing some uncertainty to the interpretation of the decay sequence and thus in the existence of this third class of $2p$ decay. This deficiency is remedied in the present work where the $2p$ decay of $^{8}\mathrm{B}_{IAS}$ is revisited and the γ ray from the decay of the $^{6}\mathrm{Li}_{IAS}$ daughter is observed. In addition we measure the correlations between the decay products and compare them to those previously determined for the $2p$ decay of $^{8}\mathrm{C}_{g.s.}$.

3.2 Decay mode

From the decay scheme shown in Fig. 3.1 one can see that one-nucleon decay from the IAS in ^{8}B is either energy allowed but isospin forbidden (p), or isospin allowed but energy forbidden (n). Two-proton decays to the ground and first excited states of ^{6}Li are also energy allowed but isospin forbidden. The only energy and isospin allowed decay mode is $2p$ decay to the $J^{\pi} = 0^{+}$, $T = 1$ IAS in ^{6}Li which is known to decay to the ground state of ^{6}Li by emitting a 3.563-MeV γ ray [9].

The reconstructed excitation-energy distribution of ^{8}B fragments from detected 2p + ^{6}Li events is shown in Fig. 3.2(a). The excitation energy was calculated based on the assumption that the detected ^{6}Li fragment was produced in its ground state. The only state in ^{6}Li with any significant gamma-decay branch is the IAS (T=1) state at 3.563-MeV. The narrow peak at 7.06±0.020 MeV from the reconstructed particle energies was observed previously [14] and was assigned as the IAS in ^{8}B at an excitation energy of 10.61 MeV assuming the decay populated the IAS in ^{6}Li. The spectrum of γ rays in coincidence with

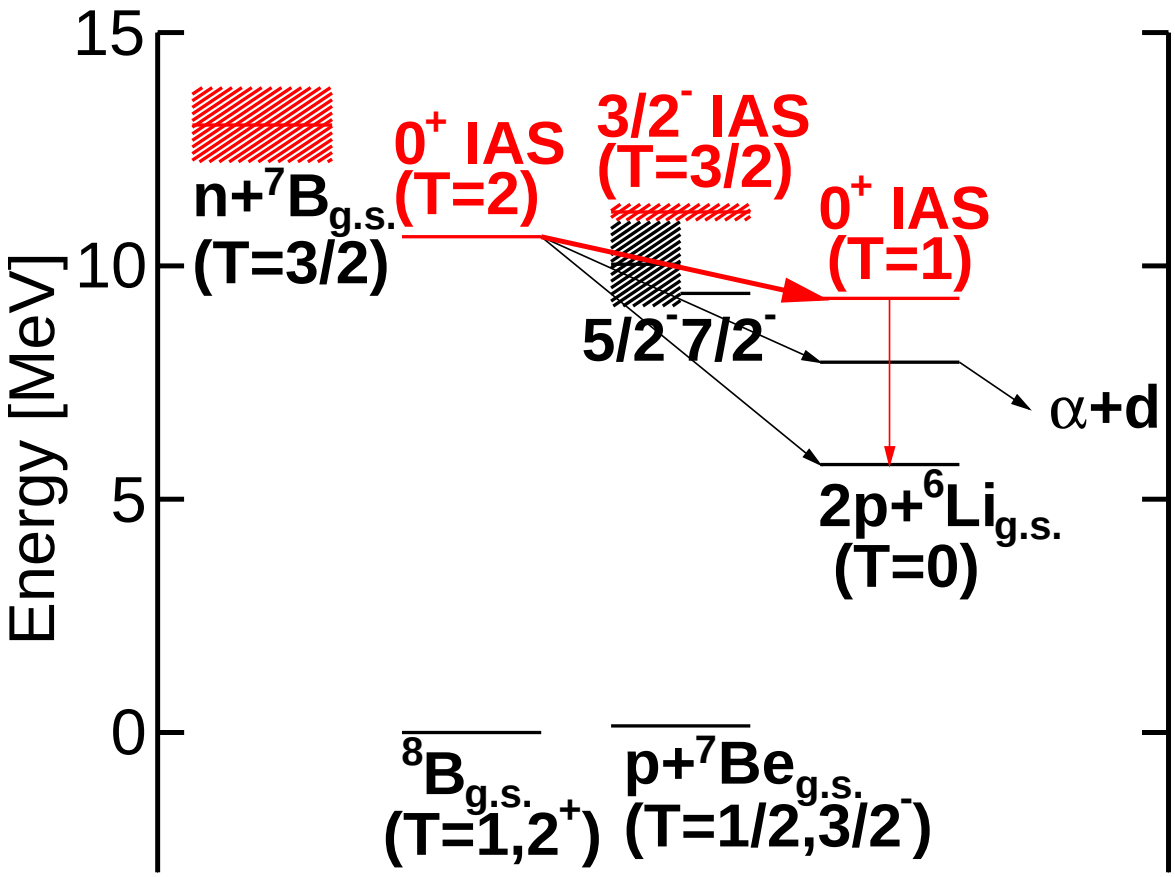

Figure 3.1: Set of levels relevant for the decay of the IAS in ^{8}B. The levels are labeled by their spin-parity (J^{π}) and isospin (T) quantum numbers. Colors indicate isospin allowed transitions. The width of the $J^{\pi} = 7/2^{-}$ state in ^{7}Be is not known, but assumed to be wide as in the mirror.

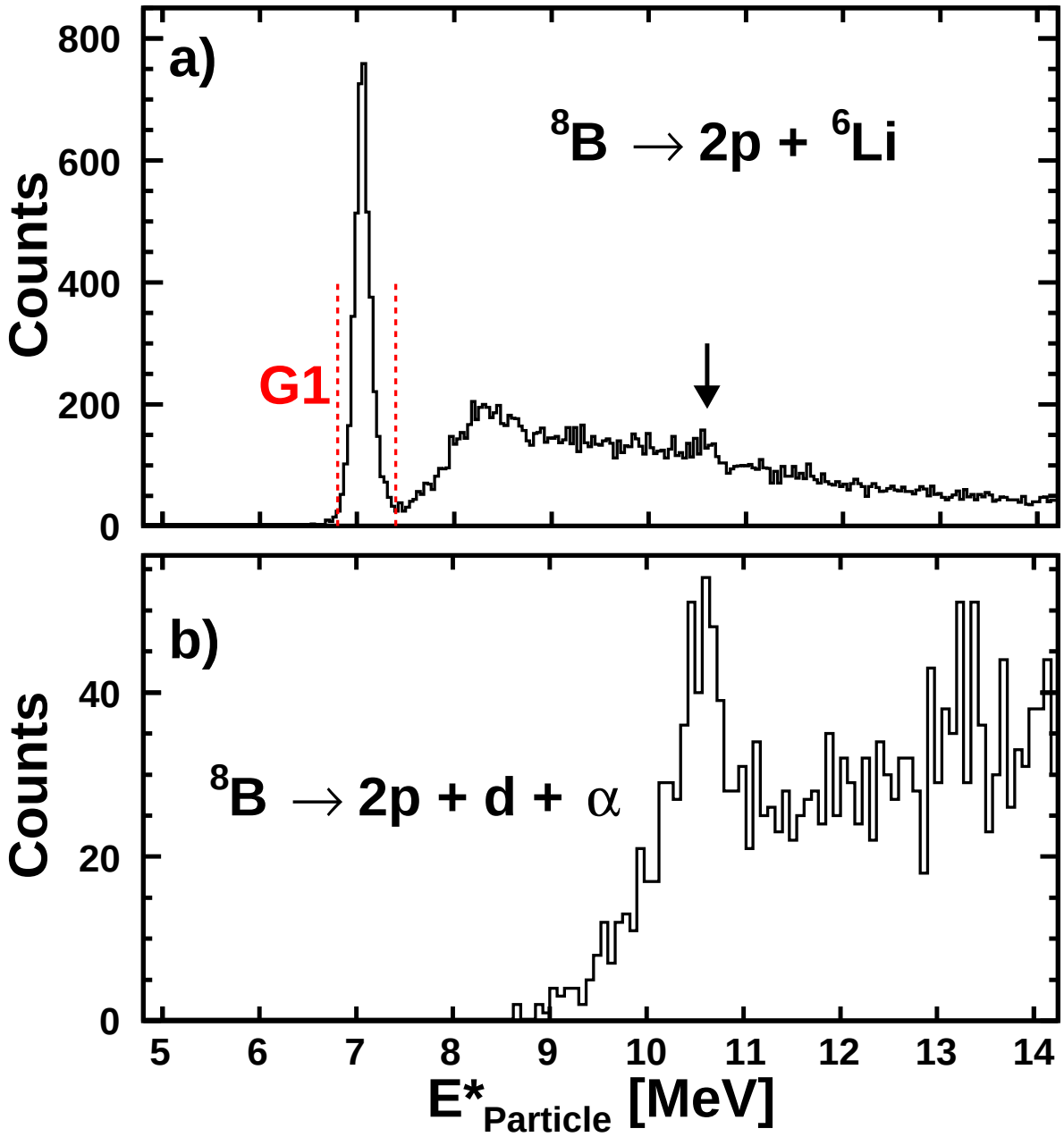

Figure 3.2: The excitation-energy spectrum from charged-particle reconstruction determined for ^{8}B from detected a) $2p$-^6Li and b) $2p$-α-d events.These energies assume no missing decay energy due to γ-ray emission.

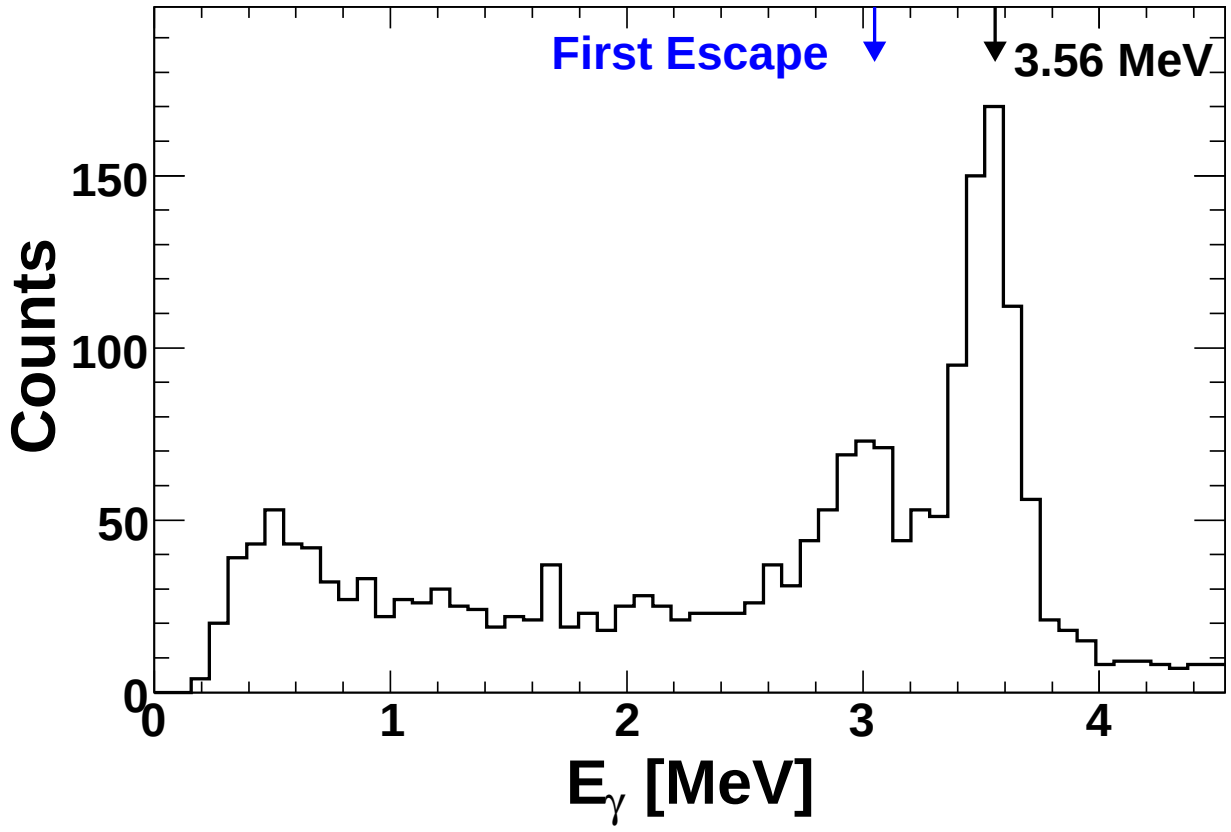

Figure 3.3: Gamma-ray energies measured in coincidence with p-p-^6Li events. This spectrum includes add-back from nearest neighbors and has been Doppler-corrected eventwise. The peak at about 3 MeV is when one of the two 511 keV γ rays from the annihilation of the pair produced positron escapes detection in CAESAR.

the reconstructed $2p$+^{6}Li events satisfying gate $G1$ in Fig. 3.2(a) is shown in Fig. 3.3. The γ-ray energies are corrected for nearest neighbor scattering and are Doppler-corrected eventwise. The spectrum has two main peaks, one at 3.56 MeV and another 511 keV lower. As a 3.563 MeV γ ray has a high probability for pair-production, a large fraction of time the γ ray will produce a positron-electron pair in one of the detectors. The charged particles will lose energy through interactions with the electrons in the crystal, depositing the bulk of their energy into that detector. When the positron slows down sufficiently, it can bind with an electron in the crystal forming positronium. The positronium will spiral in and annihilate the positron and electron with the production of two 511 keV γ rays. When one of these two γ rays is not detected in the array, the peak around 3 MeV is formed. The observed spectrum is consistent with a single gamma ray with an energy of 3.563 MeV with a significant single escape probability, confirming the IAS-to-IAS decay path. Adding the 3.563 MeV γ ray energy to the centroid of the peak in Fig. 3.2(a), gives us a total excitation energy of 10.614±0.020MeV which is consistent with the tabulated value of 10.619±0.009 MeV[9].

The emission of a γ ray from the ^{6}Li fragment will cause the fragment to recoil. If the particle was at rest, this effect would be tiny and could be immediately ignored. Since the fragment is moving and has a low mass, the recoil could actually have a measurable effect. This was tested using a Monte Carlo simulation, and the change in the centroid from the recoil is 0.002%, well within statistical uncertainties. The measured width changed by 1%, which is small compared to the other uncertainties in the detection system.

While the γ ray following the $2p$ decay of $^{12}\mathrm{N}_{IAS}$ was not measured in Ref. [23], the decay scheme is logically the same as for $^8\mathrm{B}_{IAS}$. The present measurement for $^8\mathrm{B}_{IAS}$ therefore provides support for the assigned decay path for $^{12}\mathrm{N}_{IAS}$ [23].

In light nuclei, isospin violation at the few percent level is not uncommon. Therefore it is not surprising that we also see weak decay branches from $^8\mathrm{B}_{IAS}$ to the low lying T=0 levels in ^{6}Li. From the correlations between the decay products, the $2p$+d+α exit channel is studied

as well, Fig 3.2(b). The channel is populated mostly by an isospin-forbidden $2p$ decay to the J^{π}=3^{+} excited state of ^{6}Li that subsequently decays to a d+α pair. There is also a hint of $2p$ decay directly to $^{6}\mathrm{Li}_{g.s.}$, Fig. 3.2(a). After correction for detector efficiences, the decays through these channels have yields no more than: 10% ($2p$+d+α) and 11% ($2p$+$^{6}\mathrm{Li}_{g.s.}$) relative to the isospin-conserving decay. No evidence was observed for isospin-forbidden decay to the p+^{7}Be channel. At the 3σ level, we deduce an upper limit of 7.5% for this decay.

3.3 Correlations

I now turn to the three-body correlations in the $2p$ decays of $^{8}\mathrm{B}_{IAS}$ and its isospin partner $^{8}\mathrm{C}_{g.s.}$. The energy and angular correlations in both the Jacobi T and Y coordinates are shown in Fig. 3.4 for $^{8}\mathrm{B}_{IAS}$ decay (left) and the first step of $^{8}\mathrm{C}_{g.s.}$ decay (right). In order to determine the three-body correlations in the first step of $^{8}\mathrm{C}_{g.s.}$ decay, we required that one and only one of the six possible pairs of protons, together with the α particle, reconstructed to the correct invariant mass of the ^{6}Be intermediate [14]. This event selection places some uncertainty on the extracted correlations due to a background of misassigned pairs of protons from the first and second $2p$-decay steps. This background is expected to be smooth, and one estimation of this background, described in Refs.[14, 24] is shown by the dashed curves in Fig. 3.4(e-h). In the Jacobi T energy distribution for $^{8}\mathrm{C}_{g.s.}$ decay, Fig. 3.4(e), an enhancement at low relative proton energies, a region often called the "diproton" region, is observed. The Jacobi T energy distributions for the decay of the isospin partner $^{8}\mathrm{B}_{IAS}$ are shown in Fig. 3.4(a). Distortions due to the detector acceptance and resolution are expected to be small and of similar magnitude for $2p$ decay of ^{6}Be and ^{8}C [14, 25]. In both cases one observes two broad features at low and high relative energies, corresponding to so called "diproton" and "cigar" configurations. However, the enhancement of the diproton region seen for ^{8}C decay, is not observed for $^{8}\mathrm{B}_{IAS}$ decay.

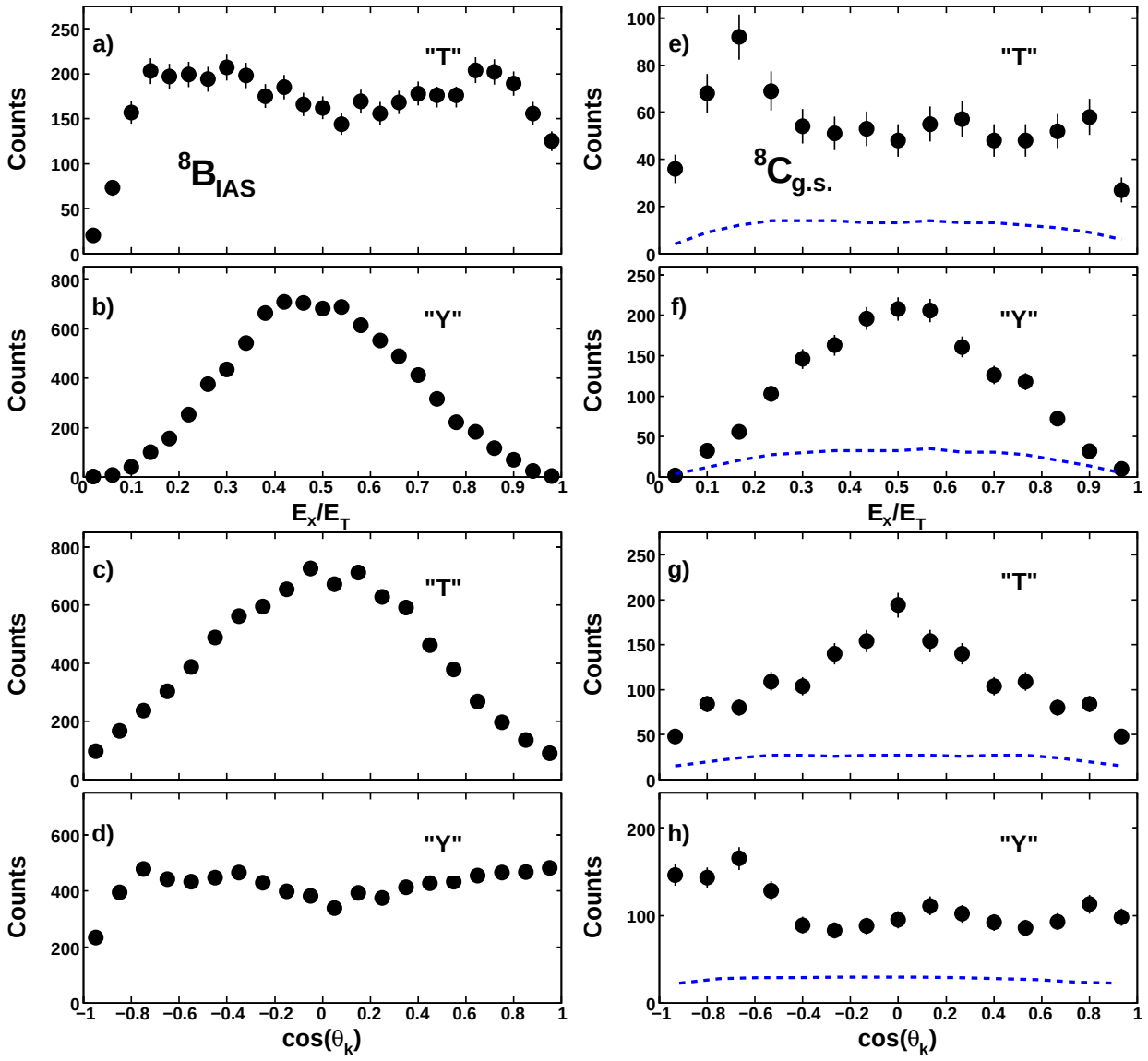

Figure 3.4: Left panel (a-d) are the projected three-body correlations from the decay of $^8B_{IAS}$ to the $2p$+$^6Li_{IAS}$ exit channel in the (a)(c) T and (b)(d) Y Jacobi systems. Energy correlations are shown in (a) and (b), angular correlations in (c) and (d). The right panel shows the same as the left, but now the correlations are associated with the first step of $^8C_{g.s}$ decay to $2p$+^{6}Be.

The Jacobi Y energy distributions for $^8B_{IAS}$ decay and $^8C_{g.s.}$ decay are shown in Fig. 3.4(b) and (f) respectively. In a three-body decay, the two protons should have approximately equal energies as this maximizes the product of their barrier penetration factors [12]. This is evidenced by the observation of a single peak at E_x/E_T=0.5 in the proton-core relative-energy spectrum (Jacobi Y system) and suggests that these are prompt $2p$ decays. As was seen for $^6Be_{g.s}$, the Jacobi Y E_x/E_T and Jacobi T θ_k distributions contain the same information, complementary to the Jacobi Y θ_k and Jacobi T E_x/E_T plots.

3.4 Summary

We have confirmed that IAS-to-IAS $2p$ decay can become the dominate decay mode when all one-nucleon emission channels are either energy or isospin forbidden. The three-body correlations from the two-proton decay of $^8B_{IAS}$ to $^6Li_{IAS}$ were measured and found to be statistically different from its isospin partner $^8C_{g.s.}$. The origin, or origins, of this difference is uncertain. The difference could result from distorting effects of the long-range Coulomb interaction which must be followed out to tens of thousands of fm in $2p$ decay theory [26]. While both decay initially to three charged particles, the ^{6}Be from the decay of $^8C_{g.s.}$ will further decay to $2p$+α within a few hundred fm of the initial decay, well within the range of the distorting final-state Coulomb interaction. Thus it is possible that the ultimate five-body final state distorts the measured correlations between the reconstructed fragments of the first three-body decay of $^8C_{g.s.}$, a distortion that would not be present for $^8B_{IAS}$. However the difference could also arise from the much shorter lifetime of $^8C_{g.s.}$ ($\tau = 2.5x10^{-21}$ s) as comparted to $^8B_{IAS}$ ($\tau > 5.5x10^{-21}$ s), which would allow the former to couple more strongly to the entrance channel knockout production reaction [27].

Chapter 4

^{16}Ne Ground State

4.1 Background

Two-proton ($2p$) radioactivity [28] is the most recently discovered type of radioactive decay. It is a facet of a broader three-body decay phenomenon actively investigated within the last decade [2]. In binary decay, the correlations between the momenta of the two decay products are entirely constrained by energy and momentum conservation. In contrast for three-body decay, the interfragment correlations are not constrained by conservation laws and are sensitive to the decay dynamics and perhaps also sensitive to the internal nuclear structure of the decaying system. In $2p$ decay, as the separation between the decay products becomes greater than the range of the nuclear interaction, the subsequent modification of the initial correlations is determined solely by the Coulomb interaction between the decay products. As the range of the Coulomb force is infinite, its long-range contribution to the correlations can be substantial, especially, in heavy $2p$ emitters.

Prompt $2p$ decay is a subset of a more general phenomenon of three-body Coulomb decay (TBCD) which exists in mathematical physics (as a formal solution of the $3 \rightarrow 3$ scattering of charged particles), in atomic physics (as a solution of the $e \rightarrow 3e$ process), and in molecular physics (as exotic molecules composed from three charged constituents) [29, 30,

31, 32, 33, 34]. The theoretical treatment of TBCD is one of the oldest and most complicated problems in physics because of the difficulty associated with the boundary conditions due the the infinite range of the Coulomb force. The exact analytical boundary conditions for this problem are unknown, but different approximations have been tried. In nuclear physics, TBCD has not attracted much attention, however the three-body Coulomb aspect of $2p$ decay will become increasingly important for heavier prospective $2p$ emitters [35].

Detailed experimental studies of the correlations have been made for the lightest p-shell $2p$ emitter ^{6}Be [36, 37] where the Coulomb interactions are minute and their effects are easily masked by the dynamics of the nuclear interactions [38]. The Coulomb effects should be more prominent for the heaviest observed $2p$ emitters, however these cases are limited by poor statistics; e.g. the latest results for the pf-shell $2p$-emitters ^{54}Zn [39] and ^{45}Fe [40] are based on just 7 and 75 events, respectively. Due to these limitations, previous $2p$ studies dedicated to the long-range treatment of the three-body Coulomb interaction [41], found consistency with the data, but no more.

The present work fills a gap between these previous studies by measuring correlations in the $2p$ ground-state (g.s.) decay of the sd-shell nucleus ^{16}Ne where the Coulombic effects appear to be strong enough to be observable. Known experimentally for several decades [42], ^{16}Ne has remained poorly investigated with just a few experimental studies [17, 18, 15, 16]. However, interest has returned recently with the decay of ^{16}Ne measured in relativistic neutron-knockout reactions from a ^{17}Ne beam [43, 44]. We study the same reaction, but at an "intermediate" beam energy and obtain data with better resolution and smaller statistical uncertainty. Combined with state-of-the-art calculations, we have identified the role the long-range Coulomb interactions play in the measured three-body correlations.

Apart from the Coulomb interactions, predicted correlations show sensitivity to the initial $2p$ configuration and other final-state interactions previously identified in $2n$ decay [45, 46, 47]. Before the unambiguous statement can be made from the correlations related to short-range nuclear interactions, the effects of the long-range Coulomb interactions must first be

isolated and quantified.

4.2 Excitation Spectrum

The spectrum of the total decay energy E_T constructed from the invariant mass of detected ^{14}O+p+p events is shown in Fig. 4.1. Due to a low-energy tail in the response function of the Si ΔE detectors, there is leaking of a few ^{15}O ions into the ^{14}O gate in the $\Delta E - E$ spectrum. However, this contamination can be accurately modeled by taking detected ^{15}O+p+p events and analyzing them as ^{14}O+p+p. The resulting spectrum (dashed red curve) was normalized to the $\sim$ 1-MeV peak associated with 2^{nd}-excited state of ^{17}Ne. All the other observed peaks are associated with ^{16}Ne, with the g.s. peak at E_T = 1.466(20) MeV being the dominant feature. This decay energy is consistent with the value of 1.466(45) MeV measured in [15] and almost consistent with, but slightly larger than, other experimental values of 1.34(8) MeV [17], 1.399(24) MeV [18], and 1.35(8) MeV [43], 1.388(14) MeV [44].

The predicted spectra in Fig. 4.1, see below for details, provide guidance for possible spin-parity assignments of the other observed structures, suggesting that the previously known peaks [43, 44] at E_T = 3.16(2) and 7.60(4) MeV are both 2^+ excited states. The broad structure at $E_T \sim$ 5.0(5) MeV is well described as a 1^- "soft" excitation which is not a resonance, but a continuum mode, sensitive to the reaction mechanism [37]. In the mirror ^{16}C system, there are also $J = 2^{(\pm)}$, $3^{(+)}$, and 4^+ contributions in this energy range, but for neutron-knockout from $p_{1/2}$, $p_{3/2}$, and $s_{1/2}$ orbitals in ^{17}Ne, we should only expect *strong* population for 0^+ ($p_{1/2}$ knockout), 2^+ ($p_{3/2}$ knockout) and 1^- ($s_{1/2}$ knockout) configurations. I will concentrate on the g.s. for the remainder of this chapter ($1.27 < E_T < 1.72$ MeV) and all subsequent figures will show contamination-subtracted data.

4.3 Theoretical Model

The calculations used in this work were performed by Leonid Grigorenko and his group in Dubna, Russia. They are the leading group in calculating nuclear three-body decays, and the present study is the most recent joint effort between this theory group and our experimental group. The model used in this work is similar to that applied previously to ^{16}Ne [48] but with improvements concerning basis convergence [3], TBCD [41] and the reaction mechanism [36]. The three-body ^{14}O+p+p continuum of ^{16}Ne is described by the wave function (WF) $\Psi^{(+)}$ with the outgoing asymptotic obtained by solving the inhomogeneous three-body Schrödingier equation,

$$(\hat{H}_3 - E_T)\Psi^{(+)} = \Phi_{\mathbf{q}},$$

with approximate boundary conditions of the three-body Coulomb problem. The three-body part of the model is based on the hyperspherical harmonics method [3]. The differential cross section is expressed via the flux j induced by the WF $\Psi^{(+)}$ on the remote surface S:

$$\frac{d\sigma}{d^3k_{^{14}\mathrm{O}}d^3k_{p_1}d^3k_{p_2}} \sim j = \langle\Psi^{(+)}|\hat{j}|\Psi^{(+)}\rangle\Big|_S . \tag{4.1}$$

When comparing to the experimental data, the theoretical predictions were used in Monte-Carlo (MC) simulations of the experiment [24, 36] to take into account the bias and resolution of the apparatus.

The source function $\Phi_{\mathbf{q}}$ was approximated assuming the sudden removal of a neutron from the ^{15}O core of $^{17}\mathrm{Ne}_{\mathrm{g.s.}}$,

$$\Phi_{\mathbf{q}} = \int d^3r_n e^{i\mathbf{q}\mathbf{r}_n}\langle\Psi_{^{14}\mathrm{O}}|\Psi_{^{17}\mathrm{Ne}}\rangle\,, \tag{4.2}$$

where $\mathbf{r}_n$ is the radius vector of the removed neutron. The $^{17}\mathrm{Ne}_{\mathrm{g.s.}}$ WF $\Psi_{^{17}\mathrm{Ne}}$ was obtained in a three-body model of ^{15}O+p+p that had been previously tested against various observables

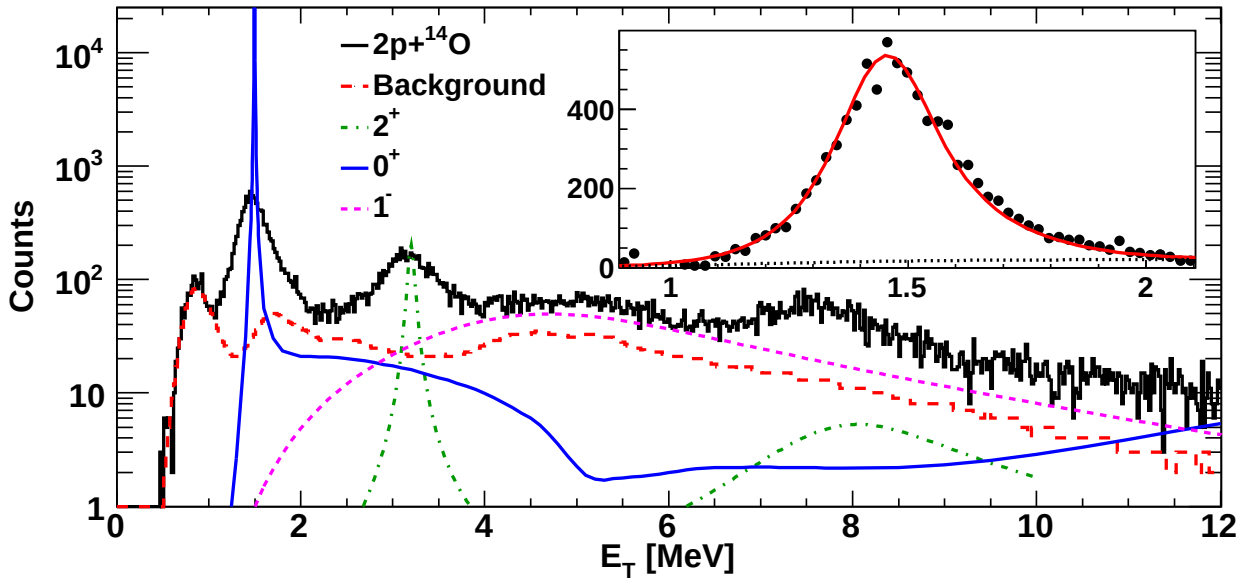

Figure 4.1: Experimental spectrum of ^{16}Ne decay energy E_T reconstructed from detected ^{14}O+p+p events. The dashed histogram indicates the contamination from ^{15}O+p+p events. The smooth curves are predictions (without detector resolution) for the indicated ^{16}Ne states. The inset compares the contamination-subtracted data to the simulation of the g.s. peak for $\Gamma = 0$, $f_{\rm tar} = 0.95$, where the dotted line is the fitted background.

[49]. Similar ideas had been applied to different reactions populating the three-body continuum of ^{6}Be [36, 38, 37]. The ^{14}O-p potential sets were taken from [48] which are consistent with a more recent experiment [50], providing $1/2^+$ and $5/2^+$ states at $E_r = 1.45$ and 2.8 MeV, respectively consistent with the experimental properties of these states in both ^{15}F and ^{15}C. For the p-p channel a smooth local potential was used that fit two nucleon data up to 300 MeV and reproduced properties of finite, closed shell nuclei [51].

The three-body Coulomb treatment in this model consists of two steps. (i) We are able to impose approximate boundary conditions of TBCD on the hypersphere of very large ($\rho_{\rm max} \lesssim$ 4000 fm) hyperradius by diagonalizing the Coulomb interaction on the finite hyperspherical basis [52]. Within this limitation the procedure is exact, however it breaks down at larger hyperradii as the accessible basis size become insufficient. (ii) Classical trajectories are generated by a MC procedure at the hyperradius $\rho_{\rm max}$ and propagated out to distances $\rho_{\rm ext} \gg \rho_{\rm max}$. The asymptotic momentum distributions are reconstructed from the set of

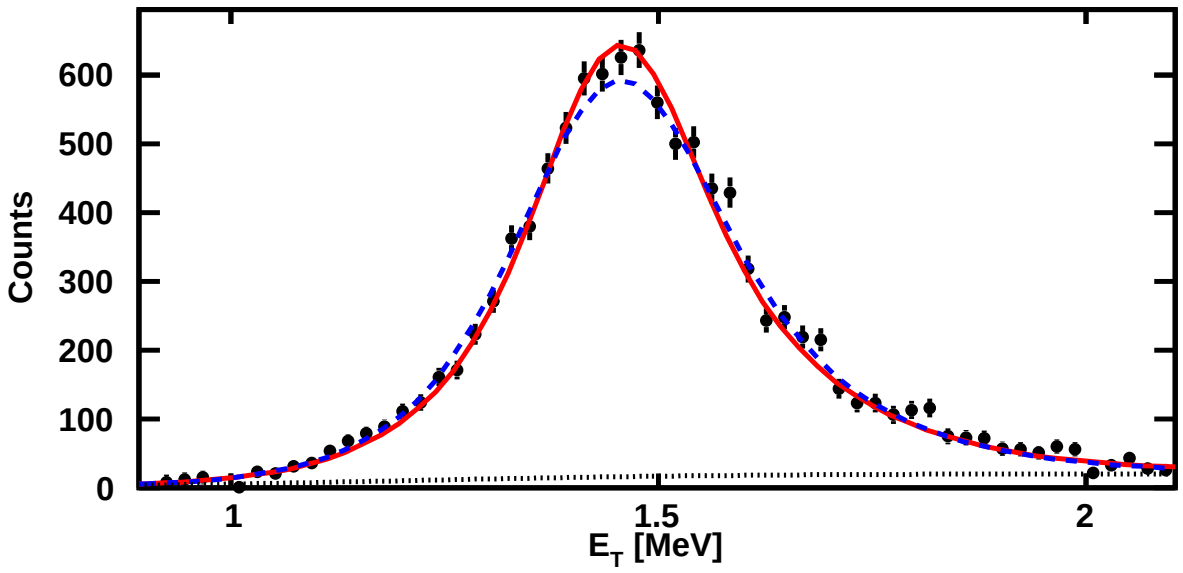

Figure 4.2: Comparison of simulated line shapes of the best fit (red curve) and 3σ upper limit (blue dashed curve) to the data. See text for description of fit parameters.

trajectories after the radial convergence is achieved. The accuracy of this approach has been tested in calculations with simplified three-body Hamiltonians allowing exact semi-analytical solutions [41].

4.4 Ground-state Width

The theoretical difficulty of reproducing the large experimental g.s. widths measured for ^{12}O and ^{16}Ne has been pointed out many times in the last 24 years [53, 54, 48, 55, 56]. For ^{12}O, this issue was resolved when a new measurement [57] gave a small upper bound. For ^{16}Ne, previous measurements of Γ=200(100) keV [17], 110(40) keV [18], and 82(15) keV [44] are large compared to the theoretical predictions, e.g. 0.8 keV in [48].

The experimental resolution is dominated by the effects of multiple scattering and energy loss in the target. Their magnitudes were fined tuned in the MC simulations by reproducing the experimental ^{15}O+p+p invariant-mass peak associated with the narrow (predicted life-time of 1.4 fs [58]) 2^{nd}-excited state in ^{17}Ne (see Chapter 8) by scaling the target thickness

from its known value by a factor $f_{\rm tar}$. The best fit is obtained with $f_{\rm tar}^{\rm fit} = 0.95$ with 3-σ limits of 0.91 and 1.00. With $f_{\rm tar}^{\rm fit}$, we find that the simulated shape of the ^{16}Ne$_{\rm g.s.}$ peak for $\Gamma = 0$ is consistent with the data (red curve in Fig. 4.2). To obtain a limit for Γ, we used a Breit-Wigner line shape in our simulations and find a 3-σ upper limit of $\Gamma < 80$ keV with $f_{\rm tar} = 0.91$ (blue dashed curve in Fig. 4.2). This limit is the first experimental result consistent with theoretical predictions of a small width [in the keV range, see, e.g. Fig. 4.4(a)]. However, out limit is still considerably larger than the predictions, and on the other hand, it is still consistent with two of the previous experiments so even higher resolution measurements are needed to fully resolve this issue.

4.5 Three-body Energy-Angular Correlations

As described in the introduction, the internal final state coordinates of a three-body decay can be completely described by two parameters: an energy parameter ε and an angle θ_k between the Jacobi momenta $\mathbf{k}_x$, $\mathbf{k}_y$:

$$\begin{aligned} \varepsilon = E_x/E_T\,, \qquad \cos(\theta_k) = (\mathbf{k}_x \cdot \mathbf{k}_y)/(k_x\, k_y)\,, \\ \mathbf{k}_x = \frac{A_2\mathbf{k}_1 - A_1\mathbf{k}_2}{A_1 + A_2}\,, \;\; \mathbf{k}_y = \frac{A_3(\mathbf{k}_1 + \mathbf{k}_2) - (A_1 + A_2)\mathbf{k}_3}{A_1 + A_2 + A_3}, \\ E_T = E_x + E_y = k_x^2/2M_x + k_y^2/2M_y, \end{aligned} \tag{4.3}$$

where M_x and M_y are the reduced masses of the X and Y subsystems. With the assignment $k_3 \rightarrow k_{^{14}\rm O}$, the correlations are obtained in the "T" Jacobi system where ε describes the (fractional) relative energy E_{pp} in the p-p channel. For $k_3 \rightarrow k_p$, the correlations are obtained in one of the "Y" Jacobi systems where ε describes the (fractional) relative energy $E_{\text{core-}p}$ in the ^{14}O-p channel.

The experimental and predicted (MC simulations) energy-angular distributions, in both Jacobi representations are compared in Fig. 4.3 and found to be similar. More detailed

comparisons will be made with the projected energy distributions.

The convergence of three-body calculations is quite slow for some observables [3, 59]. Figure 4.4 demonstrates the convergence, with increasing $K_{\max}$ (maximum principle quantum number of the hyperspherical harmonic method) for two observables for which the slowest convergence is expected. These calculations provide considerable improvement compared to the calculations of [48] which were limited to $K_{\max} = 20$.

To investigate the long-range nature of TBCD, we studied the effect of terminating the Coulomb interaction at some hyperradius $\rho_{\rm cut}$ (That is beyond $\rho_{\rm cut}$ the particles just free stream). The energy distribution in the "Y" Jacobi system is largely sensitive to just the TBCD and the global properties of the system (E_T, charges, separation energies) [2]. This makes it most suitable for studying the $\rho_{\rm cut}$ dependence [Fig. 4.5(a)]. Note that the theoretical MC results are always normalized to the integral of the data. The comparison with the data in Fig. 4.5(b) demonstrates consistency with the theoretical calculations only if the considered range of the Coulomb interaction far exceeds 10^3 fm ($\rho_{\rm cut} = 10^5$ fm guarantees full convergence). This conclusion is only possible due to the high quality of the present data. In contrast in [44], where the experimental width of the g.s. peak is almost twice as large and its integrated yield is ~ 3 times smaller, the corresponding ε distribution is broader with a FWHM of 0.41 compared to our value of 0.33. This difference is similar to that obtained over the range of $\rho_{\rm cut}$ considered in Fig. 4.5(a) demonstrating the need for high resolution to isolate the distorting effects due to the Coulomb interaction at distances far exceeding those at which the strong force can have an influence.

Our conclusions on TBCD are dependent on the stability of the predicted correlations to the other inputs of the calculations. Figure 4.5(d) demonstrates the excellent stability of the core-p energy distribution over a broad range ($\pm$200 keV) of E_T. Indeed, in this range we have a maximum in the width for this distribution due to the competition between two trends: (i) the distribution tends to $\varepsilon = 0.5$ in the limit $E_T \to 0$ [28], and (ii) some minimal width for the ε distribution is expected at $E_T \sim 2E_r$, where $E_r \sim 1.45$ MeV is the

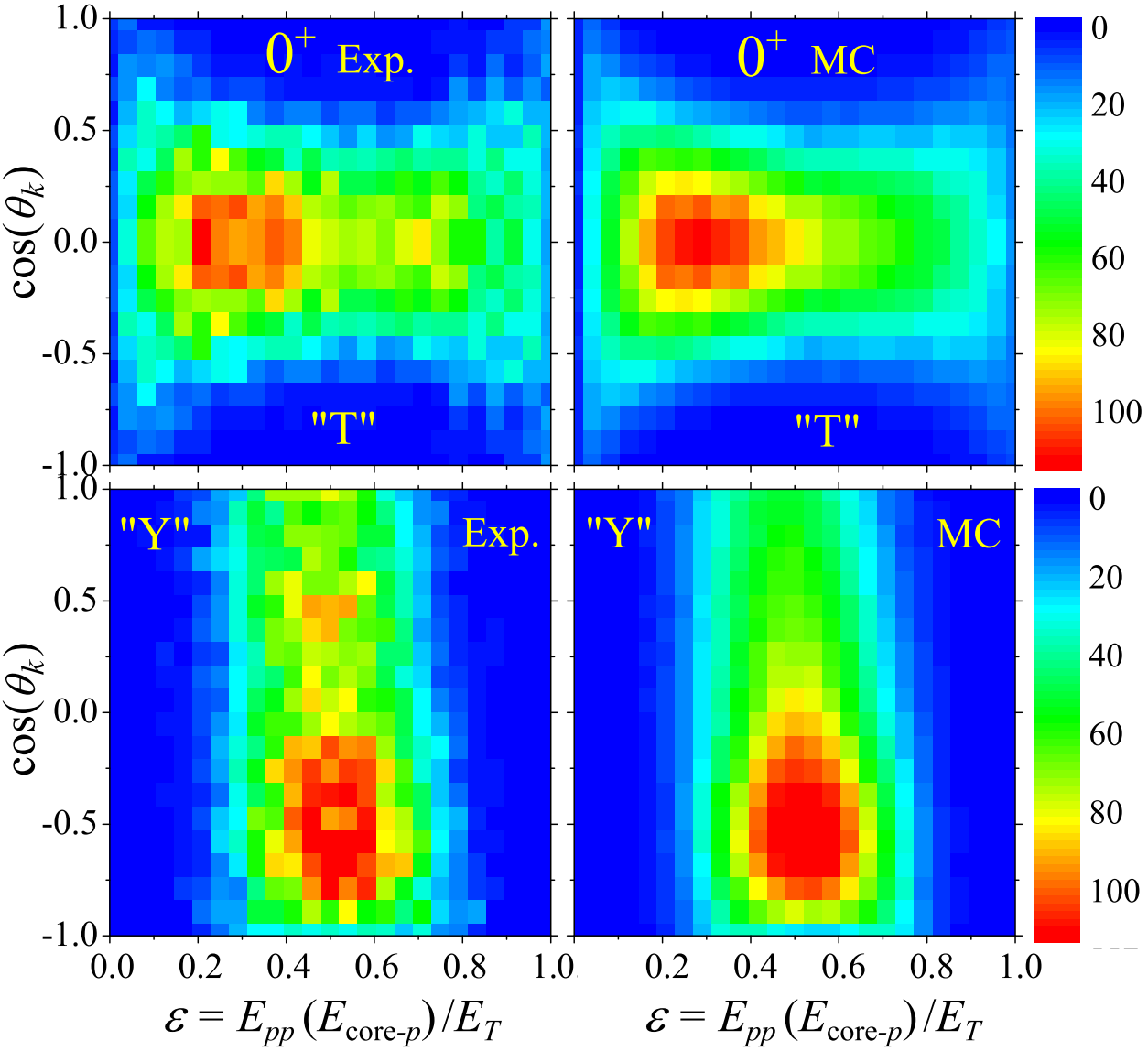

Figure 4.3: Energy-angular correlations for $^{16}\mathrm{Ne}_{\mathrm{g.s.}}$. Experimental and predicted (MC simulations) correlations for Jacobi "T" and "Y" systems are compared.

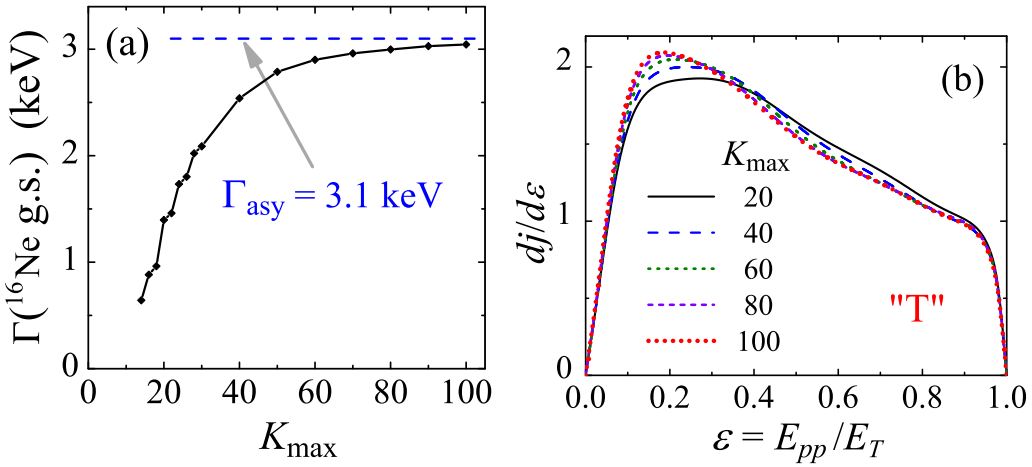

Figure 4.4: The convergence of the predicted (a) decay width and (b) energy distribution in the "T" system on $K_{\max}$ (maximum principal quantum number of hyperspherical harmonics method). The asymptotic decay width of ^{16}Ne assuming exponential $K_{\max}$ convergence is given in (a) by the dashed line.

$^{15}\mathrm{F}_{\mathrm{g.s.}} \rightarrow$ core $+ p$ decay energy. The predictions of such a "narrowing" [2] were recently proven experimentally [36]. The curve for $E_T = 1.976$ MeV is also provided in Fig. 4.5(d) to show that a really large change in energy is required to produce a significant modification of the ε distribution.

The other important stability issue is with respect to the properties of $^{15}\mathrm{F}_{\mathrm{g.s.}}$ for which there is *no agreement* on its centroid E_r and width [60]. Figure 4.5(c) shows predicted ε distributions based on four different ^{14}O+p interactions which give the indicated $^{15}\mathrm{F}_{\mathrm{g.s.}}$ properties. Even if we use the data from [61], which differs the most from the other results ($E_r \sim 1.23$ MeV instead of $E_r \sim 1.4 - 1.5$ MeV), no drastic effect is seen.

The evolution of the energy distribution between the two protons with ρ_{cut} is shown in Fig. 4.5(e). This distribution has greater sensitivity to the initial $2p$ configuration of the decaying system [2]. In addition, the spin-singlet interaction in the p-p channel provides the virtual state ("diproton") which also can affect the long-range behavior of the correlations (see [45, 46, 47] for the corresponding effects in $2n$ decay). The theoretical prediction for $\rho_{\mathrm{cut}} = 10^5$ fm in Fig. 4.5(f) reproduces the experimental data quite well, however, the sensitivity to ρ_{cut} is diminished compared to the core-p energy distribution.

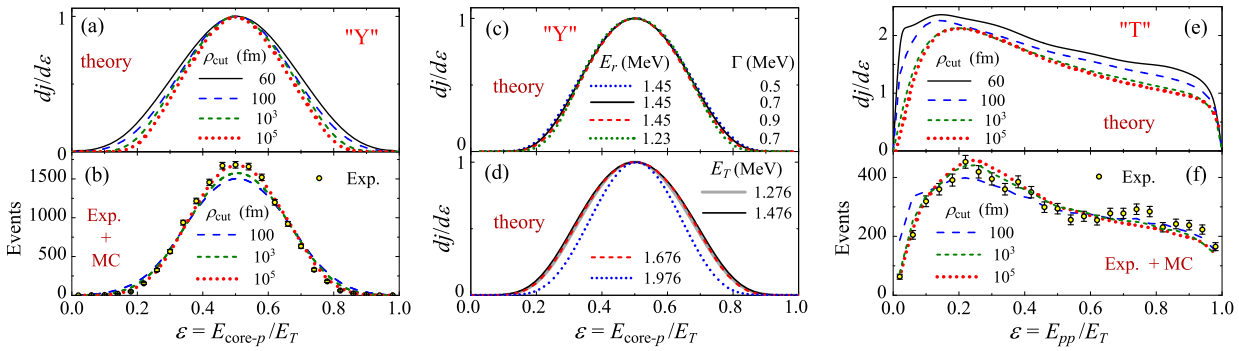

Figure 4.5: Panels (a)-(d) show energy distributions in the Jacobi "Y" system where (a) gives the sensitivity of the predictions to $\rho_{\rm cut}$, (c) to the ^{15}F$_{\rm g.s.}$ properties, and (d) to the decay energy E_T. Panels (e), (f) show energy distributions in the Jacobi "T" system where (e) gives the sensitivity to $\rho_{\rm cut}$. The theoretical predictions, after the detector bias is included via the MC simulations, are compared to the experimental data in (b) and (f) for the "Y" and "T" systems respectively. The normalization of the theoretical curves is arbitrary, while the MC results are normalized to the integral of the data.

In the model the very long distances are achieved by classical extrapolation. This approximation has been studied using calculations with simplified Hamiltonians where it was demonstrated that the classical extrapolation provides stable results if the starting distance $\rho_{\rm max}$ exceeds some hundreds of fermis for $E_T \sim 1$ MeV [41]. (e.g. ~ 300 fm for ^{19}Mg$_{\rm g.s.}$ decay where $E_T = 0.75$ MeV). At such distances, the ratio of the Coulomb potential to the kinetic energy of fragments is of the order 10^{-2}–10^{-3}. Figure 4.6 shows that for ^{16}Ne$_{\rm g.s.}$, the predictions are consistent with the data only if the conversion from quantum to classical dynamics is made at or above 200 fm.

4.6 Summary

The continuum of ^{16}Ne has been studied both experimentally and theoretically with emphasis on the ground state which decays by prompt two-proton emission. The measured decay correlations in this work were found to require a theoretical treatment in which the three-body Coulomb interaction is considered out to distances far beyond 10^3 fm. Our theoretical treatment is now validated for use in interpreting the results of future studies of heavier

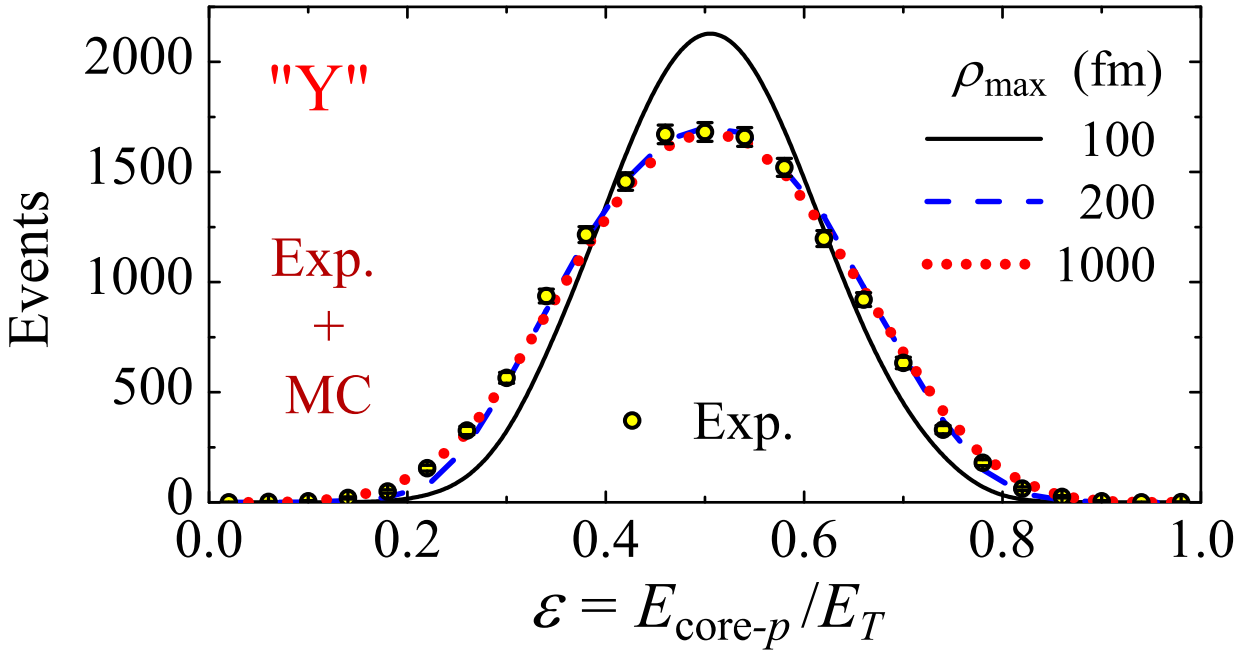

Figure 4.6: The core-proton relative-energy distribution ("Y" system) obtained by classical extrapolation started from different ρ_{max} values.

two-proton decay with particular emphasis on extracting nuclear-structure information from correlation observables.

We extract a limit of $\Gamma < 80$ keV for the intrinsic decay width of the ground state, and while this is not inconsistant with some of the previous measurements, it is the first measurement consistent with the theoretical predictions. All conclusions of this work were only possible due to the high statistics and fidelity of the present measurements.

Chapter 5

^{16}Ne Excited States

5.1 Background

Two-proton ($2p$) decay is most commonly considered as either of two extreme types: prompt or sequential. In the first case, which is also called "true" $2p$ decay, the two protons are emitted simultaneously in a three-body process. In sequential $2p$ decay, the two protons are emitted in two distinct steps of binary decay. If the intermediate system formed after the first step of single-proton decay is long-lived (narrow), then there will be no interactions between the two protons. Ground-state true $2p$ emitters occur where either no intermediate state is accessible via single-proton emission and/or the width of the intermediate state is wide compared to the single-proton decay energy [2]. For the excited states of such nuclei, these conditions may no longer apply and as the intermediate states become fully accessible by single-proton decay, it has generally been assumed that sequential decay will prevail. In this work we investigate such a case and show the transition from prompt to sequential is nontrivial.

In the previous chapter, I concentrated on the ground-state of ^{16}Ne which belongs to the class of true two-proton emitters [28, 2] because the ^{15}F $s_{1/2}$ ground state (g.s.) is not fully accessible by single-proton decay as indicated in the decay scheme of Fig. 5.1. The

experimental data used in that chapter has high statistics and excellent resolution allowing us to isolate the effect of the long-range, three-body, Coulomb interactions on the momentum distributions of the decay fragments. This effect was well reproduced by our three-body model thus validating its use with heavier $2p$ decays and allowing one to separate out the finer aspects of the decay dynamics.

Here, I continue the study of the ^{16}Ne continuum and consider the decay of the first excited, $J^\pi = 2^+$ state of ^{16}Ne. From the level scheme in Fig. 5.1, one expects that the decay of this state is sequential as the ^{15}F $s_{1/2}$ g.s. is fully accessible via one proton decay and the decay energy for this step is large compared to the width of this state. In this case, the decay energy could be efficiently shared between the degrees of freedom (first emitted proton and the motion of ^{15}F), which should provide favorable conditions for penetration. However, both the experimental data and calculations indicate that the real situation is much more complicated.

A similar problem was encountered in previous studies of the ^{6}Be continuum in Refs. [36, 38]. That work searched for the decay energy E_T at which true $2p$ decay is replaced by the sequential decay mechanism. In contrast to expectations, they found that such a transition *did not take place* in the whole observed energy range ($E_T < 10$ MeV). The decay remained of a complicated three-body nature even if some aspects of the decay correlations resembled the pattern expected for sequential decay. We now find similar results in the decay of the first-excited state of ^{16}Ne.

In ^{16}Ne, the Coulomb interaction is $\sim$4 times stronger than in ^{6}Be giving rise to higher Coulomb barriers and thus narrower states. Another difference is that the valence protons in ^{16}Ne belong to the *s-d* shell and is built on positive-parity single-particle excitations. It is interesting to see if these factors give rise to qualitative differences in the evolution of the decay mechanism with decay energy. This study will help us to predict the behavior for other *s-d* shell $2p$ emitters, for which similar quality data is not available.

Information on higher-lying excited states of ^{16}Ne is very sparse, apart from the observa-

tion of another excited 2^+ state in the ^{14}O+p+p exit channel at $E_T \sim 7.64$ MeV [43, 44, 5] and the possibility of a second 0^+ state at $E_T \sim 3.5$ MeV [16]. At even higher excitation energies, the ^{13}N+p+p+p exit channel opens and from its measured invariant-mass spectrum we find two new excited states.

5.2 ^{14}O+p+p Excitation spectrum

The distribution of ^{16}Ne decay energy E_T deduced from detected ^{14}O+p+p events via the invariant-mass method is displayed in Fig. 5.2. This spectrum has been corrected for a contamination from ^{15}O+p+p events where a small fraction of ^{15}O fragments have leaked into the ^{14}O gate in the $E - \Delta E$ spectrum. This correction is described in more detail in Chapter 4 where the raw uncorrected spectrum is also shown, Fig. 4.1.

The ^{16}Ne ground-state peak at $E_T = 1.466(20)$ MeV dominates the spectrum, but in this chapter I will concentrate on the smaller peak at $E_T = 3.16(2)$ MeV which has an excitation energy of $E^* = 1.69(2)$ MeV. In the ^{16}C mirror nucleus, the lowest excited states are a 2^+_1 state at $E^* = 1.766$ MeV and a 0^+_2 state at $E^* = 3.027$ MeV [62]. If the excited state observed in this work is the 0^+_2 state, then this would correspond to a very large Thomas-Ehrman shift of 1.3 MeV that would be ~ 1 MeV larger than that for the ground state. Recent theoretical calculations of the Thomas-Ehrman effect for ^{16}Ne-^{16}C mirror partners [63] predicted shifts ^{16}Ne 0^+_1 and 2^+ states are around $200 - 300$ keV. Therefore we believe this state at $E^* = 1.69$ MeV is the mirror of the 2^+_1 first excited state of ^{16}C. The energy of this peak is close to other levels observed in previous experiments, see the discussion of Sec. 5.7.

5.3 Width of the 2^+ state

Figure 5.2 shows a fit to the 2^+ peak using a Breit-Wigner line shape where the effects of the experimental resolution (and its uncertainty) are included via Monte Carlo simulations. The

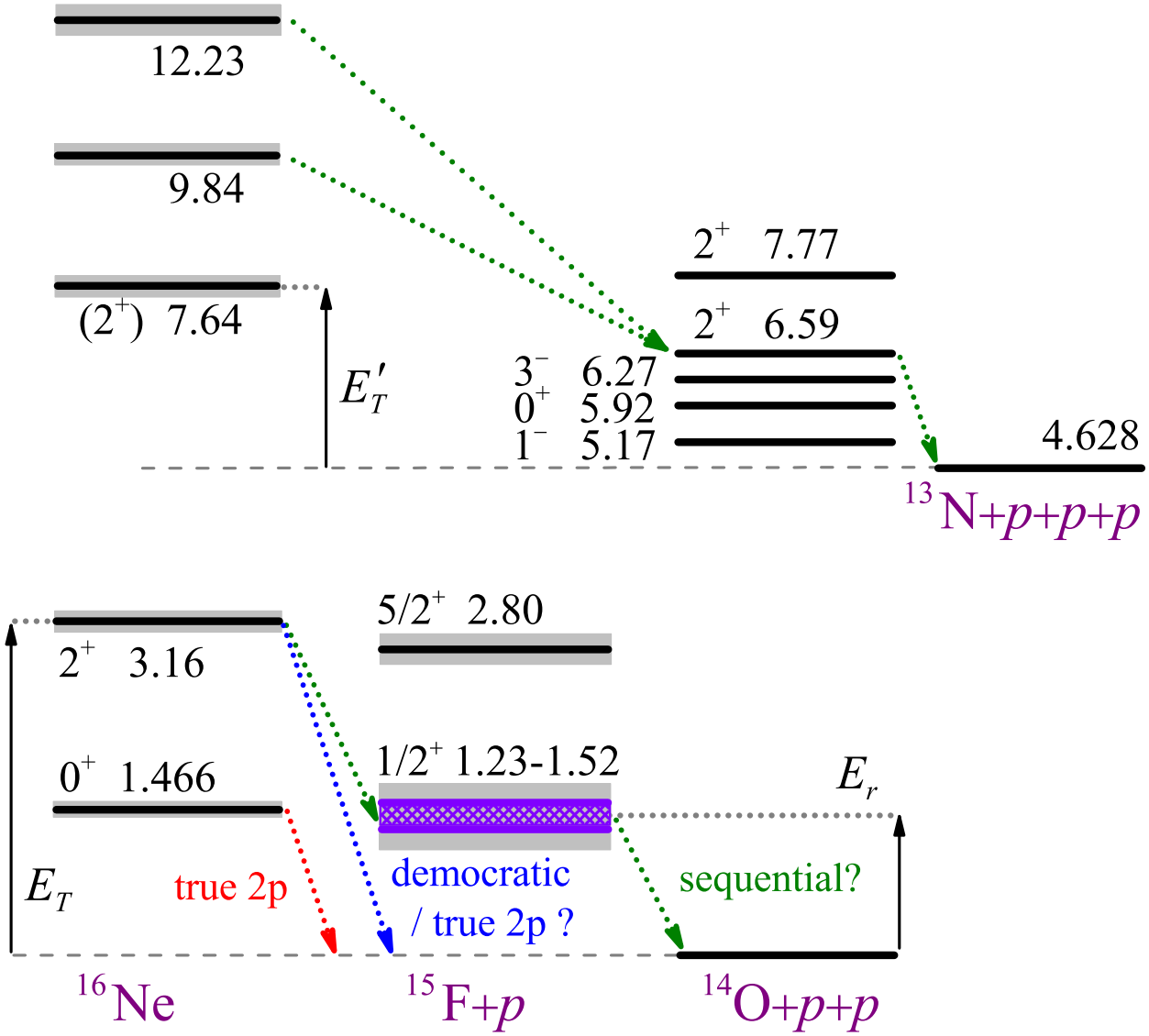

Figure 5.1: Low-lying levels of ^{16}Ne observed in this work and Ref. [5] and levels important for proton and multi-proton decay to ^{15}F, ^{14}O, and ^{13}N states. The experimental uncertainty of the ^{15}F g.s. energy is indicated by hatching. Note a reduction 1.5 in the scale above the ^{13}N+p+p+p threshold. All level energies are given with respect to the ^{14}O+p+p threshold.

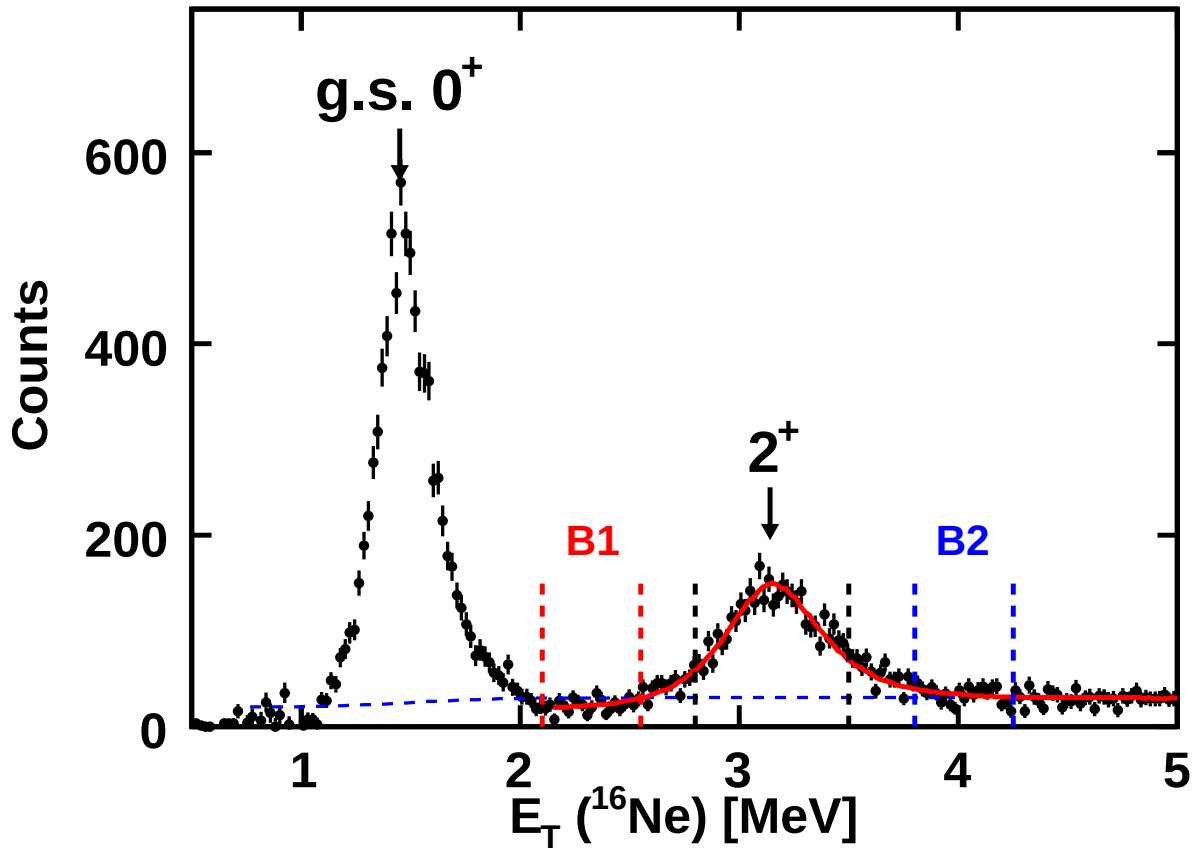

Figure 5.2: Distribution of ^{16}Ne decay energy determined from detected ^{14}O+p+p events showing peaks associated with the ground and first excited states of ^{16}Ne. The solid curve shows a fit to the first excited state where the dashed curves indicates the fitted background under this peak. Two background gates, $B1$ and $B2$, are shown which are used to investigate the background contributions to the measured decay correlations.

fit is shown by the solid line while the dashed curve indicates the fitted smooth, almost flat background. This fit is not unique as different functional forms of the background could be assumed. However, the relative magnitude of the background is small and the dependence on the exact form of the background is not large (see below). The extracted intrinsic width in this particular fit is $\Gamma = 150(50)$ keV where the error bar results predominately from the uncertainty associated with the effects of energy loss and small-angle scattering of the decay products in the target. See Ref. [5] for a discussion for this uncertainty. Upper limits to the width of this state were also obtained from the other neutron knockout experiments. Our extracted width is consistent with $\Gamma = 200(200)$ keV obtained in Ref. [43], but inconsistent with the limit of $\Gamma \leq 50$ keV from Ref. [44], see further discussion in the Section 5.7.

We have explored whether other choices of the background shape could result in significantly smaller values of Γ. If the background has a minimum under the peak, the extracted width would be smaller if the intrinsic width of this hypothetical minimum was less than 200 keV. Such a narrow "V"-shaped background seems unlikely, but in any case the depth of the such a minimum is limited as the intrinsic background (before the effects of detector resolution is applied) must always be positive. With this constraint, the observed background, after the effects of the experimental resolution is included, is always quite shallow for such narrow "V" backgrounds and produces a negligible change in the extracted value of Γ. On the other hand the use of wide "V"-shaped background can increase the extracted width. We estimate the maximum value of Γ from this and other uncertainties is 250 keV and finally we obtain $\Gamma = 175(75)$ keV.

5.4 Theoretical models

We continue to exploit the theoretical models developed by L. Grigorenko *et al.* To study the excited states we compare our data to two models both treating the decaying ^{16}Ne system as an inert ^{14}O core interacting with two protons. The first model is semianalytical with a

simplified Hamiltonian, and the second is a rigorous three-body cluster model. In principle three-body modles can yield: resonance energy, width as well as the correlations between the momenta of the decay products. The rigorous three-body model provides predictions for all of the above quantities while the simplified model is used to evaluate the width and, in case of sequential decay, the correlations can also be described reasonably well.

5.4.1 Simplified decay model

The width and momentum distributions in the "Y" Jacobi system can be estimated within the so-called "direct decay" R-matrix model presented in Ref. [2] where each proton is assumed to be in a resonant state of the core+p subsystem with resonant energy E_{j_i}. The differential flux for a system of total spin J is given by

$$\begin{aligned} \frac{dj^{(J)}_{j_1 j_2}(E_T)}{d\varepsilon\, d\theta_k} &= \frac{E_T \langle V_3 \rangle^2}{2\pi} f^{(J)}_{j_1 j_2}(\theta_k) \\ &\times \frac{\Gamma_{j_1}(\varepsilon E_T)}{(\varepsilon E_T - E_{j_1})^2 + \Gamma^2_{j_1}(\varepsilon E_T)/4} \\ &\times \frac{\Gamma_{j_2}((1-\varepsilon) E_T)}{((1-\varepsilon) E_T - E_{j_2})^2 + \Gamma^2_{j_2}((1-\varepsilon) E_T)/4}, \end{aligned} \tag{5.1}$$

where j_i is the angular momentum of a core+p_i subsystem. In this double differential, one variable is over the energy partition (ε) and the other the angular variable (θ_k), i.e. the Jacobi variables. This model corresponds to the simplified Hamiltonian of the three-body system in which the two protons interact with the core, but not with each other. It approximates the true three-body decay mechanism in a fashion that provides a smooth transition to the sequential-decay regime [59, 64]. It is essentially a single-particle approximation treating the decays of configurations $[j_1 j_2]_J$ independently and neglecting interactions between the valence nucleons. The quantity $\Gamma_{j_i}(E)$ is provided by the standard two-body R-matrix expression for the decay width as function of energy for the core+p_i resonance. The values $\Gamma_{j_i}(E_{j_i})$ correspond to the empirical values of the resonance widths in both core-nucleon subsystems i.

The angular-distribution function $f^{(J)}_{j_1 j_2}(\theta_k)$ in this model is obtained by coupling the single-particle angular functions with momenta j_1 and j_2 to total momentum J. This function does not always give realistic angular distributions [2]. However for the $[sd]$ configurations, dominating in the decay of the ^{16}Ne $J^\pi = 2^+$ state, $f^{(J)}_{j_1 j_2}(\theta_k)$ is expected to be isotropic.

The matrix element $\langle V_3 \rangle$ can be well approximated by

$$\langle V_3 \rangle^2 = D_3[(E_T - E_{j_1} - E_{j_2})^2 + (\Gamma^J)^2/4]\,,$$

where the parameter $D_3 \approx 1.0 - 1.5$ (see Ref. [64] for details) and Γ^J, the three-body decay width, is obtained selfconsistently from the FWHM of the distribution specified by Eq. (5.1).

The differential flux dj in Eq. (5.1) is normalized so that the three-body decay width is obtained by integrating over the two Jacobi coordinates,

$$\Gamma^{(J)}_{j_1 j_2}(E_T) = \int_0^1 d\varepsilon \int_{-1(diproton)}^{1(cigar)} d\theta_k \, \frac{dj^{(J)}_{j_1 j_2}(E_T)}{d\varepsilon \, d\theta_k}\,.$$

Typically for ground states there is only one configuration contributing significantly to the width, however for the 2^+ state, several configurations have non-negligible contributions and the total width is given by

$$\Gamma^{(J)}(E_T) = \sum_{j_1 j_2} W^{(J)}_{j_1 j_2} \Gamma^{(J)}_{j_1 j_2}(E_T)\,, \tag{5.2}$$

where $W_{j_1 j_2}$ are the weights of different configurations in the wavefunction (WF) for components with p-core spins of j_1 and J_2.

5.4.2 Three-body calculations

The three-body ^{14}O+p+p cluster model for the ^{16}Ne decay was originally developed by L. Grigorenko *et al* in Ref. [48]. Since that time this theoretical approach has developed

considerably [2] including a careful consideration of the Thomas-Ehrmann effect [63] and a precise treatment of the decay dynamics and long-range Coulomb effects as described in Chapter 4 and Ref [5]. The Thomas-Ehrmann effect is an energy-level shift seen for mirror states where in one you have a neutron in a $s_{1/2}$ orbital, and in the other it has been changed to a proton. Since this orbital has no angular momentum barrier, the Coulomb interaction will push the radius out to lower the energy. This is seen quite prominently in the first-excited states of ^{13}C and ^{13}N where they energy for the $1/2^+$ level has shifted down in ^{13}N (which has a proton instead of a neutron) by ~ 700 keV. Reference [63] provides a detailed up-to-date description of the model used for these ^{16}Ne calculations.

5.4.3 Three-body calculations

For the ground state of ^{16}Ne, our three-body calculations predict $\Gamma = 3.1$ keV which was found to be consistent with the upper limit we extracted for the intrinsic width of $\Gamma < 80$ keV [5]. Moreover, the model reproduces the experimental momentum correlations between the decay products with high precision. The decay mechanism of this state is the so-called true three-body decay and the hyperspherical method delivers very accurate results in this case.

The 2^+ state of ^{16}Ne can decay sequentially via the ^{15}F $s_{1/2}$ g.s. at $E_r \approx 1.4$ MeV and the first-excited, $d_{5/2}$ state at $E_r = 2.80$ MeV (see Fig. 5.1). The hyperspherical method is not as well suited for width calculations of states with important sequential decay channels and thus special care is required for the 2^+ calculation. For this level, the three-body calculations predict an intrinsic width of $\Gamma = 51$ keV for the largest basis size considered. The basis convergence of this result is studied in Fig. 5.3. The basis size is defined by $K_{\max}$, the maximum value of the principle quantum number K in the hyperspherical method. In our calculations, large basis sizes become available with the help of an adiabatic procedure ("Feshbach reduction", see e.g. Ref. [59]) that converts the calculation to one with a smaller basis size K_{FR}, which is then treated in a fully dynamical manner. It can be seen from

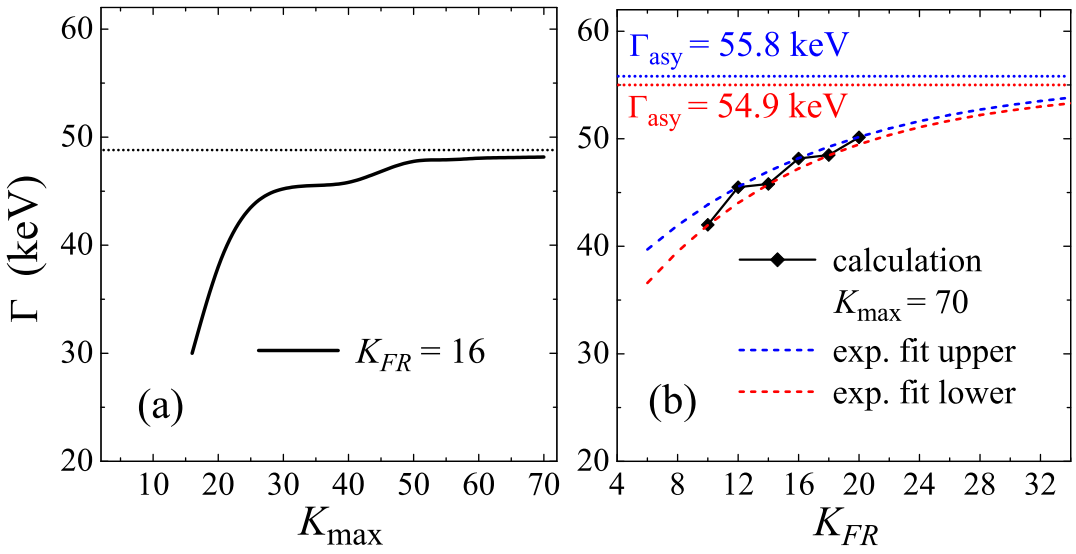

Figure 5.3: Convergence of the width calculations for the ^{16}Ne 2^+ state. (a) $K_{\max}$ convergence at a fixed K_{FR}. (b) K_{FR} convergence at a fixed $K_{\max}$. Exponential extrapolations (separately done for odd and even $K_{FR}/2$ values) point to a width of around $\Gamma = 56$ keV.

Fig. 5.3(a), that $K_{\max}$ convergence for a given K_{FR} is quite convincing. In contrast, K_{FR} convergence is not complete and displays some odd-even staggering with respect to $K_{FR}/2$. To estimate the final converged width at large K_{FR}, our collaborator L. Grigorenko performed exponential extrapolations separately for both odd and even $K_{FR}/2$ values [Fig. 5.3(b)]. The extrapolations provided very similar asymptotic values of $\Gamma \sim 56$ keV. Thus we regard this as the correct theoretical prediction. This value is smaller than the experimental result $\Gamma = 175(75)$ keV, and we do not see how the three-body calculations could be improved to match the experimental value.

5.4.4 Simplified decay model estimates

To investigate whether larger theoretical widths are possible, our collaborator performed calculations using the simplified decay model of Eq. (5.1). For the estimates provided in Table 5.1, he chose parameter sets in a reasonable way, by stretching all of them in the direction maximizing the width estimate. The channel radius $r_{\rm ch} = 4.25$ fm and the reduced width $\theta^2 = 1.5$ were used for all core+p resonances. The energies of the $p_{1/2}$ and $p_{3/2}$

resonances were assigned assuming isobaric symmetry between ^{15}F and ^{15}C states. The assumed energy of the $d_{3/2}$ resonance $E_{d_{3/2}} = 8$ MeV is also the minimal value which does not contradict the spectrum of ^{15}C.

The structure information on the $J^\pi = 2^+$ ^{16}Ne state in Table 5.1 is taken from Ref. [63]. However, for this table we required a more detailed decomposition than was provided in the that work. In spite of the simplicity of the model, the total width of the 2^+ state evaluated according to Eq. (5.2) is found to be around $\Gamma = 51$ keV in a good agreement with the three-body calculations of Sec. 5.4.3 (I remind the reader that this value is inconsistent with our experimental value).

As shown in Table 5.1, there are two ways to increase the estimated width: (i) decrease in the energy E_r of the ^{15}F $s_{1/2}$ ground state or (ii) drastically increase the $[s_{1/2}d_{5/2}]_{2^+}$ configuration weight. In both cases, the calculated widths remain at the lower limit of the experimental uncertainty. In evaluating these possible modifications one should consider their consistency with structure of the mirror states. The Thomas-Ehrman effect and the Coulomb displacement energies for the 0^+ and 2^+ states of the ^{16}Ne-^{16}C isobaric mirror partners were studied in detail in Ref. [63]. A sensitive relationship was found between the energies of the 0^+ and 2^+ states, their structures, and the ^{15}F $s_{1/2}$ ground-state energy. The latter was fixed in the calculations at $E_r = 1.405(20)$ MeV using our experimental values for the ground and 2^+ states of ^{16}Ne, Chapter 4. It is very difficult to drastically change the spin structure of predicted WF without a catastrophic effect on the consistency with the experimental energies of the 0^+ and 2^+ states achieved in Ref. [63]. Thus, a complete revision of the theoretical understanding of ^{16}Ne and ^{15}F systems is required to allow realization of the variants proposed in (i) and (ii).

5.4.5 Outlook for 2^+ state width

Given that the experimental width of the 2^+ state is larger than expected, it is useful to examine if there could be additional contributions to the ^{16}Ne excitation spectrum which

Table 5.1: Simplified-decay-model estimates of important configurations of the ^{16}Ne 2^+ WF for D_3=1.0. The total decay width according to Eq. (5.2) is provided in the line "Total". The sensitivity of the three-body width to variations of the ^{15}F g.s. energy is illustrated by the three bottom lines of the Table.

$[l_{j_1} l_{j_2}]_{J^\pi}$	$W^{(2)}_{j_1 j_2}$ (%)	E_{j_1} (MeV)	E_{j_2} (MeV)	$\Gamma^{(2)}_{j_1 j_2}$ (keV)
$[p_{1/2}p_{3/2}]_{2^+}$	3.0	4.5	6.0	11
$[p^2_{3/2}]_{2^+}$	1.1	6.0	6.0	7
$[d^2_{3/2}]_{2^+}$	1.2	8.0	8.0	0.04
$[d^2_{5/2}]_{2^+}$	5.4	2.8	2.8	1.6
$[s_{1/2}d_{3/2}]_{2^+}$	71.3	1.4	8.0	50
$[s_{1/2}d_{5/2}]_{2^+}$	15.9	1.4	2.8	93
Total	97.9			50.9
$[s_{1/2}d_{5/2}]_{2^+}$	15.9	1.2	2.8	113
$[s_{1/2}d_{5/2}]_{2^+}$	15.9	1.3	2.8	103
$[s_{1/2}d_{5/2}]_{2^+}$	15.9	1.5	2.8	89

overlap with the 2^+ state. One such possibility is that the peak we observed is actually a doublet with contributions from both the 2^+_1 and the 0^+_2 levels. Föhl *et al.* [16] report a 0^+_2 excited state at $E^* = 2.1(2)$ MeV [with corresponding $E_T = 3.57(20)$ MeV] in the ^{16}O(π^+,π^-) reaction. This energy is a 2σ difference from our fitted centroid, but overlaps with the observed peak.

In the three-body calculations [5], the 0^+_2 state is predicted in the range $E^* = 2.9 - 3.2$ MeV, well separated from the observed peak and consistent with the energy of the $E^* =$ 3.03-MeV state in ^{16}C which is expected to be the 0^+_2 mirror partner. Furthermore, the three-body calculations of Ref. [5] indicate that the 0^+ excitation function for ^{16}Ne has a dip, and not a peak, at the predicted energy of the 0^+_2 state, see Fig. 4.1. In these ^{17}Ne$(-n) \rightarrow ^{16}$Ne neutron-knockout calculations , the 0^+_2 state is strongly suppressed as the overlap of the valence-proton configurations for the ^{17}Ne ground state with those of the ^{16}Ne ground state (0^+_1 state) is so strong that there is little room for yield from the 0^+_2 state. This assumed ^{17}Ne structure is regarded as quite realistic as it was found to lead to an excellent agreement with a broad range of observables [49]. Of course, the ^{17}Ne structure or the reaction mechanism maybe more complicated than assumed in the calculations. Furthermore, the data of Föhl

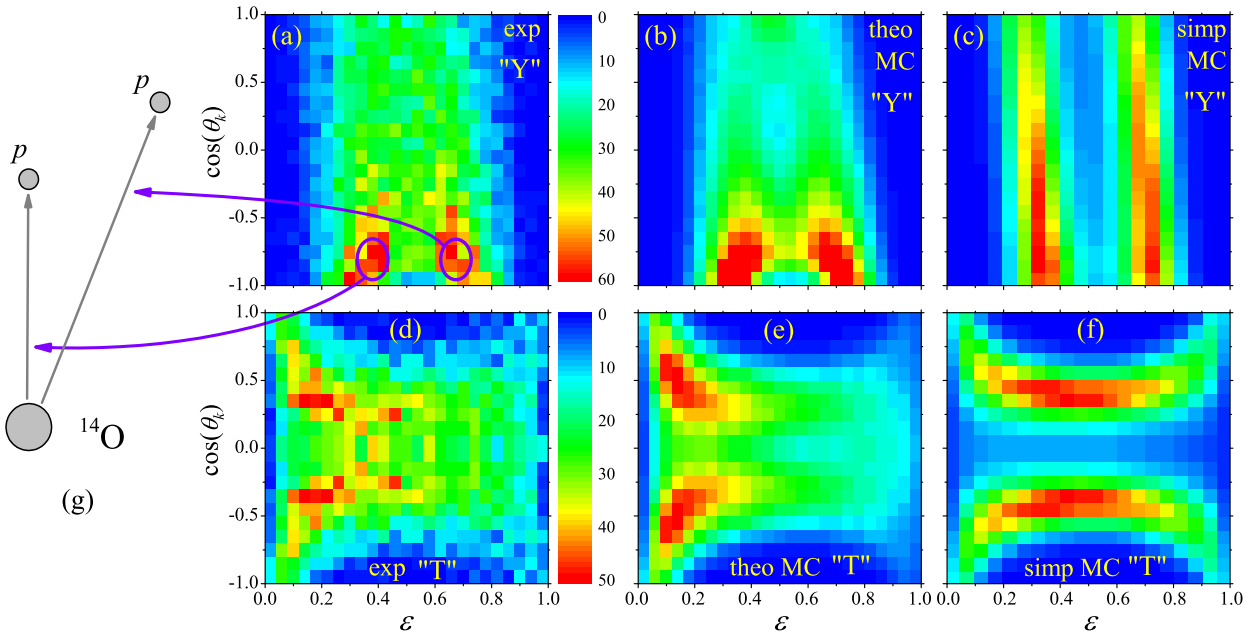

Figure 5.4: Comparison of the experimental Jacobi (a) "Y" and (d) "T" correlation distributions to the those of the three-body model [(b) and (e)] and those from a sequential decay simulation [(c) and (f)]. The effects of the detector efficiency and resolution in the theoretical distributions have been included via Monte Carlo simulations. (g) Shows the relative orientation and magnitude of the two proton velocity vectors for the peak regions indicated by blue circles in panel (a).

et al. and the calculations of Ogawa *et al.* [65] suggest that the location of this state could be much closer to our observed peak. In summary, it is clear that we do not fully understand the magnitude of the width of the 2^+ state and that this issue is strongly related to excitation energy of the 0_2^+ state and its population in these neutron knockout reactions. While the possibility of contamination from the 0_2^+ and width issue will remain unresolved, the remained of this chapter will proceed assuming the state is entirely 2^+ in character.

5.5 Correlations for 2^+ state

The experimental two-dimensional Jacobi "Y" and "T" correlations for the 2^+ state are shown in Figs. 5.4(a) and 5.4(d), respectively. The E_T gate used to select this peak is indicated in Fig. 5.2. Both distributions show the presence of two ridge structures, and

indeed double-ridge structures are expected for sequential decay. The location of these ridge structures along the Jacobi "Y" energy axis correspond qualitatively to those expected from the decay via the $s_{1/2}$ ground state of ^{15}F with $E_r \sim 1.4$ MeV. However, these ridge structures are very pronounced and intense only in the diproton halves of the distributions [small ε in the Jacobi "T" or $\cos(\theta_k) < 0$ in the Jacobi "Y" distribution]. For the other halves of the distributions, the overall intensity is reduced and the ridge structures have largely faded out. These features can also be seen in the projected energy distributions for the two Jacobi systems plotted in Figs. 5.5(a), 5.5(c), and 5.6. The geometry of the most probable decay configurations, associated with the more intense regions of the ridges, is illustrated in Fig. 5.4(g) (left).

5.5.1 Background contribution to correlations

Before discussing the correlations from our two models, it is useful to consider the contributions of the background under the $J^\pi = 2^+$ peak. From the fit shown in Fig. 5.2, we estimate that our energy gate spanning the excited-state peak contains a 24% background contribution. Background gates, $B1$ and $B2$, were placed either side of this peak (see Fig. 5.2) to investigate the correlations associated with this background. The number of events in these background gates is too small to obtain useful information from the two-dimensional distributions, so we will concentrate on the projected distributions. The projected energy distributions in both the "T" and "Y" systems are compared for the main and background gates in Figs. 5.5(a) and 5.5(c). The results for the each background gates have been normalized to 24% of the peak yield and the error bars are less than the size of the data points.

We should emphasize here that the "background" is expected to be largely a "physical background" from decay of unresolved ^{16}Ne states. For example, based on the theoretical calculations of Ref. [5], the $B1$ gate contains contributions from the large high-energy tail of the ground state and the $B2$ has contributions from a wide 1^- state.

For the Jacobi "Y" system shown in Fig. 5.5(a), there are significant differences between

the two background distributions. The $B2$ distribution has a double-peak structure much like that obtained for the excited-state gate, but the two peaks are separated further apart in energy as would be expected for sequential decay of a higher-lying ^{16}Ne level decaying through the ^{15}F ground state. In fact, the peak locations roughly match the expectation from a sequential calculation with the simplified model (Sec. 5.5.2) which are indicated by the arrows. For the $B1$ gate, there is only a single peak at $\varepsilon \sim 0.5$, but this is expected from Eq. (5.1) for a such small E_T value. If the energy projection for the background under the peak is intermediate between the $B1$ and $B2$ projections, then it will have a two-peak shape similar to the peak-gated projection. Note the magnitude of the two peak structure in the peak-gated distribution is too large to be entirely due to this background, therefore the presence of the background only contributes moderately to this feature.

On the other hand for the Jacobi "T" system in Fig. 5.5(c), the two background distributions are quite similar and therefore it is reasonable to assume the background under the peak has a similar, almost flat, dependence. As such, its contribution does not alter the measured distribution significantly. The data in Fig. 5.5(d) shows the Jacobi "Y" energy distribution after the average of the $B1$ and $B2$ gates are subtracted. It is not significantly different from the original distribution in Fig. 5.5(c). A similar subtraction is also made for the Jacobi "Y" distribution in Fig. 5.5(b), but in this case it is not clear how appropriate this is. However, the change in shape from the original distribution in Fig. 5.5(a) is again minor.

If the observed $E_T = 3.15$ MeV peak is a doublet, as discussed in Sec. 5.4.5, and the correlations for the two states are different, then one might see an E_T dependence of the correlations within the E_T range of the peak. No evidence for such an effect was observed. The only observed dependence of statistical significance is small shifting of the energies of the two peaks which follows the expected E_T dependence for decay through the ^{15}F ground state.

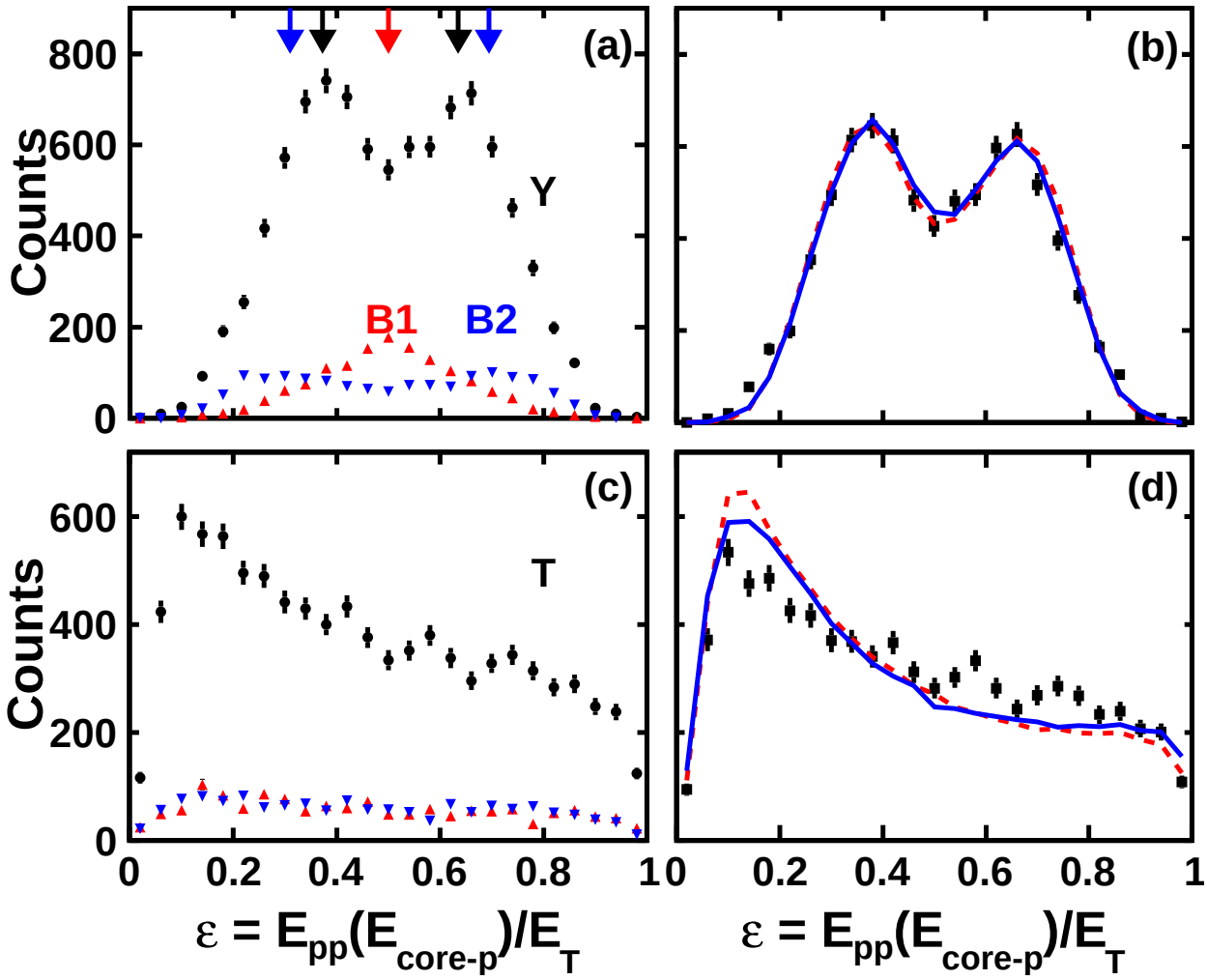

Figure 5.5: Comparison of projected Jacobi (a) "Y" and (c) "T" energy distributions for peak-gated events and the events in the neighboring background gates $B1$ and $B2$. In (b) and (d) the experimental projections have been background subtracted (see text) and are compared to the predictions of the three-body model before (dashed curves) and after (solid curves) the effects of the detector bias and acceptance was included. The arrows in (a) show the predicted locations of the maxima from Eq.(5.1) for the mean energies of each of the three gates.

5.5.2 Correlations in the simplified model

In the simplified model [Eq. (5.1)], the double-ridge distribution of Fig. 5.4(a) is dependent on the energy E_r of the ground state $s_{1/2}$ resonance in ^{15}F. However, this energy is not well defined experimentally with results varying from 1.23 to 1.52 MeV, see e.g. the discussion and references in Refs. [60, 63]. Figure 5.6 demonstrates the strong sensitivity of the simplified model to the value of E_r. This result, for the first excited state, is in stark contrast to the ground state where we found the "Y" system energy distribution was insensitive to realistic variations of E_r. The range of E_r consistent with the data in Fig. 5.6 is $1.4 \lesssim E_r \lesssim 1.5$ MeV which is also consistent with the range $1.39 \lesssim E_r \lesssim 1.42$ MeV determined from an analysis of Coulomb displacement energies [63]. Also see the discussion of the ^{15}F ground state in Sec. 5.4.4.

A detailed view on the correlations from the simplified model is presented in the two-dimensional distributions shown in Figs. 5.4(c) and 5.4(f). These distributions were calculated with $E_r = 1.405$ MeV [63] and the effects of the detector efficiency and resolution were included via the Monte Carlo simulations. Both distributions show the expected double-ridge structures. The sequential aspect of the decay is most easily understood in the Jacobi "Y" distribution of Figure 5.4(c). Here the two-ridge structures are prominent over the whole angular range. The angular distribution functions $f^{(J)}_{j_1 j_2}(c_k)$ are isotropic for all the contributions in Table 5.1 except for the minor $[p^2_{3/2}]_{2^+}$ and $[d^2_{5/2}]_{2^+}$ components. Therefore ridges are predicted to have uniform intensity as a function of $\cos(\theta_k)$ and the small dependence seen in Fig. 5.4(c) is just due to the detector acceptance. The use of smaller values of E_r in these simulations would result in the same basic picture, but the separation between the ridges would be increased (as the two decay steps would become more skewed in E_{core-p} partition) and the match with the experimental ridges at low ε values would be worse.

Comparing the data and sequential simulations, we find that the experimental distribution looks sequential only in the regions were there are strong p-p final-state interactions suggesting that the decay is sequential only when it is also of diproton nature and vice versa

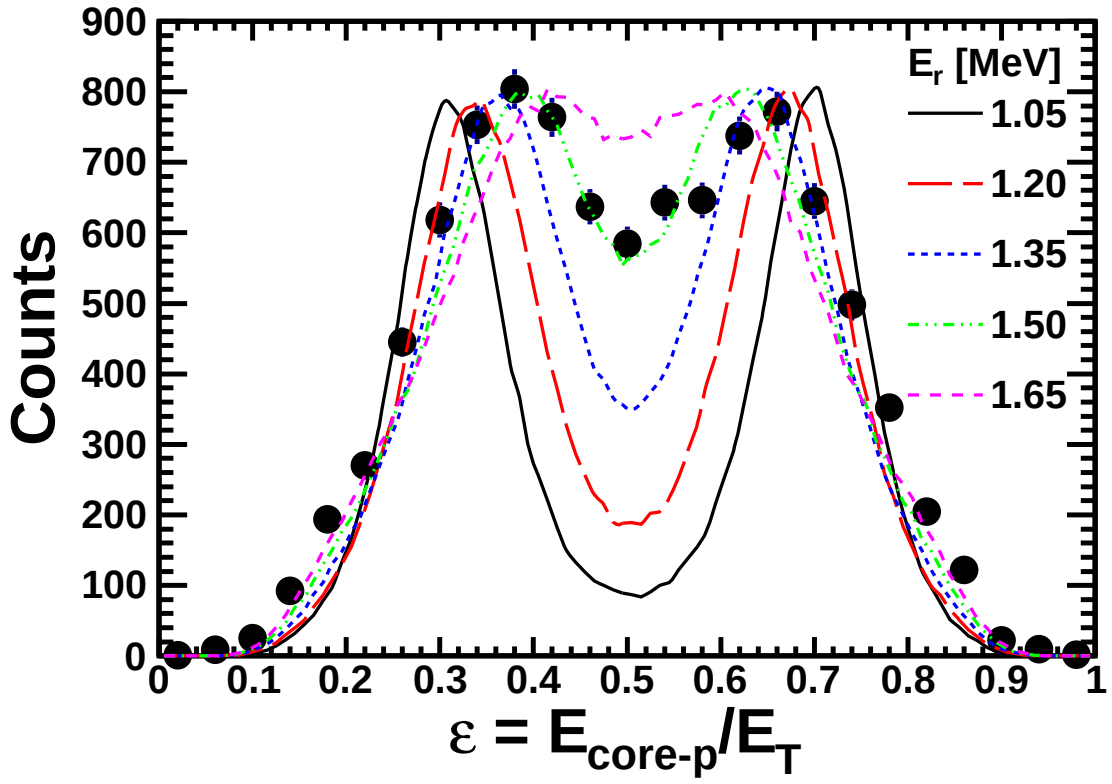

Figure 5.6: Experimental energy distribution for ^{16}Ne 2^+ state in the "Y" Jacobi system (data points) is compared with distributions calculated by the R-matrix-type expression of Eq. (5.1) for the different $s_{1/2}$ g.s. resonance energies E_r in ^{15}F listed in the figure. The detector efficiency and resolution were included via the Monte Carlo simulations.

which seems nonsensical. The "diproton" regions are those with small ε in "T" system and $\cos(\theta_k) \sim -1$ for medium ε values in "Y" system. The actual geometry of the most probable decay configuration is visualized in Figure 5.4(g). Clearly the decay mechanism is more complicated than this intuitively-simple sequential picture.

The apparent conflict between features that look sequential in the "Y" energy distribution and features indicating strong p-p final-state interactions in the "T" energy distribution was also noted in the decay of highly-excited states of ^{6}Be [36]. As the ^{6}Be results are qualitatively consistent with the present work, then it seems that the detailed structure of the state and the magnitude of the Coulomb barriers are not responsible for explaining these common and unexpected correlations.

5.5.3 Comparison with three-body calculations

The predicted two-dimensional correlations from the three-body model, after the effects of detector bias and resolution are included via the Monte Carlo simulations, are shown in Figs. 5.4(b) and 5.4(e) for the two Jacobi systems. These three-body calculations reproduce the major features of the experimental results. Like the experimental data, the "sequential-decay" ridges are clearly present and pronounced only in the diproton region. The agreement is not perfect. For example, the three-body calculations predict a "hole" in two-dimensional distributions that is most obvious in the Jacobi "Y" distribution of Fig. 5.4(b) where it is centered at $\{\varepsilon = 0.5, \cos(\theta_k) \sim 0.3\}$. This feature, if present at all in the experiment data, is significantly reduced. However, it should be noted that the experimental distribution are expected to contain $\sim 24\%$ background which will make such a fine feature difficult to see.

More detailed quantitative comparisons are made in Figs. 5.5(b) and 5.5(d), where the projected energy distributions are compared to the data. The predictions before and after accounting for the effects of the detector bias and resolution are similar as indicated by the dashed and solid curves, respectively. The two-peak structure is well reproduced in the projection for the Jacobi "Y" distribution in Fig. 5.5(b). In the Jacobi "T" distribution of

Fig. 5.5(d), the three-body model also predicts an appropriate enhancement of the diproton region (small ε), but the magnitude of the effect is somewhat larger than that observed experimentally. As mentioned above, a similar result was obtained for the highly-excited continuum of ^{6}Be [36]. We note that computation of the "Y" ε distribution is sensitive to model parameters like the resonance energy E_r of ^{15}F ground state. In contrast, the "T" ε distribution is much less sensitive to these parameters and very stable in various computation conditions. It is also possible that this disagreement is related to uncertainties in the background contribution, however it is the "T" background that seems better constrained than the "Y" background (Sec. 5.5.1).

5.6 Decay mechanism for 2^+ state

The three-body calculations reproduce the diproton and sequential features of the experimental distributions. In order to better understand the origin of these unusual momentum correlations we have examined the radial evolution of the decay WF $\Psi^{(+)}$. Figure 5.7 shows the correlation density

$$W(\rho,\theta_\rho) = \int d\Omega_x\, d\Omega_y\, |\Psi^{(+)}(\rho,\theta_\rho,\Omega_x,\Omega_y)|^2$$

as a function of the hyperangle and hyperradius in the Jacobi "Y" system. The Jacobi vectors $\mathbf{X}$ and $\mathbf{Y}$ in this system, illustrated in Fig. 5.7(c), are defined via the hyperspherical variables as

$$\begin{aligned}
\rho^2 &= \tfrac{A_1A_2}{A_1+A_2}\,X^2 + \tfrac{(A_1+A_2)A_3}{A_1+A_2+A_3}\,Y^2 = \tfrac{14}{15}\,X^2 + \tfrac{15}{16}\,Y^2\,, \\
X &= \rho\sqrt{\tfrac{A_1+A_2}{A_1A_2}}\sin(\theta_\rho) = \rho\sqrt{\tfrac{15}{14}}\sin(\theta_\rho)\,, \qquad (5.3)\\
Y &= \rho\sqrt{\tfrac{A_1+A_2+A_3}{(A_1+A_2)A_3}}\cos(\theta_\rho) = \rho\sqrt{\tfrac{16}{15}}\cos(\theta_\rho)\,, \qquad (5.4)
\end{aligned}$$

where in the "Y" system $A_1 = A_{core}$ and $A_2 = A_3 = 1$. The mid point of the θ_ρ-axis in Figs.

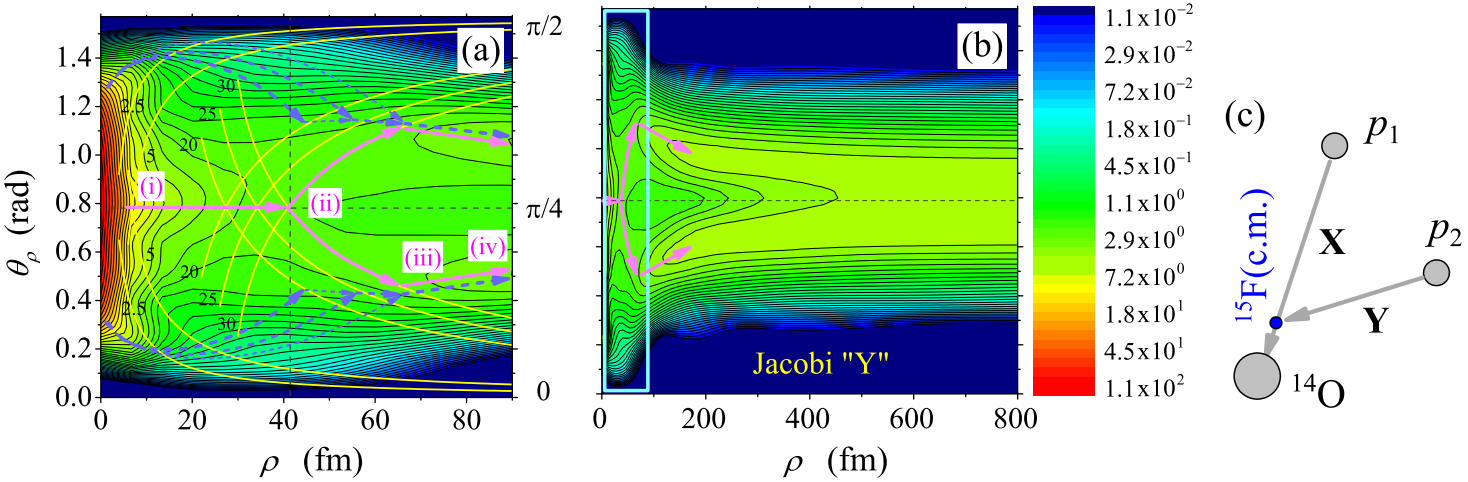

Figure 5.7: Correlation density $W(\rho, \theta_\rho)$ for ^{16}Ne 2^+ state WF $\Psi^{(+)}$ in the "Y" Jacobi system. Panels (a) and (b) show the evolution of the predicted hyperangular distribution with hyperradius on two different scales. Yellow curves in (a) provide the levels with constant absolute values of $\mathbf{X}$ and $\mathbf{Y}$ vectors indicated by the attached numbers (in fm). Blue (dashed) and pink (solid) arrows qualitatively indicate the classical paths connected with sequential and the "tethered" decay mechanisms correspondingly. The blue frame in the panel (b) shows the scale of panel (a). Panel (c) illustrates the arrangement of the $\mathbf{X}$ and $\mathbf{Y}$ vectors for the "Y" Jacobi system, see Eqs. (5.3) and (5.4).

5.7(a,b) approximately corresponds to equal projections of the hyperradius on the **X** and **Y** vectors defining the positions of p_1 and p_2 respectively, i.e.

$$\theta_\rho \sim \pi/4 \quad \rightarrow \quad X \sim Y \sim \rho/\sqrt{2}\,.$$

For large ρ values, the coordinate-space hyperangle θ_ρ transforms into momentum-space hyperangle $\theta_\varkappa$ defining the energy distribution between the subsystems:

$$\theta_\rho \rightarrow \theta_\varkappa, \quad E_x = E_T\,\sin^2(\theta_\varkappa), \quad E_y = E_T\,\cos^2(\theta_\varkappa). \tag{5.5}$$

Thus the representation of Figs. 5.7(a,b) best illustrates the geometry of the single-particle configurations.

The population density in Fig. 5.7(a) is very large for typical nuclear dimensions $\rho < 5$ fm where the two protons are inside the Coulomb barrier. This indicates the region of resonant-state formation. Extending out from this region are ridges associated with different decay paths.

Classical trajectories for sequential decay, differing in the decay time of the ^{15}F intermediate state are indicated by the dashed (blue) arrows. The initial portion of these trajectories is common to all sequential decays (one of the protons is emitted while the other remains close to the core) and they follow lines of roughly constant, but small, values of either X or Y. The presence of the ridges in Fig. 5.7(a), which are roughly parallel to the yellow lines shown for constant $X = 2.5$ or $Y = 2.5$ fm, confirms that there is a sequential component in these three-body calculations. The classical trajectories deviate from these ridges when the second proton is emitted and at this stage the classical trajectories diverge and so this part of the decay is not reflected by a ridge structure in the WF and thus is less visible. However, the decay paths do eventually concentrate at larger ρ values along the two well-defined ridges which are clearly seen in Fig. 5.7(b).

The other prominent penetration path in the three-body calculations, schematically in-

dicated by solid (pink) arrows, is more unusual. One observes a well-defined ridge in the range (i)-(ii) in Fig. 5.7(a) extending out from the main concentration of contours. For this ridge, $X \sim Y$ and thus the protons are penetrating the barrier simultaneously. The density in this ridge within the range (i)-(ii) again decreases exponentially with ρ. Simultaneous emission of protons is of course a well established decay mechanism [2]. However, the emission dynamics changes in the range (ii)-(iii). Here the arrows more closely follow the lines of constant X and Y which means that radial motion of one of the protons is now practically stopped (much slower than the orbital motion), while the other continues to move in the radial direction. Finally in the range (iii)-(iv) are two symmetric ridges which smoothly evolve with ρ to the "sequential-decay" double-hump structures observed in the energy distribution of Fig. 5.5(b). This region is common for both the initial sequential and prompt decay paths and both protons are more or less in the state of free flight except for the effect of the long-range Coulomb interaction. This behavior implies that in the evolution along the path (i)-(iv), the "near" proton leaves its position adjacent to the core at point (iii) starting the expansion stage of the whole system. At this moment even the "near" proton is already far beyond the typical nuclear size relative to the core and thus the WF component evolving along the (i)-(iv) pathway cannot "remember" information about core-p interaction. However, the sequential trajectories merge with this decay path at this point and from Eq. (5.5), the "near" proton and core have the relative energy appropriate for the ^{15}F ground-state resonance. Thus we conclude that the expansion stage (iii)-(iv) is initiated, for this WF component, by the interference with WF components associated with the sequential decay path [dashed (blue) arrows].

The angular distributions of the $\mathbf{X}$ and $\mathbf{Y}$ vectors is integrated for presentation of Fig. 5.7. The analysis of the WF for the "pink trajectory" region indicates that this angular distribution is quite broad with a mean angle between $\mathbf{X}$ and $\mathbf{Y}$ close to $\pi/2$. The average case of the solid (pink) path from Fig. 5.7 is visualized in Fig. 5.8. In the three-body decay plane ($r_z = 0$), the initial trajectories of protons are directed along the r_x and r_y axes. The

line $r_x = r_y$ corresponds to the trajectory of the center of mass of the p-p subsystem. It can be seen that at distances of about 30 fm, the radial propagation of one of the protons is practically stopped and the protons behave for some time as connected with a kind of "tether" of (practically) fixed length (blue dotted lines in Fig. 5.8) producing complicated spatial trajectories. The realistic motion in our quantum-mechanical calculations does not of course correspond to this piecewise trajectory; quantum mechanical motion is always "smooth" and there are no well defined decay paths as in the classical case. However, this idealized decay path is quite instructive and demonstrates the complexity of this decay that we portray in qualitative terms as a "tethered decay mechanism".

5.7 Previous Experimental Studies

In 1978 KeKelis *et al.* [17] reported the detection of the first excited state of ^{16}Ne from the observation of a peak with yield of ~ 12 counts at $E_T = 3.03(7)$ MeV in the ^{20}Ne(^{4}He,^{8}He) reaction.

More recently, information on the lowest ^{16}Ne excitations was obtained in two studies [43, 44] which also used neutron knockout from ^{17}Ne beams, but at relativistic energies. See Table 5.2 for a comparison of extracted centroids and widths for the ground and first-excited states in these and the present experiment.

The work of [43] uses a technique based on the tracking of the reaction products, a technique created for studies of the radioactive decay lifetimes in the fs-ns range. In the case of the much shorter-lived ^{16}Ne states, the lifetime information is not extractable. The spectroscopic properties are obtained from kinematically incomplete information. Therefore the resonance parameters are recovered by MC simulations based on theoretical assumptions about spectrum populations and decay mechanisms, both of which have uncertainties. The ^{16}Ne g.s. position $E_T(0^+) = 1.35(8)$ MeV found in [43] has a value that is somewhat lower than ours, but otherwise the results are consistent.

The ^{16}Ne excitation spectrum measured in Refs. [44, 66] is very similar to ours. This is evidence for a similar reaction mechanism despite the large differences in bombarding energies: $E/A = 500$ MeV compared to $E/A = 57.6$ MeV in our work. The experimental resolution and statistical uncertainty in Refs. [44, 66] are significantly worse than in our work [5], the former can be gauged by the widths of the experimental peaks that are almost a factor of two larger than those in Figure 5.2. Despite these differences, it is surprising that the uncertainties on the extracted widths from Refs. [44, 66] are smaller than ours. Such an extraction would require an extremely precise understanding of their experimental resolution. The 2^+ decay energy E_T in Refs. [44, 66] is consistent within the listed experimental errors to our value, but the extracted width in these references ($\Gamma < 50$ keV) is inconsistent with the present work.

Correlation data for the 2^+ state in the relativistic study were also presented in Ref. [66] and it was concluded that they are consistent with a purely sequential calculation. No two-dimensional correlation plots are shown in Ref. [66], however, projections on the energy and angular axes are presented (see Fig. 8 of [66]). Their energy distribution in the "Y" system does not have the doubled-humped structure present in the distribution of Fig. 5.5(a). However, if we take our best-fit simplified-model calculation or the three-body model result and artificially decrease the experimental resolution in our MC simulations so as to reproduce the experimental width of the 2^+ state in the relativistic study, then this feature is washed out and one is left with a broad peak similar to that found in Ref. [66].

The energy distribution in the "T" system obtained from the study of Ref. [66] is consistent with their flat sequential calculation within their large statistical error bars. However, it is also clear that a dependence with enhanced correlations in the diproton region of similar magnitude to that found in our distribution (see Fig. 5.5(b)) would also be consistent. Therefore, the two sets of experimental data may not be inconsistent, however more precise comparisons would require a detailed knowledge of the experimental acceptance of Ref. [66]. It seems that the higher resolution and statistics of the our work have permitted us to bet-

ter characterize the decay mechanism and allow the non-sequential aspects of the decay to become clearer.

5.8 Higher Excited States

In Ref. [5] we also reported on the a second excited state in the ^{14}O+p+p channel at E_T = 7.60(4) MeV. This peak was relatively weak in our excitation spectrum (due to its lower detection efficiency) so no further analysis was attempted. Even higher ^{16}Ne excited states were observed in Ref. [43] by their feeding into the states of ^{15}F. However, it was not possible to resolve such states in this experiment.

At these higher excitation energies the decay will also start populating the ^{13}N+p+p+p exit channel (corresponding energy above its threshold is denoted as E'_T, see Fig. 5.1). The decay-energy spectrum for this channel is shown in Fig. 5.9 and displays two peaks at E'_T = 5.21(10) and 7.60(20) MeV corresponding to ^{16}Ne excitation energies of E^* = 8.37(10) and 10.76(20) MeV, respectively. The solid curve shows the best fit for one choice of the background contribution (dashed curve). As for the ^{14}O+p+p channel, the fit assumes intrinsic Breit-Wigner line shapes where the effect of the experimental resolution is incorporated via the Monte Carlo simulations. The background is relatively large and other functional forms can give good fits as well. We have included contributions to the uncertainties of the peak energies based on fits with other background choices. The fitted intrinsic widths of

Table 5.2: The properties of 0^+ g.s. and first 2^+ states of ^{16}Ne obtained in the recent neutron knockout reaction studies with ^{17}Ne beam. Energies and widths are in MeV. All the E_T values are provided relative to the ^{14}O+p+p threshold.

Work	[43]		[44]		[5], this work	
J^π	E_T	Γ	E_T	Γ	E_T	Γ
0^+	1.35(8)		1.388(15)	0.082(15)	1.466(20)	< 0.08
2^+	3.2(2)	0.2(2)	3.220(46)	< 0.05	3.160(20)	0.150(50)
(2^+)	7.6(2)	$0.8^{+0.8}_{-0.4}$	7.57(6)	≤ 0.1	7.60(4)	≤ 0.5
(?)					9.84(10)	0.32(10)
(?)					12.23(20)	0.51(23)

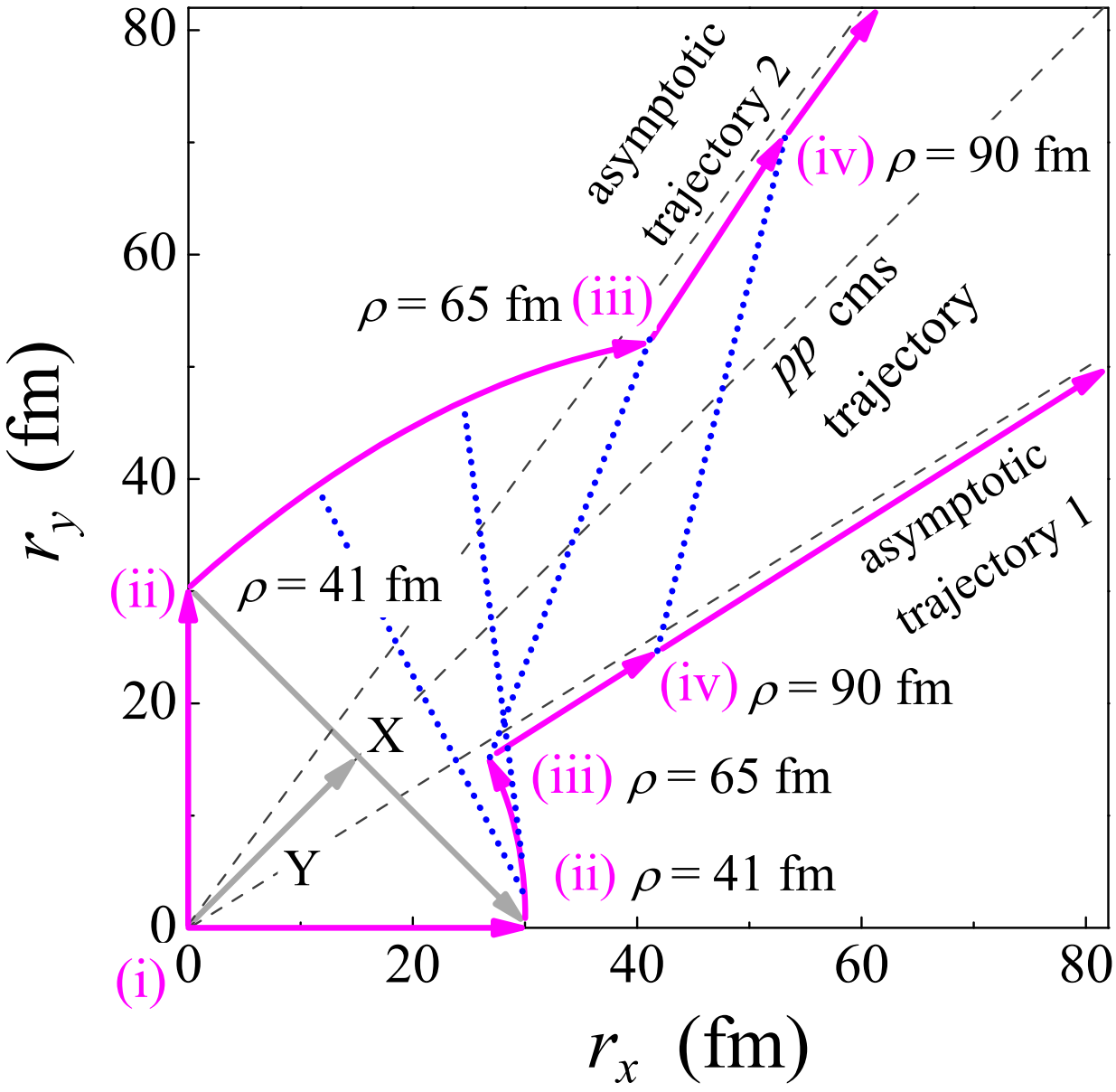

Figure 5.8: Schematic of the tethered decay mechanism. Trajectory of two protons corresponding to solid (pink) path in Fig. 5.7. The configurations labeled by the Roman numerals correspond to the same configurations denoted in Fig. 5.7. The p-p center-of-mass motion path $r_x = r_y$ is collinear with $\mathbf{Y}$ vector for the Jacobi "T" coordinate system.

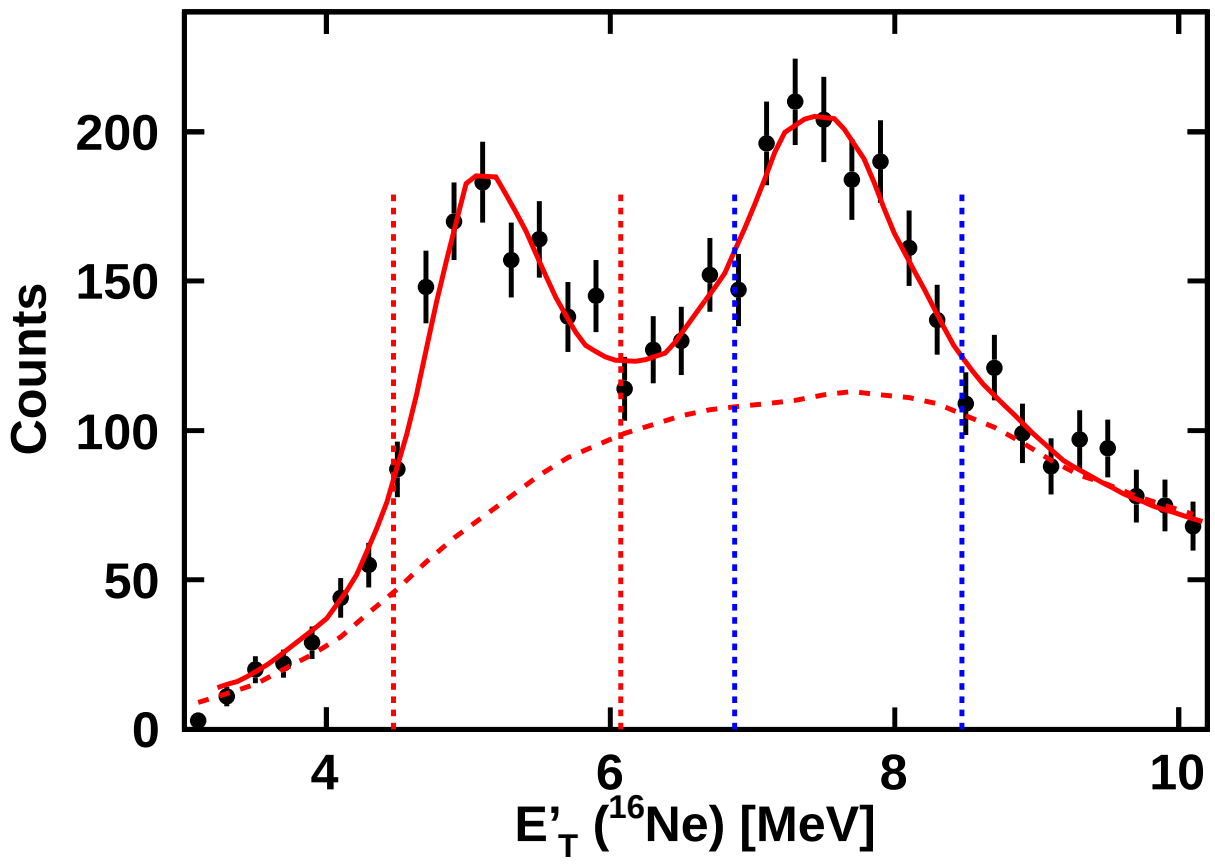

Figure 5.9: Distribution of ^{16}Ne decay energy determined from detected ^{13}N+p+p+p events. Gates are shown on the two observed peaks which are used in the analysis shown in Figure 5.10.

these peaks were found be $\Gamma = 320(100)$ keV and 510(230), respectively.

With three protons in the exit channel, it is much more difficult to determine the decay mechanism compared to channels with just two protons, especially given the relative large background contribution. However some information on the decay path can be established. Figure 5.10 shows the ^{14}O excitation reconstructed from the core and one of the detected protons for each of the two peaks in Fig. 5.9 using the gates shown by the dashed vertical lines. The location of the first five excited states in ^{14}O are shown by the vertical dashed lines in this figure. In interpreting these spectra, one must remember that more than half of the events come from background below the peaks. Also as only one of the three detected

protons can come from the decay of an excited ^{14}O intermediate state, then at least 2/3 of the remaining yield in these spectra is an additional background. Although we cannot rule out small contribution from each of these ^{14}O states in Fig. 5.10, a peak associated with the forth excited state at $E^* = 6.59$ ($J^\pi = 2^+$) is quite prominent for both ^{16}Ne gates. Of course it is not entirely clear whether this ^{14}O level is associated with the background or the peaks in the ^{16}Ne spectrum. However, we note that gating on this $J^\pi = 2^+$ ^{14}O peak, strongly enhances the $E'_T = 5.21$ MeV ^{16}Ne peak and thus we feel confident that this 2^+ level is an important intermediate state in the decay of this level. A similar search for possible ^{15}F intermediate states was fruitless probably because such states are expected to be wide at the available ^{15}F excitation energies in these decays.

5.9 Summary

The decay of the first excited state of ^{16}Ne has been studied. A peak located at decay energy $E_T = 3.16$ MeV was observed in the ^{14}O+p+p invariant mass spectrum which is consistent with the expected location of the 2^+_1 first excited state based on the better known spectroscopy of the mirror nucleus ^{16}C. The intrinsic width of this state was determined to be between 100 and 250 keV.

Three-body calculations which reproduced the momentum correlations of the ^{14}O+p+p decay products of the ground state and were consistent with the experimental limits for its intrinsic width were found to predict an intrinsic width for the 2^+_1 state of $\Gamma \sim 56$ keV which is smaller than the experimental range. This conflict suggests either some deficiency in the calculations or the possibility that the observed peak has other contributions, for example, from the second 0^+_2, state.

We have provided a detailed analysis of the dynamics of the three-body decay model that has met with considerable success in reproducing many features of our and other group's data. The predicted ^{16}Ne$^{2^+}$ 2p decay mechanism differs drastically from the common ideas

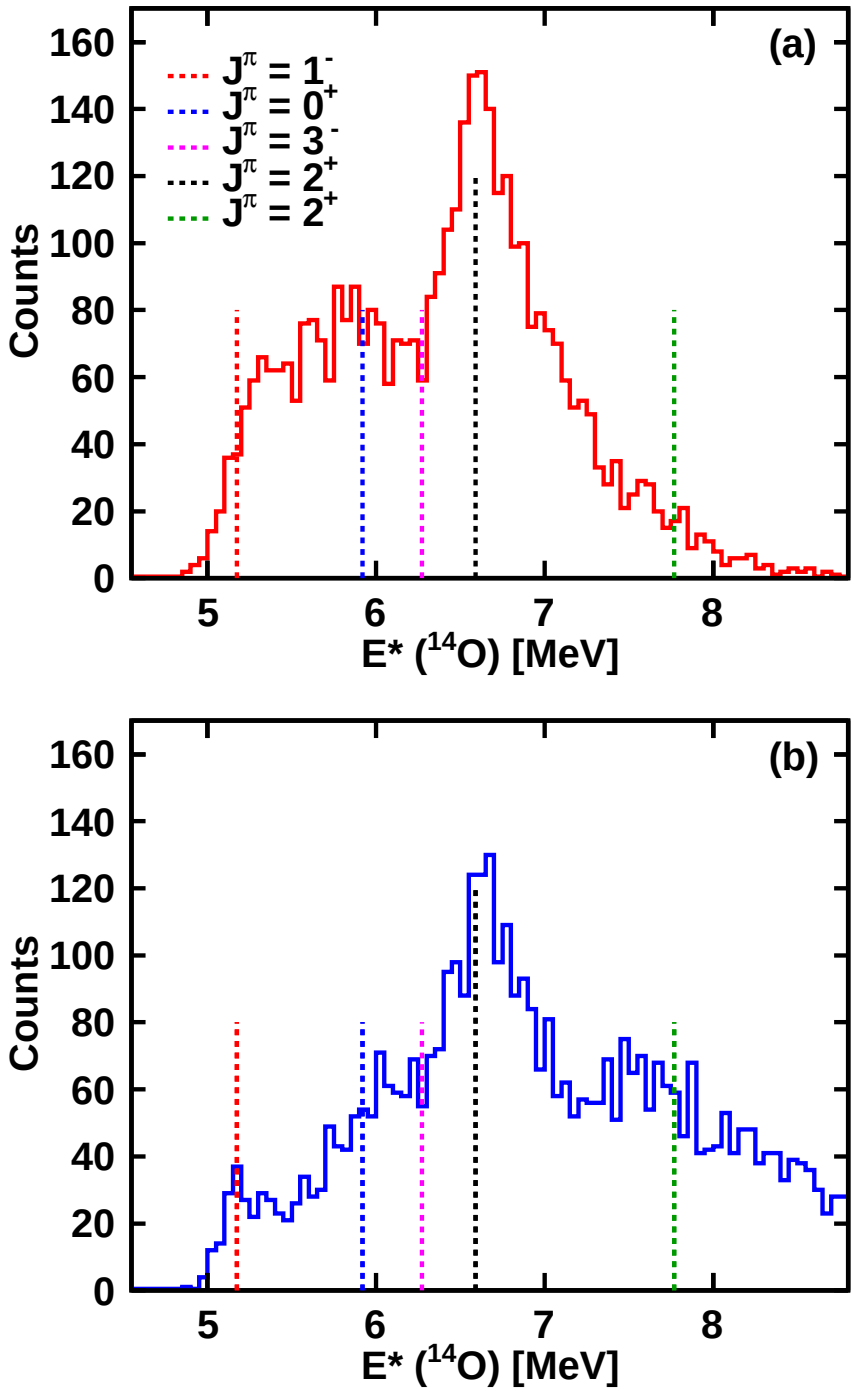

Figure 5.10: Distribution of ^{14}O decay energy determined for all possible ^{13}N+p subsets of each detected ^{13}N+p+p+p event. Pannel (a) is for the gate on the $E'_T = 5.21$ MeV state in ^{16}Ne while (b) is for the $E'_T = 7.60$ MeV state. The vertical dashed lines show the location of the first five excited states in ^{14}O.

about the decay process in terms of sequential or/and diproton decay mechanisms. The two-dimensional correlations measured for the $2p$ decay of the first excited state shows a double-ridge pattern expected for sequential decay only when the two protons have low relative energy (diproton-like correlation). A careful investigation of the decay mechanism on the level of the wavefunction in the three-body model indicates that the real situation is quite intriguing. The model predicts both sequential and prompt-decay paths which interfere and produce the strange decay pattern which we qualitatively describe as a "tethered decay mechanism". The observed correlation pattern is qualitatively similar to that measured previously for excited ^{6}Be fragments and suggests other examples will be found in the future.

Finally, new ^{16}Ne excited states with total decay energy of $E'_T = 5.21(10)$ and 7.60(20) MeV [corresponding $E^* = 8.37(10)$ and 10.76(20) MeV] were observed in the ^{13}N+p+p+p exit channel. There is some evidence that both these peaks have a sequential component in their decay dynamics with intermediate populations of the $E^* = 6.59$ MeV, $J^\pi = 2^+$ resonance in ^{14}O.

Chapter 6

Isobaric Analog State in ^{16}F

6.1 Background

In Chapter 3 evidence for a new type of direct $2p$ decay was presented, namely decay from an Isobaric Analog State (IAS) to an Isobaric Analog State. The daughter nucleus then de-excites to its ground state via γ-ray emission. While $^{8}\mathrm{B}_{IAS}$ was the first case where all of the decay products were measured (two protons, the ^{6}Li core and the γ), it is not the only case where this has been proposed as the decay mechanism. In some previous work by our group a resonance was seen in the $2p$+^{10}B decay channel corresponding to a state in ^{12}N [23]. If the detected ^{10}B were formed in its ground state, then the measured excitation energy would not correspond to any known state in either ^{12}N or its mirror ^{12}B. However, $^{12}\mathrm{N}_{IAS}$ should decay to $^{10}\mathrm{B}_{IAS}$, in an analogous way to the decay of $^{8}\mathrm{B}_{IAS}$. $^{10}\mathrm{B}_{IAS}$ is known to decay via γ emission, however the γ rays were not measured in that experiment. If this measured state were the $^{12}\mathrm{N}_{IAS}$, and it decayed to $^{10}\mathrm{B}_{IAS}$, then the measured excitation energy of ^{12}N is too low by the excitation energy of $^{10}\mathrm{B}_{IAS}$. Adding in this missing energy brings the measured energy up to the predicted excitation energy of $^{12}\mathrm{N}_{IAS}$ from the IMME (see Chapter 7 for more details on the IMME). Thus while this decay mode was not confirmed in this case, the measurement of the decay mode $^{8}\mathrm{B}_{IAS}$ lends strong support to this assumption.

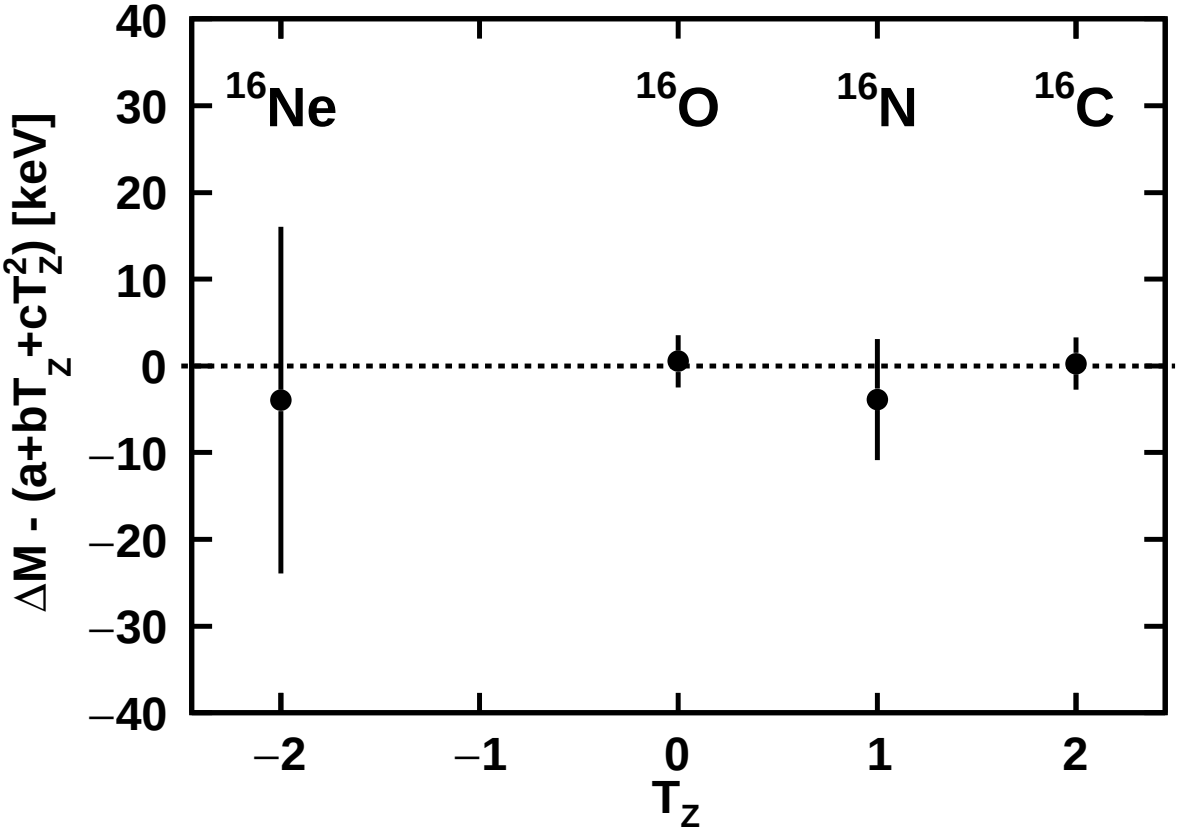

Figure 6.1: Deviation from the fitted quadratic form of the IMME for the lowest $T = 2$ states in the $A = 16$ isobar.

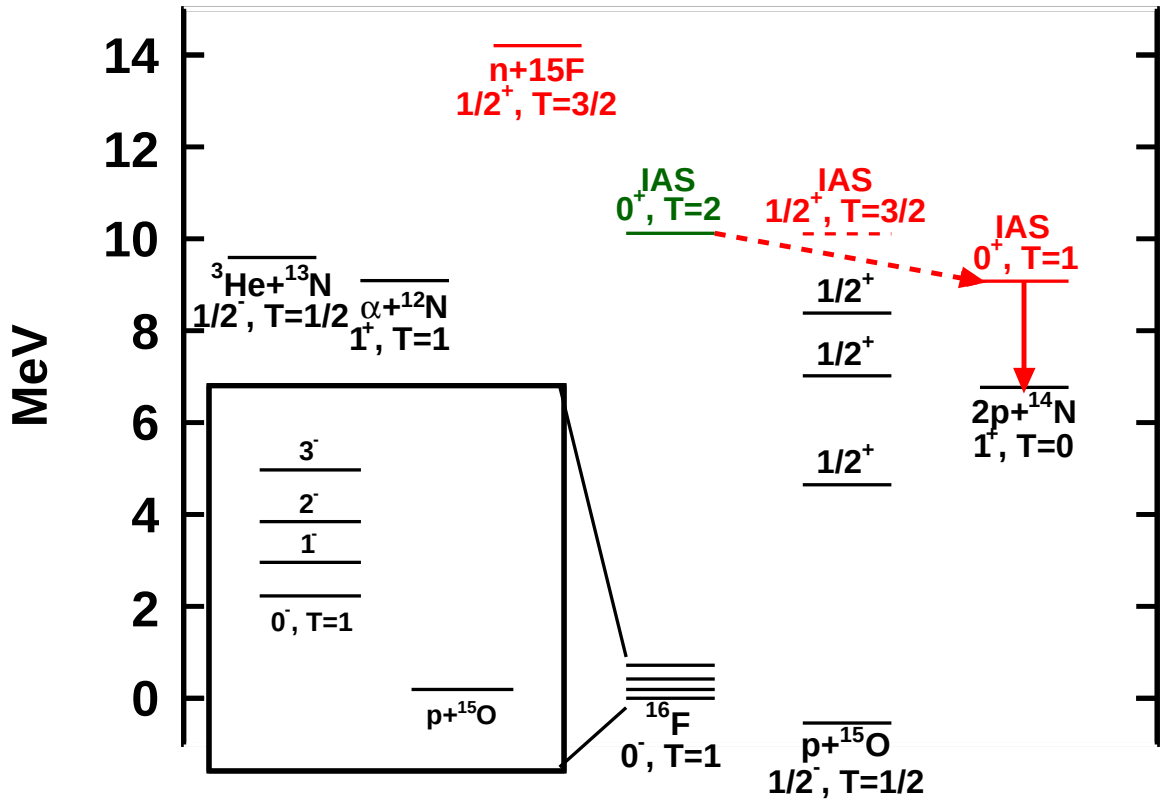

Figure 6.2: Partial level scheme for the decay of $^{16}\mathrm{F}_{IAS}$ (level in green). Colored levels indicate isospin allowed decays from the $^{16}\mathrm{F}_{IAS}$. All energies are relative to the ground state of ^{16}F. The inset shows an expanded level scheme for the low-lying states of ^{16}F.

Moving higher in mass, the next Isobaric Analog State that could decay in this manner is $^{16}\mathrm{F}_{IAS}$. While this resonance has never been observed, the energy can be predicted from the IMME for $A = 16$, Fig. 6.1. The quadratic fit of the $A = 16$, $T = 2$ quintet contains the new mass for $^{16}\mathrm{Ne}_{g.s.}$ from Chapter 4 and takes the other masses from the most recent mass evaluation [67]. This fit predicts an excitation energy for $^{16}\mathrm{F}_{IAS}$ of 10.12 MeV, which is displayed as the green level in the partial level scheme, Fig. 6.2. As was true in both $^{8}\mathrm{B}_{IAS}$ and $^{12}\mathrm{N}_{IAS}$, the only isospin- and energy-allowed particle decay is a $2p$ decay to the isobaric analog state of the daughter, ^{14}N. The $^{14}\mathrm{N}_{IAS}$ is known to decay by emission of a 2.313 MeV γ ray to the ground state. If this $2p$ decay were to be observed in an invariant mass spectrum, the peak would be located at ~ 7.8 MeV.

6.2 Two-proton decay

With a ^{17}Ne beam, ^{16}F states can be formed in proton-knockout reactions. In the same data set obtained to detect ^{16}Ne two-proton decay, two-proton decay of ^{16}F states were investigated. The reconstructed excitation energy spectrum of ^{16}F from all detected $2p$+^{14}N events is shown in Fig. 6.3 (a). If $^{16}\mathrm{F}_{IAS}$ were to decay by the $2p$+$^{14}\mathrm{N}_{IAS}$ path, there should be a peak at the position of the red arrow. An expanded version of this can be seen in the inset to Fig. 6.3 (a). The observed peak is ~ 200 keV lower than the expected position of the IAS. While this does not rule out the possibility that it is the IAS, it is highly unusual for the energy of an analog state to deviate that far from the quadratic form of the IMME. If this were the IAS, it must be in coincidence with the 2.313 MeV γ ray from the decay of $^{14}\mathrm{N}_{IAS}$. The energy spectrum of γ rays in coincidence with events in the region of the observed peak are shown in Fig. 6.3 (b). For a 2.3 MeV γ ray, the photopeak efficiency of CAESAR is $\sim 20\%$, i.e. with roughly 100 events in the peak we should measure 20 events in the photopeak. We can therefore conclude that the observed peak does not decay through the $^{14}\mathrm{N}_{IAS}$ and is a $T = 1$ state at $E^* = 7.67 \pm 0.02$ MeV. This is likely the analog of the

$E^* = 7.674$ MeV state in the mirror, ^{16}N, for which no J^π assignment was made.

As we did not see the $^{16}\mathrm{F}_{IAS}$ in the isospin allowed $2p$ decay channel, we should look for an explanation. We saw isospin allowed $2p$ decay from the isobaric analog states in both ^{8}B and ^{12}N and that channel is also energetically allowed for $^{16}\mathrm{F}_{IAS}$. The decay energies for the IAS to IAS transitions are listed in Table 6.1. As one moves higher in mass the decay energy becomes smaller, and at the same time the Coulomb barrier becomes larger. Both of these effects dramatically reduce the barrier penetration factors, P_ℓ, for these decays. The isospin allowed $2p$ decay for $^{16}\mathrm{F}_{IAS}$ is more than 100 times slower than the isospin allowed $2p$ decay for $^8\mathrm{B}_{IAS}$. This increase in the partial half-life, decrease in partial decay width, allows isospin non-conserving decay channels to be competitive.

Decay channel	E_T (MeV)	ℓ	P_ℓ
$^8\mathrm{B}_{IAS} \rightarrow 2p{+}^6\mathrm{Li}_{IAS}$	1.312	0	0.0907
$^{12}\mathrm{N}_{IAS} \rightarrow 2p{+}^{10}\mathrm{B}_{IAS}$	1.165	0	0.0144
$^{16}\mathrm{F}_{IAS} \rightarrow 2p{+}^{14}\mathrm{N}_{IAS}$	1.046	0	0.000736
$^{16}\mathrm{F}_{IAS} \rightarrow 2p{+}^{14}\mathrm{N}_{g.s.}$	3.359	0	0.289
$^{16}\mathrm{F}_{IAS} \rightarrow \alpha{+}^{12}\mathrm{N}_{g.s.}$	1.037	2	0.000034
$^{16}\mathrm{F}_{IAS} \rightarrow {}^3\mathrm{He}{+}^{13}\mathrm{N}_{g.s.}$	0.523	1	$7.0\mathrm{x}10^{-8}$

Table 6.1: Decay energies (E_T) and barrier penetration factors (P_ℓ) for the decay channels relevant to this work. The barrier penetration factors for $2p$ decays are calculated assuming that each proton takes away 1/2 E_T. Isospin non-conserving decays are listed in the lower section of the table.

6.3 Isospin non-conserving decays

From phase-space considerations, one of the most competitive isospin non-conserving decay mode for $^{16}\mathrm{F}_{IAS}$ is $2p$ emission to the ground state of ^{14}N either directly by simultaneous $2p$ emission or sequentially through an excited state of ^{15}O. If the energy predicted from the IMME is correct, then either possibility would produce a peak at the location of the black arrow, Fig. 6.3 (a). While there is a peak near that energy in the $2p{+}^{14}$N invariant mass spectrum, the excitation energy is $E^* = 10.26 \pm 0.02$ MeV, which is more than 100 keV

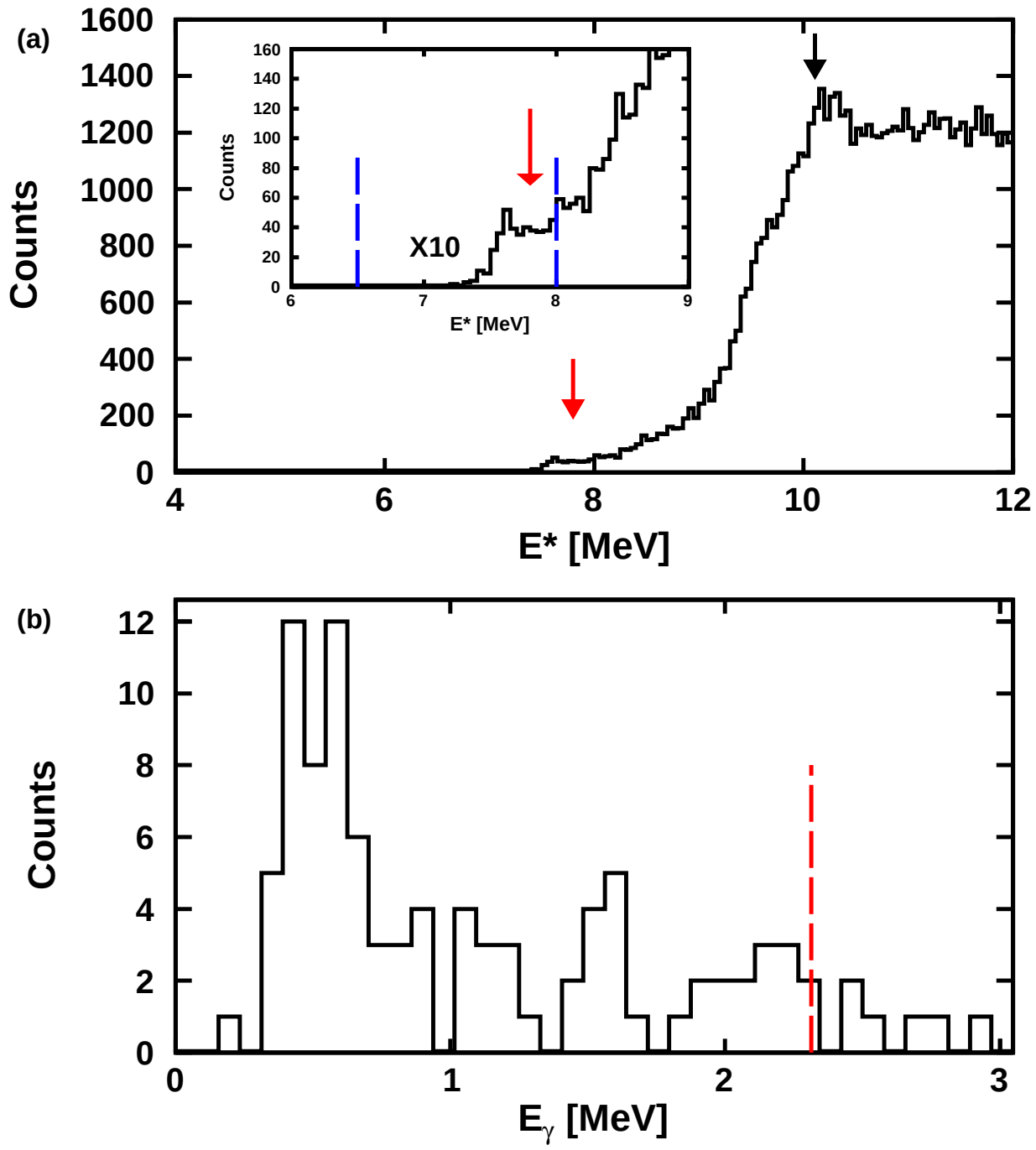

Figure 6.3: (a) Excitation energy spectrum of ^{16}F from all detected $2p$+^{14}N events. The inset is shows the same histogram expanded in the region around the expected $^{16}F_{IAS}$ peak. (b) γ ray energy spectrum measured in coincidence with events inside of the gate indicated in (a) with the blue dashed lines. The excepted photopeak position (2.313 MeV) is marked with the red dashed line.

different than the predicted energy. This is also larger than any known deviation from the quadratic IMME for an isospin multiplet. Therefore, without further evidence that this is a $T = 2$ state, we must conclude that it is probably a previously unknown $T = 1$ state.

Other possible energy-allowed but isospin-forbidden transitions are alpha emission and ^{3}He emission. Both decays have decay energies at or below 1 MeV and have angular momentum barriers. The barrier penetration factors are much lower than even the isospin allowed $2p$ decay channel, so we do not expect to see any yield to these channels. Figure 6.4 shows the excitation energy spectra for ^{16}F decay to α (a) and ^{3}He (b). No peak is observed near 10.12 MeV in either spectrum, indicating that $^{16}\mathrm{F}_{IAS}$ does not decay through either of these channels.

The final possibility for isospin non-conserving decay is via $1p$ emission. The $^{16}\mathrm{F}_{IAS}$ has $J^\pi = 0^+$, so it will preferentially decay to $1/2^+$ states. All energy allowed $1/2^+$ states in ^{15}O are shown in Fig. 6.2. The $1/2^+$ isobaric analog state in ^{15}O (in red) is energy forbidden. The next two highest $1/2^+$ states will decay to $^{14}\mathrm{N}_{g.s.}$ which was previously ruled out. The last $1/2^+$ state, the first-excited state, is known to decay via a 5.183 MeV γ ray. The excitation energy spectrum from all p+^{15}O events is shown in Fig. 6.5. If $^{16}\mathrm{F}_{IAS}$ decayed through the first-excited state in ^{15}O, this would be detected as a peak at $\sim$ 4.9 MeV in the invariant-mass spectrum [$E^*(^{16}F_{IAS})$ - E_γ], and no peak is observed. While $1p$ decay to the ground state is $\ell = 1$, the decay energy is 10.655 MeV so the barrier penetration factor is large. While no peak is observed at 10.12 MeV, we cannot rule out this possibility as our detection efficiency is very small in this region.

6.4 Gamma decay

The only other energy-allowed, isospin-conserving decay mode for $^{16}\mathrm{F}_{IAS}$ is γ decay to a low lying state in ^{16}F which will then $1p$ decay to $^{15}\mathrm{O}_{g.s.}$. The low-lying structure of ^{16}F can be seen in the inset of Fig. 6.2. While γ decay is not normally competitive with proton decay,

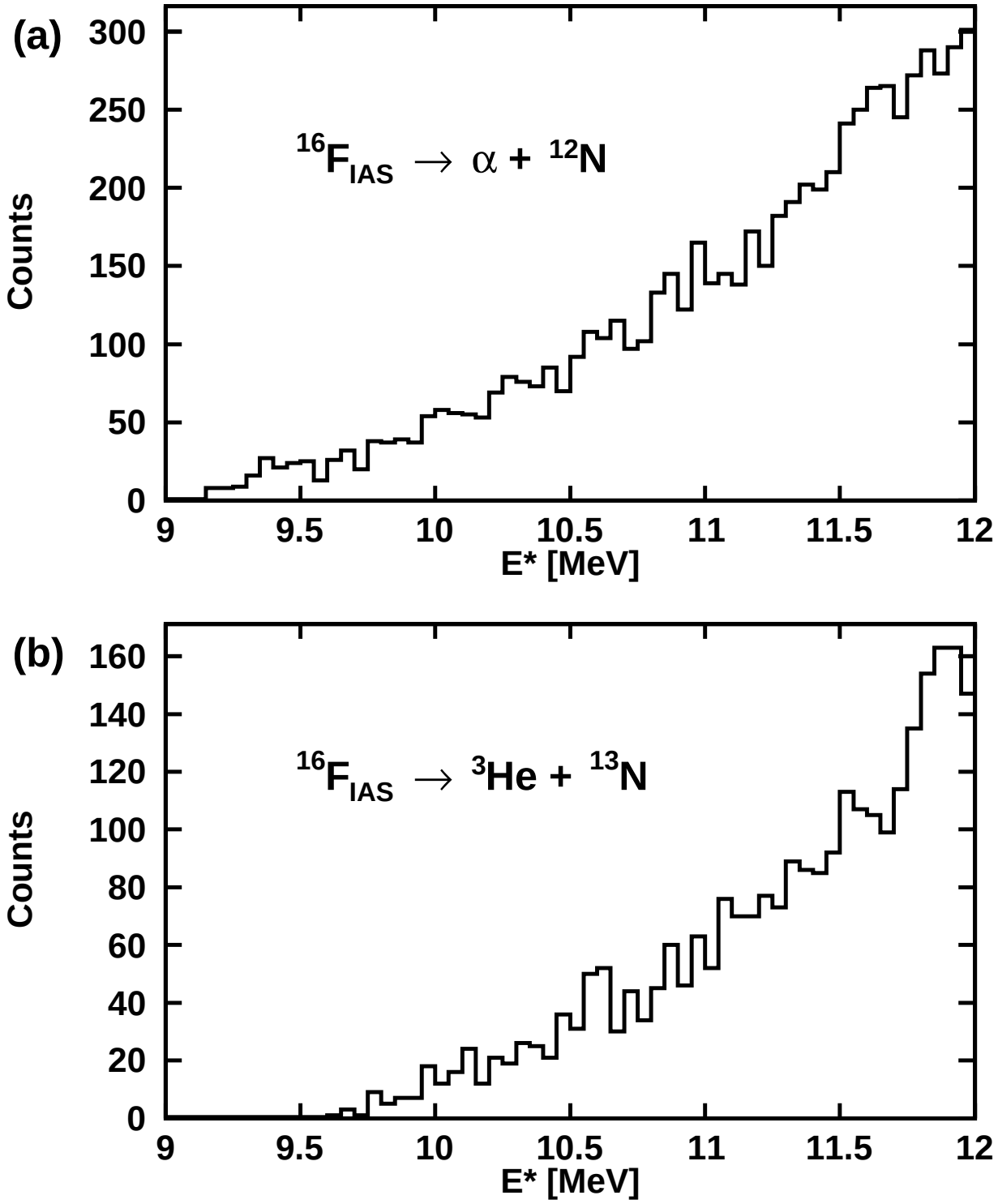

Figure 6.4: Excitation energy spectra for all detected (a) α+^{12}N events and (b) ^{3}He+^{13}N events.

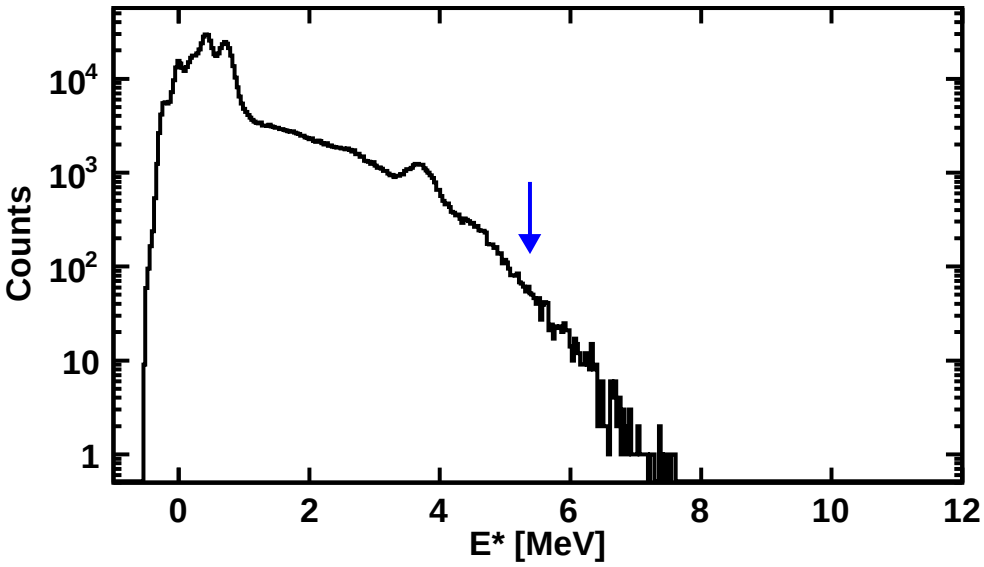

Figure 6.5: Excitation energy spectra for all detected p+^{15}O events. The blue arrow indicated the energy of the $T = 1$ state from the blue path, see text, if the γ-ray energy were added.

for this $\sim$ 10 MeV $E1$ transition ($0^+ \rightarrow 1^-$) the estimated [Weiskopf] γ decay lifetime is 2×10^{-18} s. As we do not see the isospin allowed $2p$ decay, the only energy-allowed particle decays are isospin forbidden. This may make the particle decay lifetime long enough to be comparable to that expected for this γ decay.

For a 10 MeV γ ray in CsI(Na), the attenuation coefficient (related to the interaction probability) for pair production is more than a factor of three larger than Compton scattering, with photoelectric effect many orders of magnitude less than both. In pair production, the γ ray spontaneously creates a positron-electron pair that deposit all but 1.022 MeV of the energy of the γ ray in the first crystal. That 1.022 MeV is released as two 511 keV γ rays when the positron annihilates with an electron in the crystal. Those γ rays can be detected in neighboring crystals and added to the energy measured in the first. Similarly, γ rays which Compton scatter in the first crystal will deposit most of their energy in that crystal. The remaining energy can be detected if the scattered γ is detected in a neighboring crystal. Aside from small-angle Compton scattering, in both of these cases these γ rays will over-range our ADCs.

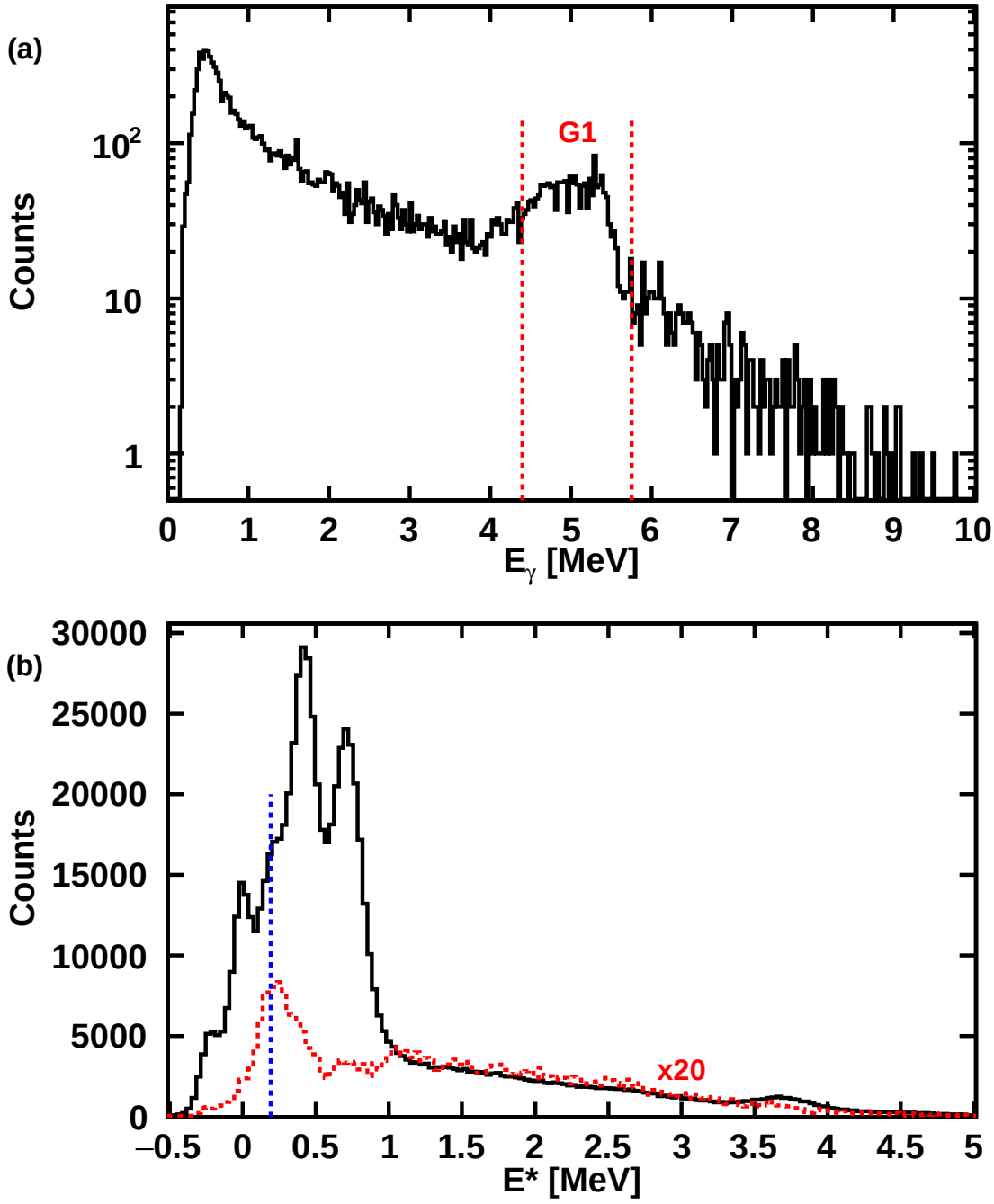

Figure 6.6: (a) γ energy spectrum in coincidence with all p+^{15}O events. (b) ^{16}F excitation energy spectrum of p+^{15}O events. This is the same spectrum shown in Fig. 6.5 but with a linear ordinate. The blue dashed line marks the position of the first-excited state in ^{16}F. The red dashed histogram is the excitation energy spectrum gated on the *gamma* rays in gate G1.

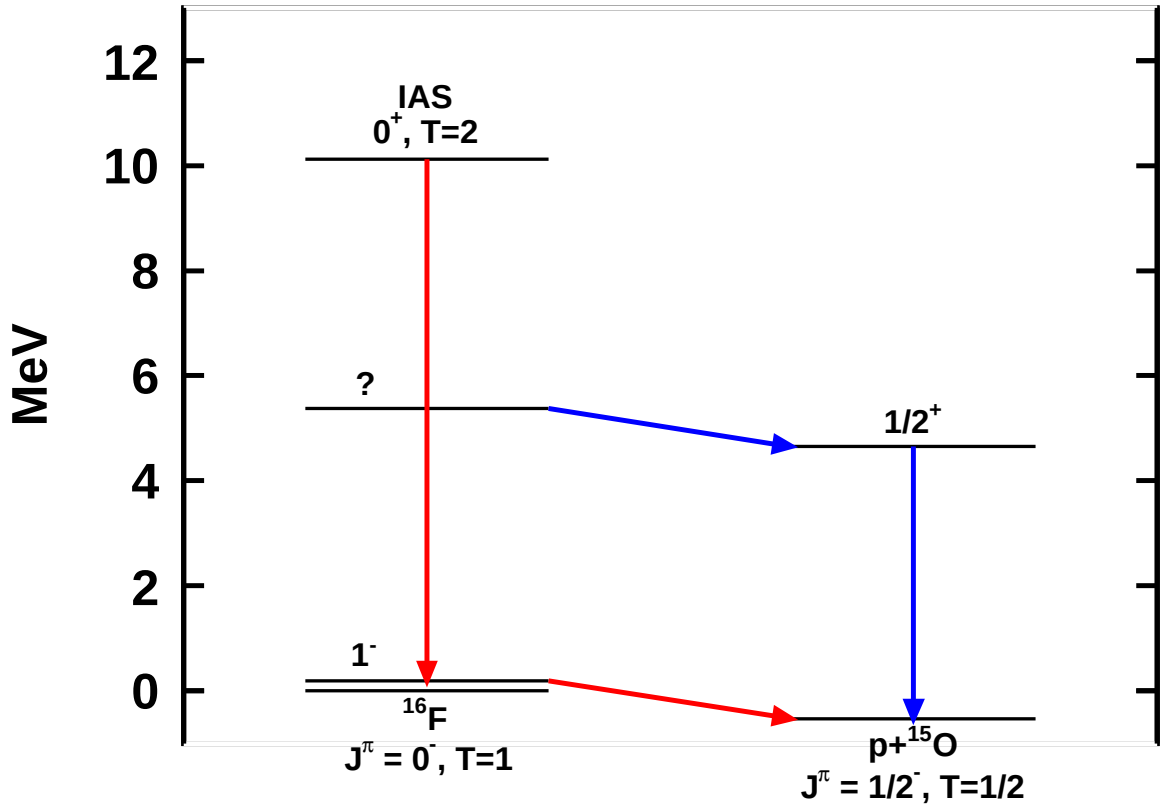

Figure 6.7: Partial level scheme of ^{16}F . The red arrows indicate a possible isospin-conserving decay mode for the decay of $^{16}\mathrm{F}_{IAS}$, and the blue mode indicates the possible decay mode of a $T = 1$ state of ^{16}F.

The γ-ray energy spectrum measured in coincidence with all detected p+^{15}O events is shown in Fig. 6.6 (a). While we would expect a smoothly falling distribution that cuts off around 8.5 MeV, the maximum energy that does not over range our detectors, we see a wide peak centered at $\sim$ 5 MeV. Gating the p+^{15}O excitation energy spectrum on this peak pulls out predominantly a single peak, Fig. 6.6 (b). Two possible explanations for this particle-gamma coincidence are summarized in Fig. 6.7. If the γ decay preceded the particle decay, the invariant-mass peak corresponds to the 0.193 MeV first-excited 1^- state in ^{16}F (red path). If the $^{16}\mathrm{F}_{IAS}$ were to γ decay, it would preferentially decay to this first-excited state. However, there is no obvious reason for a 10 MeV γ ray to form a peak at $\sim$ 5 MeV. Another possibility is that the particle decay precedes the γ decay (blue path). If that were the case, then the particle decay is to the first-excited state of ^{15}O, which γ decays via a 5.183 MeV γ. Then this particle + γ decay would correspond to the decay of a state at $\sim$ 5.4 MeV in ^{16}F that is $T = 1$. The position of this low T state is marked by a blue arrow in Fig. 6.5. While the blue decay scheme is possible, there would need to be a nuclear structure reason for that state to decay to the excited state of ^{15}O, giving up a large amount of phase space, rather than decaying directly to the ground state.

6.5 Summary

We have measured the excitation energy and decay mode of two new, $T = 1$ excited states in ^{16}F that decay by $2p$ emission. They have excitation energies of $E^* = 7.67 \pm 0.02$ MeV and $E^* = 10.26 \pm 0.02$ MeV. While we expected the $^{16}\mathrm{F}_{IAS}$ to decay by $2p$ decay to $^{14}\mathrm{N}_{IAS}$, this is highly suppressed by the Coulomb barrier and was not observed. This is likely due to the reduced phase space and increased Coulomb barrier as compared to the observed cases. The only possible evidence for $^{16}\mathrm{F}_{IAS}$ is a peak in the γ ray energy spectrum measured in coincidence with a $E_T \sim 0.2$ MeV $1p$ decay. As the main goal of the γ ray array was to detect the 3.563 MeV γ ray from the decay of $^{6}\mathrm{Li}_{IAS}$, our electronics were not set up to

measure a 10 MeV γ ray. Simulation of the detector response to a 10 MeV γ ray is not possible without detailed knowledge of these electronics, and therefore no clear conclusion can be drawn for the γ decay of $^{16}\mathrm{F}_{IAS}$.

Chapter 7

A = 7 IMME

7.1 Background

In the absence of Coulomb forces, if isospin is a good quantum number, the masses of the members of an isobaric multiplet should be independent of their isospin projections, T_Z. With the addition of the Coulomb force and the proton-neutron mass difference, the masses can be described by the quadratic Isobaric Multiplet Mass Equation (IMME),

$$M(T, T_Z) = a + bT_Z + cT_Z^2. \tag{7.1}$$

Addition of cubic (dT_Z^3) or quartic (eT_Z^4) terms to the IMME measure deviation from the quadratic form due to isospin-symmetry breaking. However, certain isospin-breaking effects, such as Thomas-Ehrman shifts and isospin mixing, are entirely accounted for in the b and c terms [68]. The cubic and quartic terms are generally small and in most cases unnecessary for quartets and quintets with $A \leq 41$ [69]. Among these, only the $A = 7$, $A = 11$, and $A = 41$ quartets have cubic terms larger than 20 keV [69]. For the $A = 7$, $T = 3/2$ quartet a purely quadratic fit has $\chi^2/n = 4.7$, and $d = 47 \pm 22$ keV was required to fit the quartet [24]. While this value of d is not that large, the deviation from zero is at the 2σ level. The A=7 quartet is unique amongst multiplets used to test the IMME in that all of it members

are resonances. Indeed the narrowest of these resonances is $^{7}\mathrm{He}_{g.s.}$ with a FWHM of 150 (20) keV [9]. All members are wide enough, and close enough to threshold, that their line shapes are not adequately described by a Breit-Wigner form. In such cases the resonance energy is not a well defined quantity, and there are a number of different definitions that can be employed which can give different values. It is therefore important to use a consistent definition of the resonance energy for all four members in constructing the IMME.

The A=7 quartet is also important as it is amenable to *ab initio* calculations. Green's Function Monte Carlo (GFMC) calculations suggest that this quartet requires a cubic term of moderate strength, i.e. d=7.5±2.5 keV [10].

Here we reexamine the A=7 IMME and present new data for the isobaric analog states (IAS) in both ^{7}Li and ^{7}Be. In addition we refit existing data for $^{7}\mathrm{B}_{g.s.}$ decay published in Ref. [24] and subject all three states to a consistent R-matrix analysis [70] of their line shapes. The line shape of the forth member of the quartet, $^{7}\mathrm{He}_{g.s.}$, will be taken from the R-matrix analyses of its n+^{6}He decay channel in Refs. [7, 8]. Note that for all four members of the quartet, the R-matrix analysis was made with data obtained using the invariant-mass technique. The fact that all members are resonances also allows us to use the R-matrix analysis to extract information on the variation of spectroscopic strength across the multiplet.

Previous measurements of the $|T_Z| = 1/2$ members ($^{7}\mathrm{Be}_{IAS}$ and $^{7}\mathrm{Li}_{IAS}$) of this quartet were made more than 45 years ago. For $^{7}\mathrm{Li}_{IAS}$ there are two previous measurements, E* = 11.19 ± 0.05 MeV from ^{6}Li(n,n') [71] and E* = 11.28 ± 0.04 MeV from ^{9}Be(p,^{3}He) [72, 73]. For $^{7}\mathrm{Be}_{IAS}$ there exist two measurements, E* = 11.00 ± 0.05 MeV from ^{4}He(^{3}He,p) [74] and E* = 11.01 ± 0.04 MeV from ^{9}Be(p,t) [73, 75]. In all these previous studies, the experimental peaks were fit using Breit-Wigner lines shapes, rather than the R-matrix form, possibly causing problems for the A=7 IMME studies.

7.2 Experimental Method

Data for the decay of $^{7}\mathrm{Be}_{IAS}$ were obtained using the experiment described in Chapter 2. Data for $^{7}\mathrm{B}_{g.s.}$ were obtained under almost identical experimental conditions (same beam, target and detector arrangement) and the invariant mass spectrum was presented in Ref. [24]. $^{7}\mathrm{Li}_{IAS}$ states were populated by reactions of a secondary beam of ^{12}Be (1 x 10^5 pps, 87% purity) on polyethylene and carbon targets. The decay products were detected in the High-Resolution Array (HiRA) [19] in 16 ΔE-E [Si-CsI(Tl)] telescopes located 60 cm downstream of the target. The telescopes were arranged in four towers of four telescopes each, with two towers on either side of the beam.

7.3 R-matrix formalism

The line shapes of the resonances were fit with the R-matrix formalism [70] which was originally developed to describe resonance scattering. In this formalism, the scattering wave for a particular channel c is subdivided into internal and external regions separated by a surface at relative distance $r = a_c$, called the channel radius. The channel radius is chosen such that only Coulomb and centrifugal potentials exits in the external region and therefore the reduced radial wavefunction $u_c(r)$ for that channel can be expressed as a linear combination of regular and irregular Coulomb wave functions. In the isolated resonance approximation [70], the couplings between the wavefunctions $u_c(r)$ and their derivatives $u'_c(r)$ of the different channels in the vicinity of the energy E_λ are given by

$$u_c(a_c) = \sum_{c'} \frac{\gamma_c \gamma_{c'}}{E_\lambda - E} \left[a_{c'} u'_{c'}(a_{c'}) - B_{c'} u_{c'}(a_{c'}) \right] \tag{7.2}$$

where the boundary conditions B_c are the logarithmic derivative of the channel wavefunction $\frac{a_c u_c'(a_c)}{u_c(a_c)}$ at the energy E_λ. For a resonance that couples to only one channel, this reduces to

$$\frac{a_c u_c'(a_c)}{u_c(a_c)} = B_c + \frac{E_\lambda - E}{\gamma_c^2}, \tag{7.3}$$

which is just a first-order expansion of the logarithmic derivative in energy about E_λ. From Eq. (7.2), the S-matrix relating the magnitudes of the incoming and outgoing waves for the different channels can be derived. For elastic scattering with a channel c, the S-matrix element can be expressed as

$$\mathcal{S}_{c,c} = \mathcal{S}_{c,c}^{res} e^{(-2i\phi_c)} \tag{7.4}$$

where the ϕ_c term is the contribution from hard-core or potential scattering and $\mathcal{S}_{c,c}^{res}$ is the resonance contribution. Similarly the total phase shift δ_c, defined by $\mathcal{S}_c = |\mathcal{S}_{c,c}|e^{2i\delta_c}$, has both a resonant and hard-core contribution, i.e.,

$$\delta_c = \delta_c^{res} - \phi_c. \tag{7.5}$$

In invariant-mass studies where the resonance is produced by knockout or other inelastic processes, the potential scattering contribution is irrelevant and so the line shape is assumed to come just from the resonant contribution, i.e.,

$$\left|1 - \mathcal{S}_{c,c}^{res}(E)\right|^2 = \frac{\Gamma_c(E)}{(E_\lambda + \Delta_{tot}(E) - E)^2 + (\Gamma_{tot}(E)/2)^2} \tag{7.6}$$

where the energy-dependent total decay width has contributions from all unbound channels that couple to the level

$$\Gamma_{tot} = \sum_c^{(unbound)} \Gamma_c(E) \tag{7.7}$$

and the total level shift has contributions from all bound and unbound channels

$$\Delta_{tot} = \sum_{c}^{(unbound)} \Delta_c(E) + \sum_{c}^{(bound)} \Delta_c(E). \tag{7.8}$$

The level shifts are $\Delta_c(E) = -\gamma_c^2 \left[S_c(E - E_c) - B_c\right]$ where E_c is the threshold for that channel. Given that the isolated level approximation is only valid in the vicinity of the E_λ, this value should in principle be chosen to be in the center of the resonance region. However in practice, equivalent line shapes can be obtained with any value of E_λ as long as the B_c values are adjusted accordingly. However, it is useful to use what has been called natural boundary conditions defined as $B_c = S_c(E_\lambda - E_c)$ so that $\Delta_i(E_\lambda) = 0$ and then E_λ takes the value of the resonance energy (at least in one definition of that quantity [see Sec. 7.4]). The energy-dependent decay widths are $\Gamma_c(E) = 2\gamma_c^2 P_c(E - E_c)$ where P_c is called the penetrability factor. For unbound states ($E > E_c$), both $P(E - E_c)$ and $S(E - E_c)$ are dependent on the regular and irregular Coulomb wavefunction F and G evaluated at the channel radius. For bound states ($E < E_c$), $P(E - E_c) = 0$ and $S(E - E_c)$ is determined from the Whittaker function at this radius. See Ref [70] for details.

The use of Eq. (7.6) is an assumption which should be justified by reaction theory. However given the complexity of the reactions in this work, where multiple particles are removed from the projectiles with possible contribution from different mechanisms, this is not possible at present. In general one would not expect Eq. (7.6) to be valid at low bombarding energies where the range of possible excitations is limited by energy conservation. This should not be a problem in this work. Also in the isolated level approximation, this assumption (Eq.(7.6)) may not be valid too far from the resonance energy.

The reduced widths can be written as

$$\gamma_c^2 = \mathbb{S}_c C_c^2 \gamma_c^2(s.p.) \tag{7.9}$$

where $\gamma_c^2(s.p.)$ is the single-particle value of the reduced width, and $\mathbb{S}_c C_c^2$ is the spectroscopic

factor for that channel. The quantity C_c is the isospin Clebsch-Gordan coefficient and the total spectroscopic strength is $\mathbb{S}_c$ for isobaric equivalent decays. In the single-particle model, the overlap function for the channel c is the solution of the Schroedinger equation for the potential $V(r)$ between the two fragments. If this potential is known and thus $a_c u_c'(a_c)/u_c(a_c)$ can be calculated, then $\gamma_c^2(s.p.)$ can be determined from it's first order expansion about the resonance energy [Eq. (7.3)]. Equivalently the single-particle value is also given by [70]

$$\gamma_c^2(s.p.) = \frac{\hbar^2}{m_c a_c^2}\theta_c^2, \tag{7.10}$$

$$\theta_c^2 = \frac{a_c}{2\int_0^{a_c} u_c(r)^2 dr} u_c(a_c)^2. \tag{7.11}$$

Many R-matrix analyses ignore the contribution from bound channels to Δ_{tot}. If a bound channel c is eliminated and we assume the Thomas approximation that $\Delta_c(E)$ is linear in energy, then the $R-$matrix line shape expression Eq. (7.6) still holds but the remaining partial decay widths for channels c' must be replaced by effective values

$$\gamma_{c'}^2(eff) = \frac{\gamma_{c'}^2}{1 - d\Delta_c/dE}. \tag{7.12}$$

The resonance energy does not change as long as one is using natural boundary conditions. These $\gamma_{c'}^2(eff)$ values can be used to describe the line shape, however they should not be used to extract the spectroscopic factor unless corrections for the eliminated channels are first made. As shown in Ref. [70], for a bound channel:

$$\frac{d\Delta_c}{dE} = -\mathbb{S}_c C_c^2 \frac{\int_{a_c}^{\infty} |u_c(r)|^2 dr}{\int_0^{a_c} |u_c(r)|^2 dr}. \tag{7.13}$$

Therefore the largest correction will be from eliminated channels with large spectroscopic strength and with energies close to threshold where the wavefunction extends significantly beyond the channel radius. In this work the most important correction will come from eliminating the nucleon+core (J^π=2^+) channels where these conditions hold. However, rather

than trying to correct the effective values, we will perform R-matrix fits with these channels included and thus do not rely on the Thomas approximation.

7.4 Resonance energy definitions

There are many definitions of the resonance energy which give different values for wide resonances, but coincide in the limit of the resonance width going to zero [76, 77]. For a single channel, the scattering phase shift undergoes a change of around π radians as the energy is scanned across the resonance. One could consider the resonance energy as the value where this change in phase shift is $\pi/2$ radians. In the R-matrix formalism where the total phase shift is conveniently given in terms of the sum of potential scattering and resonance scattering contributions [Eq. (7.5)], the resonance energy is typically defined as the energy where the resonant part of the phase shift is $\pi/2$ radians, i.e., $\delta^{res}(E_r^{(1)}) = \pi/2$. This occurs at the energy [70]

$$E_r^{(1)} = E_\lambda + \Delta(E_r^{(1)}) \tag{7.14}$$

which for natural boundary conditions is just $E_r^{(1)} = E_\lambda$. Another possible solution is to choose the energy $E_r^{(2)}$ where the total phase shift changes fastest with energy, i.e., $(d^2\delta/dE^2)_{E_r^{(2)}} = 0$.

For levels which couple to more than one open channel, like the decay of $^7\mathrm{Be}_{IAS}$ and $^7\mathrm{Li}_{IAS}$, phase shifts for elastic scattering of the different channels do not always undergo a change of π radians as one scans the resonance and thus these definitions need to be generalized. If there are two open channels, then only for the channel with the larger partial decay width does this phase shift change by π radians. For example, Fig. 7.1 shows the total neutron and proton phase shifts extracted from our R-matrix analysis of the $^7\mathrm{Li}_{IAS}$ resonance (see later). Here only the dominant proton channel undergoes a phase shift of close to π radians whereas the neutron channels has little net change in the phase across the resonance. However, for both channels, $\mathcal{S}_{c,c}^{res}$ is purely real at the energy $E_r^{(1)}$ given by

Eq. (7.14) and thus this can be used as a more general definition of this resonance energy.

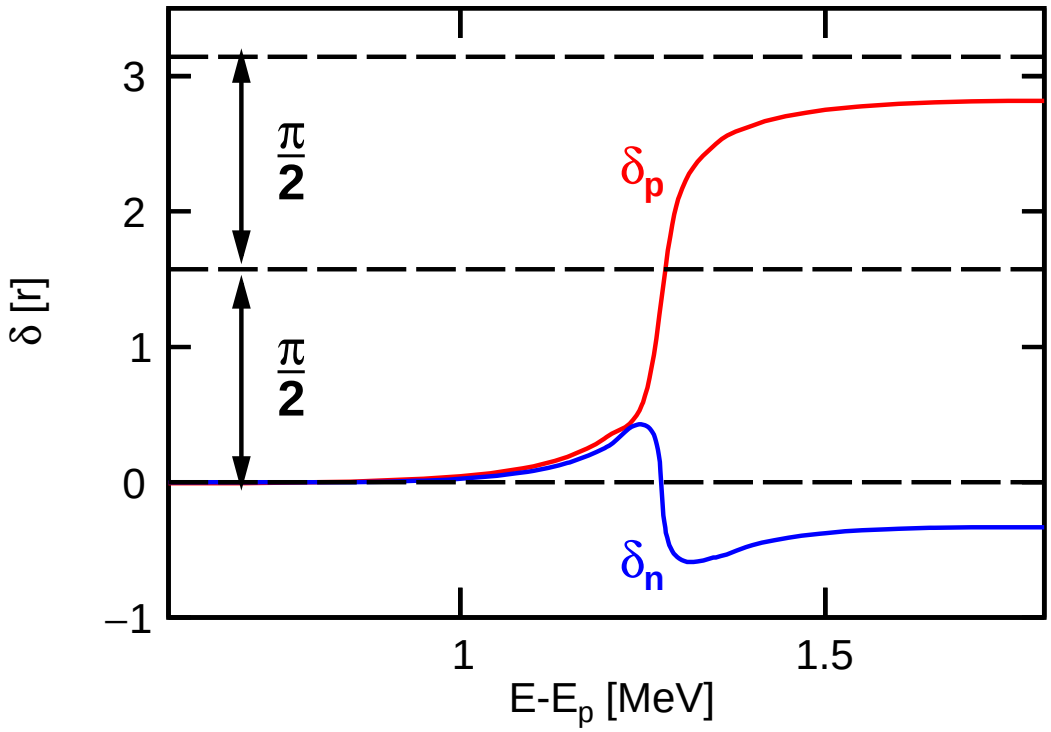

Figure 7.1: (Color Online) Elastic scattering phase shifts for p+^{6}He (δ_p) and n+^{6}Li$_{IAS}$ (δ_n) scattering extracted for the ^{7}Li$_{IAS}$ resonance. The energy is relative to the proton threshold E_p.

As for the definition of $E_r^{(2)}$, things are more complex. For two unbound channels, both channels shown a rapid variation of the total phase shift near the resonance energy (Fig. 7.1). However, the energy where $d^2\delta_c/dE^2 = 0$ can be different for the two channels. Such a definition is channel specific and therefore not as useful.

Another often-used definition of the resonance energy is the pole of the S-matrix in the complex energy plane. At this complex energy $E^{(3)} = E_r^{(3)} - i\Gamma^{(3)}/2$, one has Gamow-state solutions where the probability decays exponentially in time and there is only an out-going wave asymptotically. This definition is also valid for multi-channel resonances as all elements of the S-matrix have poles at the same energy. This pole can be obtained from solving

$$E_\lambda + \Delta_{tot}(E^{(3)}) - E^{(3)} - i\frac{\Gamma_{tot}(E^{(3)})}{2} = 0. \tag{7.15}$$

7.5 Monte Carlo Simulation

In fitting the experimental line shape with the R-matrix parametrization, it is important to include the experimental resolution. This was determined via Monte Carlo simulations of the decay in all its aspects and also the detection apparatus. We made two sets of fits. First we include only the nucleon+core ($J^\pi = 0^+$) decay channels and thus we have only one channel for the $^7\mathrm{B}_{g.s.}$ resonance and two channels each for the isobaric states (see Fig. 7.2). These fits are comparable to those made for ^{7}He in Refs. [7, 8]. The R-matrix fit parameters are E_λ and the total spectroscopic strength $\mathbb{S}_{0^+}$. This strength is divided by the isospin Clebsch-Gordan coefficients into the ratios 2/3 and 1/3 for the proton and neutron decay channels of $^7\mathrm{Be}_{IAS}$ respectively. The ratios are reversed for $^7\mathrm{Li}_{IAS}$ decay. The spectroscopic strengths one obtains in these fits are, in principle, minimum values as they correspond to effective reduced widths [Eq. (7.12)] due to elimination of bound channels.

To see the effect of including unbound channels, we have also made fits including the nucleon+core (J^π=2^+) channels which requires the magnitude of $\mathbb{S}_{2^+}$ to be specified (see later). These J=2^+ daughter states are wide, especially the ^{6}Be first excited state. We therefore calculate the energy shift as an integral over the line shapes of the daughters;

$$\Delta_c(E) = -\gamma_c^2 \int w(E_0 - E_0^{cen}) \left[S(E - E_0) - S(E_\lambda - E_0) \right] dE_0 \tag{7.16}$$

where the weight $w(E_0 - E_0^{cen})$ is a normalized Breit-Wigner line shape and E_0^{cen} is the centroid of the daughter state. In principle these wide states should also show deviations from a Breit-Wigner form. We explored the sensitivity to their line shape by using Gaussian weights with the same FWHM and got equivalent results. For $^7\mathrm{B}_{g.s.}$ and $^7\mathrm{Be}_{IAS}$ decays, the line shapes of these wide daughter states extend into the continuum, Fig. 7.2, and so a similar integral over the line shape will contribute to the decay width $\Gamma_c(E)$. It is important to understand if this influences the predicted line shape significantly and shifts the fitted resonance energy.

For ^{7}B decay, the ^{6}Be daughters subsequently decay to the $2p$+α channel. The final ^{7}B exit channel is thus $3p$ + α events which can include the J^π=2^+ state of ^{6}Be as well. In order to determine the detector response we need to simulate the two-proton decay of these ^{6}Be levels. We have extensively studied the decay of both these levels in Ref. [78] where the correlations between the momentum of all three decay fragments is well described by Hyperspherical-Harmonic cluster model calculations [78]. We have used Monte-Carlo events generated by this cluster model for the decay of ^{6}Be fragments in our simulations.

The only significant contributions to the experimental resolution come from the energy-loss and small-angle scattering of the final fragments in target and the energy resolution of the CsI(Tl) E detectors. As in our previous work [24], the target effects were treated as described in Refs. [79, 80]. The CsI(Tl) resolutions, which may be particle dependent, were determined by fitting a narrow resonance where the exit channels contained the same two particles as in the resonance of interest. This fitting was made individually for each of the A=7 resonances using data measured during the same experiment. For the $^7\mathrm{Li}_{IAS} \rightarrow p$+^{6}He decay, we used the ^{6}Li(J=3^+, E^*=2.186(2) MeV)$\rightarrow d + \alpha$ resonance of width Γ=24(2) keV to fine tune the CsI(Tl) resolution while for the $^7\mathrm{Be}_{IAS} \rightarrow p$+^{6}Li resonance the ^{8}Be(J^π=1^+, E^*=17.640(1) MeV, Γ=10.7(5) keV)$\rightarrow p$+^{7}Li was used. Finally for the $^7\mathrm{B}_{g.s.}$ resonance that decays to the $3p$+α channel, we used the $^6\mathrm{Be}_{g.s.}$(J^π=0^+, Γ=92(6) keV)$\rightarrow 2p + \alpha$ decay for this fine tuning. The extracted CsI(Tl) resolutions were similar in all cases.

7.6 Analysis

7.6.1 General Consideration

Figure 7.2 presents partial energy-level diagrams for the $A = 7$, $T = 3/2$ isobar showing only the levels relevant for this work. In fitting the experimental line shapes we used the channel radius a_c=4 fm for all channels for consistency with the ^{7}He R-matrix analyses in Refs. [7, 8]. For each system, we first fit the invariant-mass spectrum with the nucleon+core (J^π=0^+)

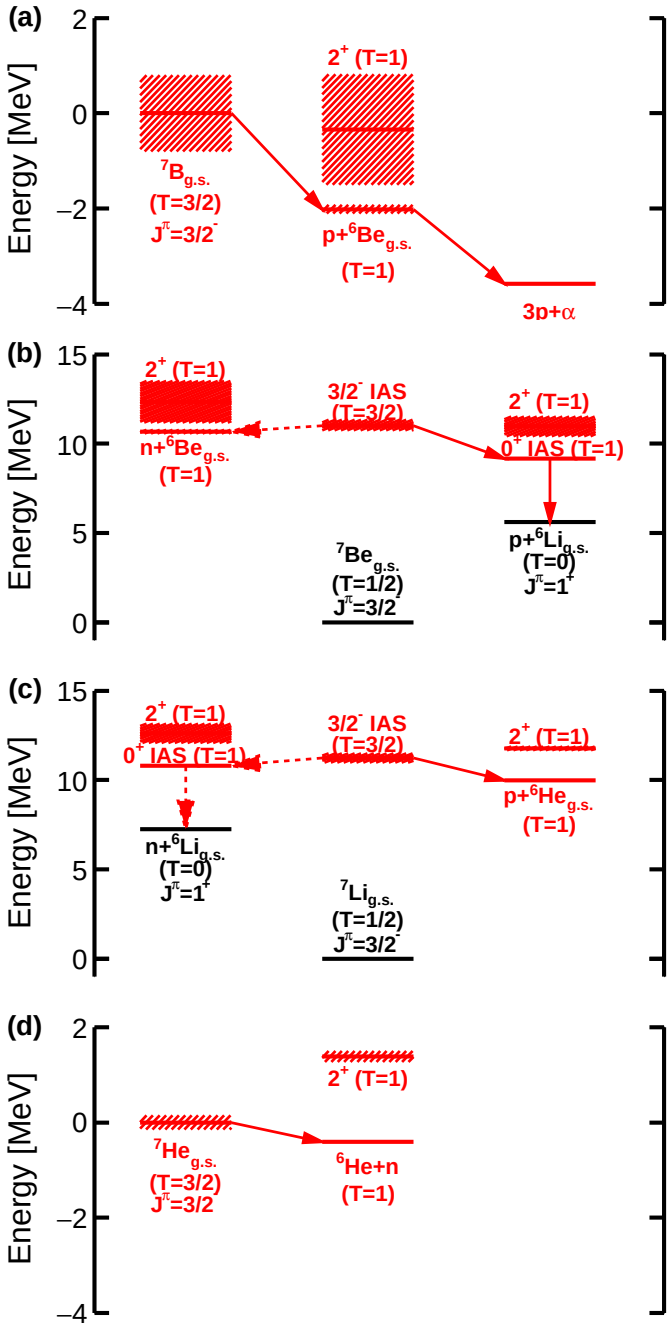

Figure 7.2: (Color Online) Set of levels relevant for the decay of the $T = 3/2$ members of the $A = 7$ quartet, with (a)-(d) arranged with increasing T_Z. The levels are labeled by their spin-parity (J^π) and isospin (T) quantum numbers. Observed, isospin-allowed decays are shown with solid red lines, and unobserved, isospin-allowed decays are shown with dashed red lines. Levels to which particle decay is allowed are shown in red. The properties of the A=6 states are listed in Table 7.1

Table 7.1: Excitation energy and widths of the A=6 daughter states from Ref. [9].

state		^{6}He	^{6}Li	^{6}Be
J=0$^+$	E^* [MeV]	0.	3.563	0.
	Γ [MeV]	0.	8.2×10^{-6}	0.092(6)
J=2$^+$	E^* [MeV]	1.797(25)	5.366(15)	1.670(15)
	Γ [MeV]	0.113(20)	0.541(20)	1.16(6)

channels. The dimensionless single-particle reduced widths $\theta^2_{s.p.}$ were obtained from the overlap functions predicted with the Variational Monte Carlo (VMC) or the Green's Function Monte Carlo (GFMC) methods in Ref. [6] using Eq. (7.11). Calculated reduced overlap functions from the two theoretical methods are displayed in Fig. 7.3 for the $^7\mathrm{He}_{g.s.} \rightarrow n{+}^6\mathrm{He}_{g.s.}$ decay. The more recent VMC calculations use the Argonne v18 two-nucleon (AV18) [81] and Urbanna X three-nucleon [82] potentials while the GFMC results used the same two-nucleon potential but the Illinois-7 three-body interaction (IL7)[83]. Both methods treat this unbound channel as being pseudo-bound and thus the asymptotic behavior should be ignored. The dashed curves are from single-particle calculations with a Wood-Saxon potential $V(r)$ whose depth was adjusted to give the correct resonance energy, while the radius and diffuseness parameters were adjusted to fit theoretical overlap functions inside the channel radius (a_c=4 fm, vertical dashed line in Fig. 7.3).

These single-particle overlap functions give us an indication of the radial extent to which the GFMC and VMC overlaps should be trusted. If the channel radius a_c were to be shifted further out from our value of a_c=4 fm, then it would be problematic to use the direct theoretical overlap functions to calculate $\theta^2_{s.p}$, especially for the VMC calculation. In such cases the dashed curves would be a better choice for determining $\theta^2_{s.p.}$.

The $\theta^2_{s.p.}$ values for the $^7\mathrm{He}_{g.s.} \rightarrow n{+}^6\mathrm{He}_{g.s.}$ are 0.584 and 0.700 for the GFMC and VMC methods respectively. For the VMC method, calculated overlap functions for the nucleon+core (J^π=0$^+$) channels of the other isotopes were very similar in shape and subsequently the $\theta^2_{g.s.}$ values only ranges from 0.700 ($n{+}^6\mathrm{He}_{g.s.}$) to 0.724 ($p{+}^6\mathrm{Be}_{g.s.}$), a 3% variation. Such calculations were not available for the GFMC method and so a constant

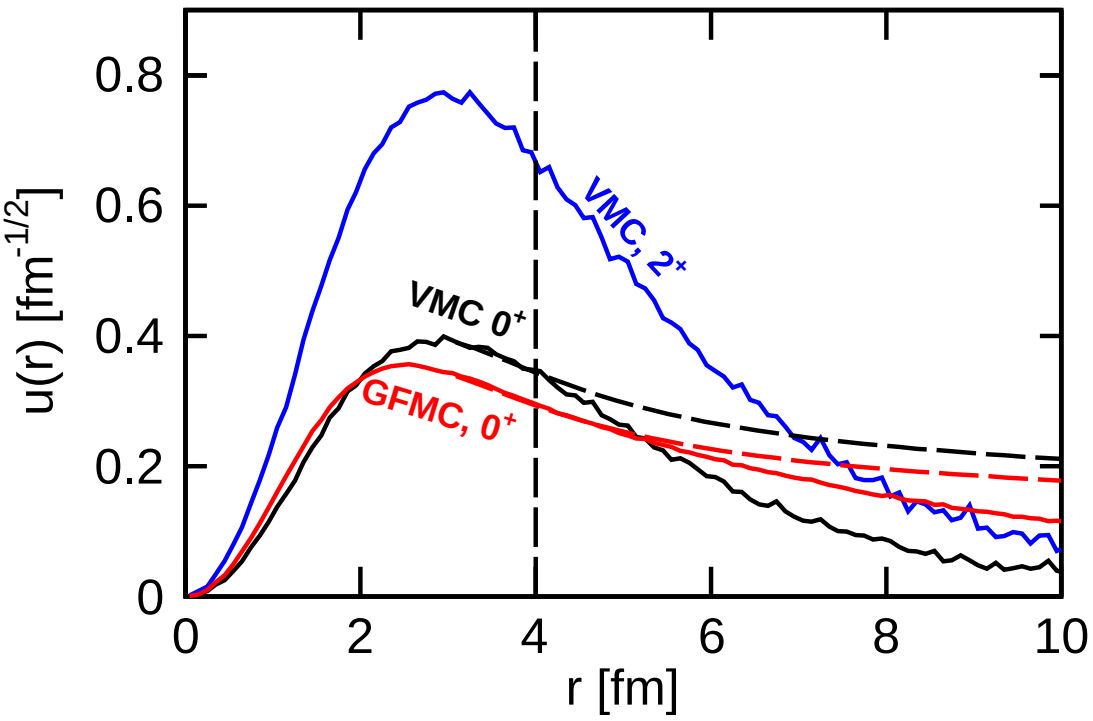

Figure 7.3: (Color Online) Overlap function predicted by the GFMC and VMC method for the $^7\mathrm{He}_{g.s.} \rightarrow n{+}^6\mathrm{He}$ channels. For the the VMC methods, results are shown for decays to the ground ($J^\pi{=}0^+$) and first excited state ($J^\pi{=}2^+$) state of ^{6}He, while only the ground state is shown for the GFMC method. The $J^\pi{=}0^+$ channel is unbound and the dashed curves show single-particle overlaps with the correct asymptotic behavior that match with the theoretical calculations in the interior region (see text for details).

$\theta^2_{g.s.}$=0.584 was used for all $J^\pi{=}0^+$ channels.

To gauge the effect of the $J{=}2^+$ channels we have also performed R-matrix fits with these channels included. The overlap function for the bound $^7\mathrm{He}_{g.s.} \rightarrow n{+}^6\mathrm{He}(2^+)$ channel predicted with the VMC method is also shown in Fig. 7.3. This overlap is for the $p_{3/2}$ orbital only and has a large spectroscopic factor of $\mathbb{S}_{2^+}$=2.05. For comparison the shell-model prediction (code Nushell@MSU[84]) with the Cohen-Kurath effective interaction [85, 86] is $\mathbb{S}_{2^+}$=1.34 (including center-of-mass corrections). There is also a small $p_{1/2}$ contribution predicted by the VMC method with strength $\mathbb{S}$ = 0.008 that we have ignored. As both these $J{=}0^+$ and $J{=}2^+$ channels are $p_{3/2}$ in nature, it is not surprising that their overlap functions have similar shapes in the interior regions. For the $n{+}^6\mathrm{He}(2^+)$ channel, $\theta^2_{s.p.}$=0.685

which is very similar to the value for the corresponding J=0^+ channel ($\theta^2_{s.p.}$=0.700). Results for corresponding channels in the other isotopes are also similar with a value of $\theta^2_{g.s.}$=0.733 obtained for p+^{6}Be(2^+). No overlap functions and spectroscopic factors are available for the GFMC method for the J^π=2^+ channels. For illustrative purposes in this case, R-matrix fits were performed with a value of $\theta^2_{s.p.}$=0.584 (same as for the J^π=0^+ channels) and $\mathbb{S}_{2^+}$=2.0.

For each of the three resonances, the fitted energies $E_\lambda = E_r^{(1)}$ are listed in Table 7.2 and the fitted spectroscopic strengths are listed in Table 7.3. The systematic errors quoted in the following discussions contain contributions from the uncertainties in the energy and angular calibrations of the detectors. This was gauged by comparing the invariant mass of known narrow resonances found in the same data set. See Table 7.4 for a list of these resonances and their extracted energies.

Table 7.2: Resonance energies and decay widths extracted from the R-matrix analyses of the $A = 7$ cases. The $E_r^{(2)}$ resonance energy is channel dependent and thus values are listed from both proton (p) and neutron (n) exit channels.

Nuclide	resonance energy [MeV]				Γ [keV]	
	$E_r^{(1)}$	$E_r^{(2)}$	$E_r^{(3)}$	$E_r^{(ENSDF)}$	R-matrix	ENSDF
^{7}He [7]	0.387(2)	0.372(2)(n)	0.372(2)	0.410(8)	132(3)	150 (20)
^{7}He [8]	0.430(3)	0.416(3) (n)	0.416(3)		131	
^{7}Li	1.288(15)	1.288(15) (p)	1.269(15)	1.266 (30)	191(41)	260(35)
		1.288(15) (n)				
^{7}Be	1.82(2)	1.79(2) (p)	1.78(2)	1.840(30)	376(47)	320(30)
		1.85(2) (n)				
^{7}B	2.037(35)	1.963(38)(p)	1.963(38)	2.013 (25)	599(113)	801(20)

7.6.2 ^{7}Li$_{IAS}$

The isobaric analog state (IAS) in ^{7}Li has two energy- and isospin-allowed decay channels, Fig. 7.2(c). It can neutron decay to the isobaric analog state in ^{6}Li, which then decays to the ground-state via a 3.563 MeV γ ray, or it can proton decay to the ground-state of ^{6}He. Our detectors are not sensitive to neutrons, so only the proton decay channel was observed. Using the invariant-mass method, the ^{7}Li excitation energy was reconstructed from the

Table 7.3: Spectroscopic factors $\mathbb{S}_{0^+}$ extracted from the R-matrix fits in this work. Results are listed for both the $\theta^2_{s.p.}$ values obtained from the GFMC and VMC overlap functions and for $\mathbb{S}_{2^+}$=0 and $\mathbb{S}_{2^+}$=2.0

Nuclide	$\mathbb{S}_{g.s.}$				Ref.
	GFMC		VMC		
	$\mathbb{S}_{2^+}=0$	$\mathbb{S}_{2^+}=2.0$	$\mathbb{S}_{2^+}=0$	$\mathbb{S}_{2^+}=2.0$	
^{7}He	0.52(2)	0.99(4)	0.43(1)	0.89(2)	[7]
^{7}He	0.43(1)	0.82(2)	0.36(1)	0.74(2)	[8]
^{7}Li	0.39(11)	0.79(20)	0.33(9)	0.79(20)	[*]
^{7}Be	0.48(9)	0.94(12)	0.40(7)	0.89(12)	[*]
^{7}B	0.56(14)	0.98(27)	0.45(11)	0.82(20)	[*]

detected p+^{6}He events. The excitation-energy spectrum from the polyethylene-target data, shown in Fig. 7.4, displays a strong peak corresponding to the IAS. The reaction mechanism responsible for the creation of this state is complex in that it involves the loss of 5 nucleons from the projectile. There are possible contributions from direct knockout and decays of other heavier resonances.

In our R-matrix fits we have considered two parametrization for the background under the peak. The first is just a quadratic, i.e.,

$$b_1(E_T) = a_1 + a_2 E_T + a_3 E_T^2 \tag{7.17}$$

where the a_n coefficients were fit simultanously the R-matrix parameters. The second background form,

$$b_2(E_T) = \frac{a_1 + a_4\,(E_T - a_2)}{1 + \exp\left[(E_T - a_2)/a_3\right)}, \tag{7.18}$$

in principle, allows for a more complex variation of the background under the peak. The best fitted excitation-energy distributions with both background parameterizations and S_{2^+}=0 are shown Fig. 7.4 as the solid curves. However, the two fits are almost identical and cannot be differentiated in this figure. On the other hand, the fitted backgrounds indicated by the dotted (b_1) and dashed (b_2) curve are somewhat different. The choice of background is not important for extracting the peak energy as the fitted $E_r^{(1)}$ values differ by 0.2 keV compared

to a statistical error of 3 keV. However, the extracted spectroscopic strength and width of the peak have a much larger sensitivity to the background form (see later).

From the fitted resonance energy $E_r^{(1)}$, the excitation energy of this level is $E^* = 11.267 \pm 0.003$ MeV (statistical), with a systematic uncertainty of 0.015 MeV. A fit of the data from the carbon target agrees within 2 keV. While this is just within the 1σ error bound of the previous value ($E^* = 11.240 \pm 0.03$ MeV) [9], the uncertainty is reduced by a factor of two. A four channel fit with $\mathbb{S}_{2^+}$=2 was also made, however, the resulting curve is almost identical to that obtained with the two-channel fit in Fig. 7.4. The fitted resonance energy $E_r^{(1)}$ was less than 1 keV smaller in value, confirming that the Thomas approximation (Sec. 7.3) is valid for this resonance. The elimination of bound channels therefore has negligible effect on the extracted resonance energy. The Thomas approximation that $\Delta_c(E)$ is linear in energy, is not expected to hold for energies significantly different from the resonance energy and indeed small modifications of the intrinsic line shape in the tail region are found, but these are easily compensated by adjustments to the background contributions in the fit.

From the best fits, the branching ratios for the n+^{6}Li$_{IAS}$ and the p+^{6}He$_{g.s.}$ decay channels are 47% and 53% respectively. This result was found for the fits with both $\mathbb{S}_{2^+}$=0 and $\mathbb{S}_{2^+}$=2.0 and also those with the θ^2 parameters obtained from either the VMC and GFMC overlap functions.

7.6.3 ^{7}Be$_{IAS}$

The level structure for ^{7}Be, Fig. 7.2(b), is very similar to that of ^{7}Li. There are two energy- and isospin-allowed decays, neutron decay to ^{6}Be$_{g.s.}$ or proton decay to the IAS in ^{6}Li. However in this case, the proton decay will be followed by γ emission. Figure 7.5 shows the γ-ray spectrum tagged by the p+^{6}Li channel. The spectrum has been Doppler corrected event-wise and contains add back of Compton scattered γ rays detected in neighboring crystals of the CAESAR array. The selection of events which have the 3.563 MeV γ ray (G1 in Fig. 7.5), identifies $T = 3/2$ states in ^{7}Be. A spectrum of the excitation energy,

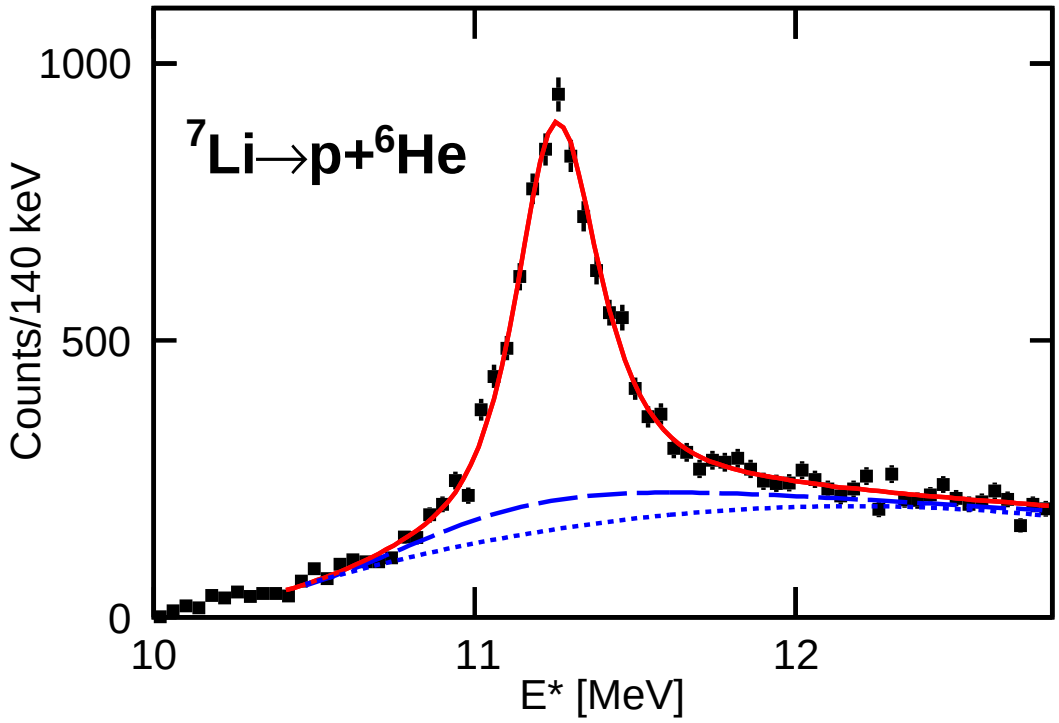

Figure 7.4: (Color Online) The excitation energy spectrum for ^{7}Li reconstructed from all p+^{6}He events. The red solid curve is our R-matrix fit with $\mathbb{S}_{2^+}$=0 (θ_c^2 taken from GFMC [6]). Two almost identical fits were made with different background contributions. The dotted and dashed curves indicated the fitted background obtained using parametrizations. b_1 and b_2, respectively.

less the γ-ray energy, from p+^{6}Li events selected by this γ-ray is shown as the solid curve in Fig. 7.6(a). Previously it was determined in this experiment that ^{8}B$_{IAS}$ fragments, produced by one-proton knockout, decay by two-proton emission to the IAS in ^{6}Li [14, 87]. Therefore decays of ^{8}B$_{IAS}$ where one proton is not detected will contaminate this spectrum. By taking the detected p+p+^{6}Li events gated on the 3.563 MeV γ ray and throwing away one of the protons, a background spectrum can be constructed. The relative magnitude of this contamination was determined by Monte Carlo simulations of the ^{8}B$_{IAS}$ decay. This contamination (blue dashed curve) accounts entirely for the peak around 6.5 MeV in Fig. 7.6(a). The majority of the p+^{6}Li yield comes from $2p$ knockout reactions, with a small contribution from sequential decay of $T = 2$ states in ^{8}B. The latter is the second higher-energy peak in the blue dashed curve. There is also a background under the peak in the

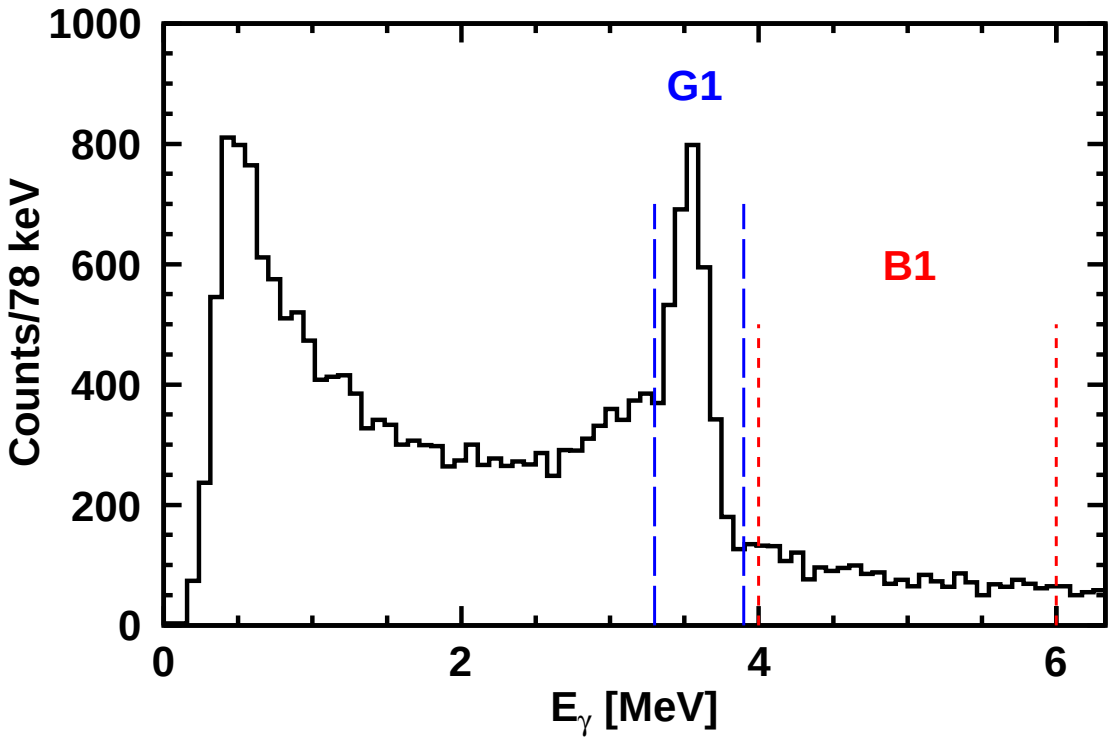

Figure 7.5: (Color Online) The Doppler-corrected γ-ray spectrum measured in coincidence with detected p+^{6}Li events.

G1 gate in Fig. 7.5. The resulting contribution to the excitation-energy spectrum can be approximated by taking reconstructed p+^{6}Li events in coincidence with the gate B1 in Fig. 7.5. This contribution, scaled by the relative widths of the G1 and B1 gates, is shown as the red dotted curve in Fig. 7.6(a). The background-subtracted histogram is displayed in Fig. 7.6(b).

A fit of this spectrum with just two unbound channels ($\mathbb{S}_{2^+}$=0) and no residual background is shown as the solid curve in this figure. Fits which included a smooth background contribution were also made, but gave almost identical R-matrix parameters. The extracted excitation energy from the $E_r^{(1)}$ resonance energy is $E^* = 10.989 \pm 0.004$ MeV (statistical) with a systematic uncertainty of 0.015 MeV. This is within the error bar from the previous value of 11.010±0.030 MeV [9], but reduces the uncertainty by half. Again the four channel fit ($\mathbb{S}_{2^+}$=2.0), produced an almost identical curve to that shown in Fig. 7.6(b) and the same resonance energy. The fitted branching ratios for the n+^{6}Be$_{g.s}$ and p+^{6}Li$_{IAS}$ decay channels

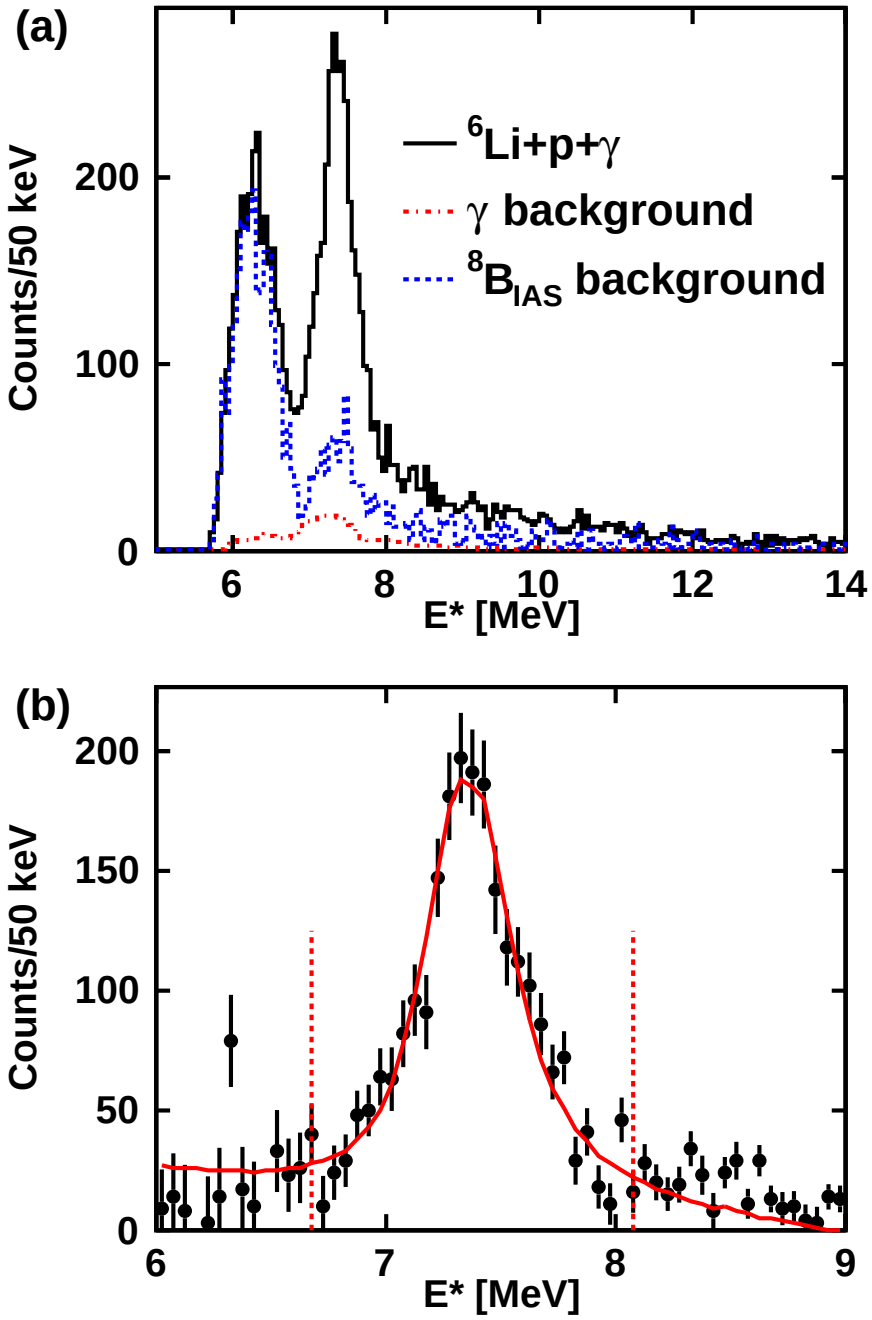

Figure 7.6: (Color Online) (a) Reconstructed minimum excitation-energy spectrum (missing the γ energy) for the p+^{6}Li events in coincidence with a 3.563 MeV γ ray (G1 in Fig. 7.5). The blue dashed histogram indicates a contamination from ^{8}B+p+p+γ events where one proton misses the array. The red dot-dashed histogram is a background from the γ-ray gate (B1 in Fig. 7.5). (b) The points are the background-subtracted excitation-energy spectrum. The red solid curve is a simulation of the decay from ^{7}Be$_{IAS}$ using a R-matrix line shape (θ_c^2 taken from GFMC [6]) with the experimental resolution included.

are 9% and 91%, respectively.

7.6.4 $^{7}B_{g.s.}$

The $3p$+α invariant-mass spectrum in Fig. 7.7 was published previously by us in Ref. [24]. The particles were produced following interactions of an E/A=70-MeV ^{9}C beam with a ^{9}Be target and the final decay fragments were detected in the HiRA array configurated in almost the same arrangement as for the $^{7}Be_{IAS}$ experiment.

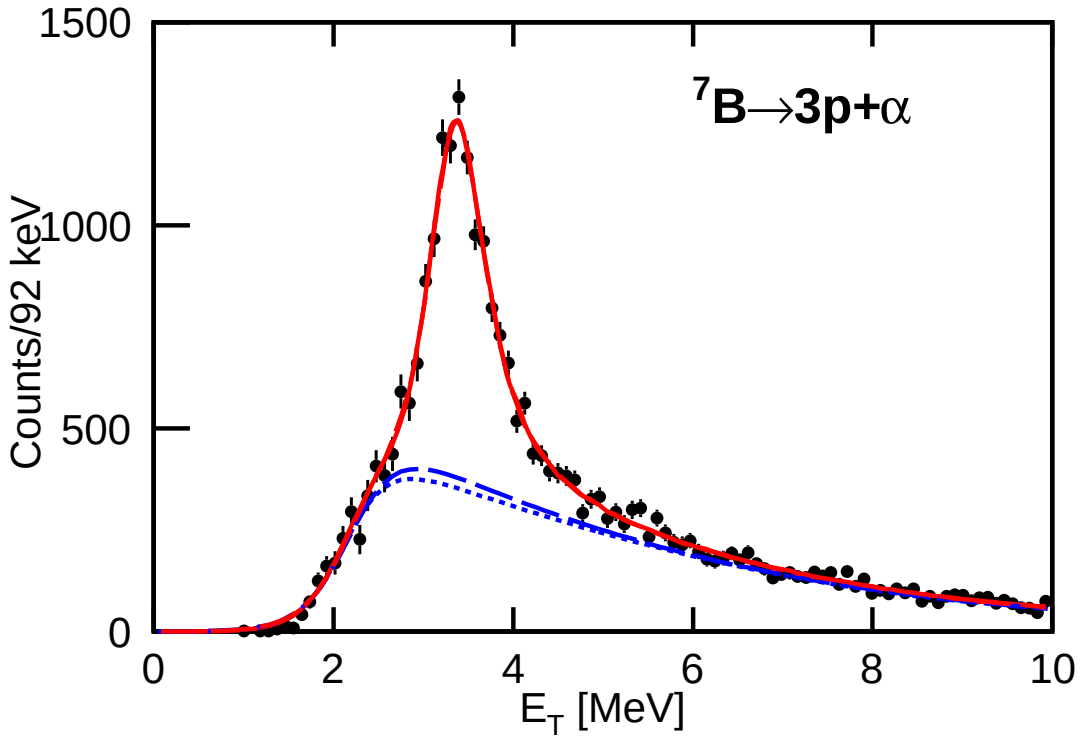

Figure 7.7: (Color Online) Invariant mass of ^{7}B from all detected $3p$+α events. Two R-matrix fits with $\mathbb{S}_{2^+}$=0 are shown as the red solid curve using both background parameterizations. These two fits are almost identical and cannot be differentiated, but their fitted backgrounds are somewhat different. The blue dotted and blue dashed curves were obtained with the b_3 and b_4 parameterizations, respectively.

This spectrum has been corrected for the contribution from $^{8}C_{g.s.}$ $\rightarrow 4p$+α events where only three of the protons are detected. This correction involving taking detected $4p$+α events and throwing one of the protons away. The resulting $3p$+α invariant-mass spectrum was scaled by the number of such events predicted in our Monte Carlo simulation of $^{8}C_{g.s.}$ decay

and subtracted from the raw data [24]. This correction did not change the peak location significantly which largely determines the resonance energy. In extracting the uncertainties for R-matrix parameters we have considered a $\pm 10\%$ uncertainty in the normalization of these pseudo $3p$+4α events. In addition to removing the contribution from $^8\mathrm{C}_{g.s.}$ peak, we have also considered the effect of removing the contribution from higher excitation $4p$+α events that form a tail on the ground state. This was not done in Ref. [24]. This tail is rather flat and this subtraction does not make a significant change in the fitted resonance energy.

Even after subtracting these background components, the resulting spectrum still shows a considerable residual background under the ^{7}B resonance. Indeed this residual background is not smooth as the total counts drops sharply for the decay energies E_T below 2 MeV. The nature of this background with its threshold-like feature is unclear. As it extends below the ^{7}B ground-state peak and then drops sharply, it cannot be an excited ^{7}B resonance. To explore the sensitively of extracting the R-matrix parameters, we have used two different parameterizations for the residual background which can produced quite different shapes. The first parametrization,

$$b_3(E_T) = \frac{a_1 + a_2 E_T + a_3 E_T^2}{1 + \exp\left[-(E_T - a_4)/a_5\right]} \tag{7.19}$$

is a quadratic polynomial with an inverse Fermi function to produce the threshold-like feature. The second parametrization is

$$\begin{aligned} b_4(E_T) &= a_1 \frac{1}{1 + \exp\left[-(E_T - a_2)/a_3\right]} \frac{1}{1 + \exp\left[(E_T - a_4)/a_5\right]} \\ &+ a_6 \frac{1 - a_7 * (E_T - a_4)}{1 + \exp\left[-(E_T - a_4)/a_5\right]} \end{aligned} \tag{7.20}$$

The best-fit curves with these two background parameterizations and a single channel in the R-matrix prescription ($\mathbb{S}_{2^+}$=0) are almost identical and are shown by the solid curve in

Fig. 7.7. While these two curves are the same, their decomposition into peak and residual background components are somewhat different. The fitted background contributions are indicated by the dotted [$b_3(E)$] and dashed [$b_4(E)$] curves in this figure. The fitted resonance energy is $E_r^{(1)}$=2.036±0.009 MeV (statistical) with a systematic error of 26 keV which the includes the uncertainties from the various background contributions.

For this resonance, the p+^{6}Be(2^+) channel is partially unbound [Fig. 7.2(a)] and would also contribute to the detected $3p$+α events. Therefore it is important to understand how it affects the shape of the ^{7}B invariant-mass peak. We therefore refit the experimental data with a two-channel R-matrix expression with $\mathbb{S}_{2^+}$=2.0 and the resulting fitted curve and resonance energy are almost identical to that obtained with just one channel ($\mathbb{S}_{2^+}$=0). Fig. 7.8 compares the fitted intrinsic lines shapes attained from the one and two-channel fits with the $b_4(E_T)$ background parameterization. The two line shapes are essentially identical except for the high-energy tail region with the same FWHM. Our fits are insensitive to the magnitude in the tail region as any change in the tail is easily compensated by changes in the background contribution. Thus the main effect of including the decay to the 2^+ state, similar to that obtained for the other A=7 resonances, is to modify the spectroscopic factor extracted for the main decay channel. We would like to point out that the extracted width is smaller, but with a larger uncertainty, than the ENSDF value (see Table 7.2). The latter was in fact from our previous analysis [24] that we now know had a fitting error.

7.7 Isobaric Multiplet Mass Equation

From the R-matrix fits in Sec. 7.6 we have learned that the extracted resonance energies are independent on whether the nucleon+core (J^π=2^+) channels are included or not. Up until this point, we have concentrated on the $E_r^{(1)}$ definition of the resonance energy. Table 7.2 compares these values to those obtained from from the poles of the S matrix ($E_r^{(3)}$) via Eq. (7.15). Not unexpectedly, the largest difference between these two resonance energies of

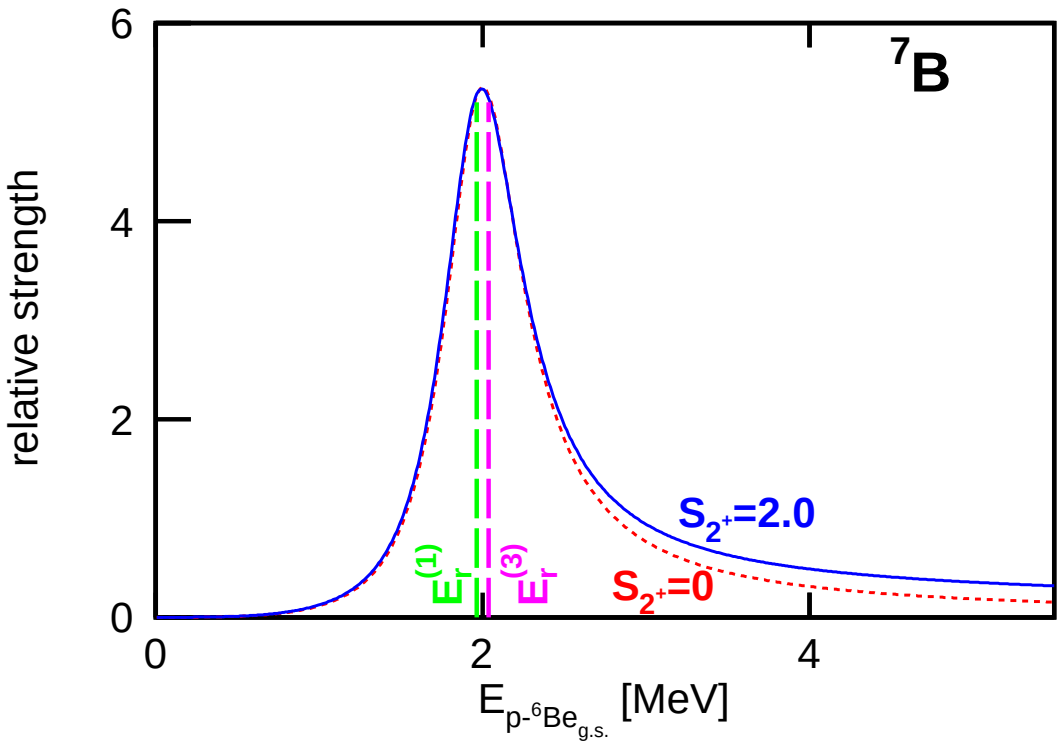

Figure 7.8: (Color Online) R-matrix line shape for ^{7}B with (without) the contribution of the $J^\pi = 2^+$ state included shown as the red dotted (blue solid) curve.The location of the resonance energy input to the R-matrix ($E_r^{(1)}$) is shown in green, and the resonance energy from the pole of the S-matrix ($E_r^{(3)}$) is shown in magenta.

74 keV is for the widest resonance $^7B_{g.s.}$. The location of these two resonance energies are indicated on the Fig. 7.8 which displays the fitted intrinsic line shape. The value obtained from the pole of the S matrix ($E_r^{(3)}$) is located just below the maximum of the line shape while the other value $E_r^{(1)}$ sits just above. This difference varies quite smoothly across the quartet and therefore it can easily be accounted for in the quadratic IMME.

The experimental masses of the T = 3/2 quartet obtained from the $E_r^{(1)}$ definition are listed in Table 7.5. In this case the mass of ^{7}He is taken from Ref. [8]. The most recent mass evaluation for this nucleus is based on the $E_r^{(1)}$ resonance energy [67]. Figure 7.9 shows a comparison between the residuals of a quadratic fit with the previous masses (closed circles) [88] and a quadratic fit with the new masses determined ether with the $E_r^{(1)}$ (closed triangles) or the $E_R^{(3)}$ (open triangles) definitions. The error bars used in the fit are estimates

Table 7.4: Comparison between the measured excitation energies (E^*_{exp}) and the literature values (E^*_{ENSDF}) [9] for narrow resonances used to estimate the systematic uncertainties in the two experiments. The deviation is given as $\Delta E^* = \left|E^*_{exp} - E^*_{ENSDF}\right|$. For the $^7B_{g.s.}$ experiment, we list equivalent results for the total decay energy E_T of ^{6}Be.

Channel	J^π	E^*_{exp} (MeV)	E^*_{ENSDF} (MeV)	ΔE^* (keV)
		$^7Li_{IAS}$		
^{6}Li$\rightarrow d+\alpha$	3^+	2.1930 (3)	2.186 (2)	7 ± 2
^{7}Li$\rightarrow t+\alpha$	$7/2^-$	4.6315 (7)	4.630 (9)	1 ± 9
^{8}Be$\rightarrow p+^7$Li	1^+	17.643 (1)	17.6400 (10)	3.0 ± 1.4
^{10}B$\rightarrow \alpha+^6$Li	3^+	4.7827 (13)	4.7740 (5)	8.7 ± 1.4
^{9}B$\rightarrow p+\alpha+\alpha$	$5/2^-$	2.3610 (11)	2.345 (11)	16 ± 11
^{10}B$\rightarrow p+^9$Be	2^+	7.4829 (50) [1]	7.470 (4)	13 ± 6
	2^-		7.479 (2)	3 ± 5
		$^7Be_{IAS}$		
^{6}Li$\rightarrow d+\alpha$	3^+	2.1850 (2)	2.186 (2)	1 ± 2
^{8}Be$\rightarrow \alpha+\alpha$	0^+	0.0014 (3)	0.00 (7)	1.4 ± 0.3
^{8}B$\rightarrow p+^7$Be	1^+	0.7692 (3)	0.7695 (25)	0.3 ± 2.5
	3^+	2.3207 (7)	2.320 (20)	1 ± 20
^{8}B$\rightarrow p+p+^6$Li	0^+	10.6149 (2)	10.619 (9)	4 ± 9
^{9}B$\rightarrow p+\alpha+\alpha$	$3/2^-$	0.007 (1)	0.0000(9)	7 ± 1
	$5/2^-$	2.358 (2)	2.345 (11)	13 ± 11
^{8}Be$\rightarrow p+^7$Li	1^+	17.6470 (8)	17.6400 (10)	7.0 ± 1.3
		E_T^{exp} (MeV)	E_T^{ENSDF} (MeV)	ΔE_T (keV)
		$^7B_{g.s.}$		
^{6}Be$\rightarrow p+p+\alpha$	0^+	1.364(6)	1.371(5)	7±11

of the systematic uncertainty. The statistical errors are about a factor of three smaller. As expected the residuals obtained using the two definitions of the resonance energy are very similar. The IMME coefficients from the two fits are listed in Table. 7.6. It is clear that the quadratic fit reproduced the masses very well; with χ^2/n=0.66 ($E_r^{(1)}$) and χ^2/n=0.38 ($E_r^{(3)}$). A fit with a cubic dependence yields coefficients for the T_Z^3 term of d=19.5±13.8 keV for both definitions, consistent with zero within the 2σ limit. As mentioned previously, GFMC (AV18+IL7) calculations, where charge independence breaking interactions are included, predict a value of d= 7.5±2.5 keV [10]. The other coefficients from this calculations are also listed in Table 7.6 and compared to the cubic fit coefficients from this work. They predict

a slightly larger T_Z dependence than our two fits. However the predicted cubic term is still consistent with our experimental result. The largest contribution to d in these calculations is from the expansion of the nucleus with decreasing T_Z. More accurate determination of the experimental masses are needed to confirm if a non-zero d of this magnitude is required. A quadratic fit of the experimental masses using instead the mass of ^{7}He from Ref. [7] provides a very similar fit with χ^2/n=1.23 ($E_r^{(1)}$) and χ^2/n=0.84 ($E_r^{(3)}$).

Table 7.5: Mass excesses for the A = 7, isospin T = 3/2 quartet using the $E_r^{(1)}$ resonances energies and the coefficients from the quadratic fit.

Nucl.	T_Z	Mass excess (keV)	a,b,c (keV)
^{7}B	-3/2	27700 (35)	a = 26406 (14)
^{7}Be	-1/2	26758 (20)	b = -557 (11)
^{7}Li	1/2	26169 (15)	c = 213 (10)
^{7}He	3/2	26050 (8)	χ^2/n = 0.66

Table 7.6: Comparison of the coefficients obtained from the cubic fits to the quartet masses for the two definitions of resonance energy ($E_r^{(1)}$, and $E_r^{(3)}$) and from the GFMC calculations of Ref. [10].

Coef.	$E_r^{(1)}$	$E_r^{(3)}$	GFMC
b	-594(28)	-574(28)	-591(8)
c	206(11)	198(11)	237(8)
d	19(14)	19(14)	7.5(2.5)

We have also considered the sensitivity of results to the choice of the channel radius. In addition to the fits with a_c=4 fm, we repeated the fitting with a_c=5.5 fm. The $\theta^2_{s.p.}$ values were determined from the dashed-curve in Fig. 7.3 with the correct asymptotic behavior. The fitted resonance energies shifted by less than 2 keV, much less that our experimental uncertainties and therefore this can be ignored. In addition the fitted resonance energies were the same for the VMC and GFMC values of $\theta^2_{s.p.}$.

We have also looked at the result with the second definition of resonance energy $E_r^{(2)}$ based on the derivative of the phase shift which is problematic in that it may have a channel dependence for the isobaric analog states (Sec. 7.4). For the ^{7}Li$_{IAS}$ where the decay branches

for the neutron and proton are similar (Sec. 7.6.2), the deduced values of $E_r^{(2)}$ are identical, see Table 7.2. However for the $^7\mathrm{Be}_{IAS}$, the two values differ by 54 keV. If we take the value for the dominant p+$^6\mathrm{Li}_{IAS}$ channel and construct the IMME with this and the other $E_r^{(2)}$ values we also get small residuals with a χ^2/n of 0.98 which is only slightly larger than those for the other definitions of the resonance energy.

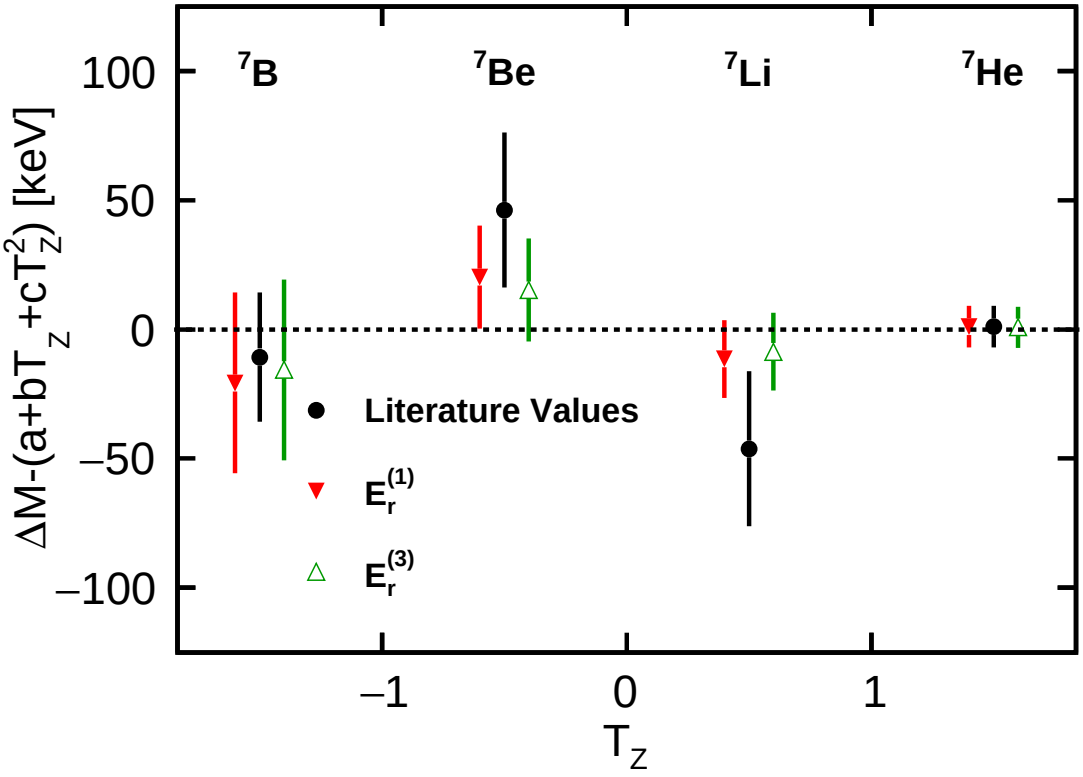

Figure 7.9: (Color Online) Deviation from the fitted quadratic form of the IMME for the lowest $T = 3/2$ states in the $A = 7$ isobar. The data points for the $E_r^{(1)}$ and $E_r^{(3)}$ definitions are shifted by 0.1 and 0.2, respectively, along the abscissa for clarity.

7.8 Variation of Spectroscopic Strength

To the extent that isospin is a good quantum number, the spectroscopic strength $\mathbb{S}_{0^+}$ should be constant across the quartet. Figure 7.10 shows the variation of the fitted $\mathbb{S}_{0^+}$ values as a function of the isospin projection T_Z. Results are shown for $\mathbb{S}_{2^+}$=0 (open-squares) and for

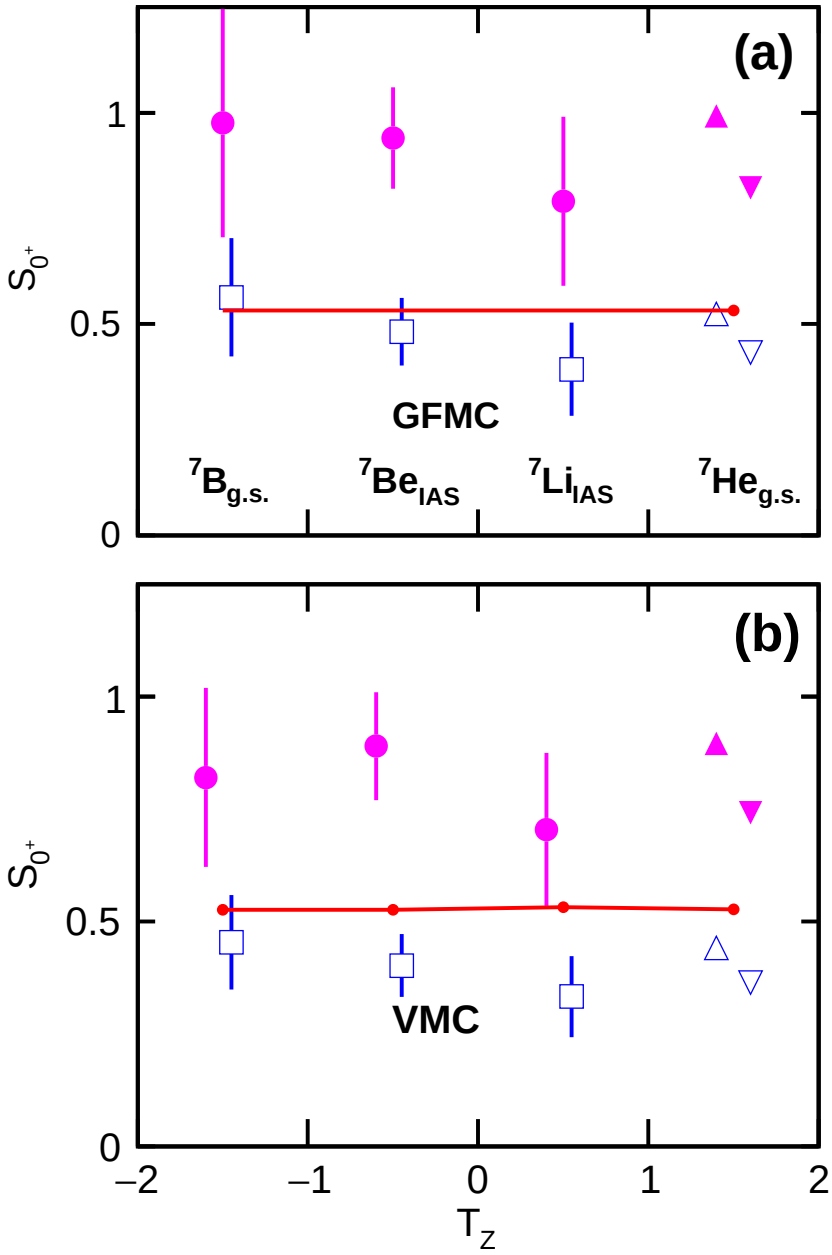

Figure 7.10: (Color Online) Ground-state spectroscopic factor as a function of isospin projection (T_Z) using θ_c^2 from (a) Green's Function Monte Carlo and (b) VMC. The open blue data points have $S_{2^+} = 0$ and the solid magenta data points have $S_{2^+} = 0.75$. The top- and bottom-pointing triangles are from [7] and [8], respectively. The horizontal lines show the predicted spectroscopic factors for $^7\mathrm{He}_{g.s.}$ from the respective models.

$\mathbb{S}_{2^+}$=2.0 (filled circles) and for the $\theta^2_{s.p.}$ determined from the GFMC [fig. 7.10(b)] and VMC [Fig. 7.10(b)] overlap functions. The effect of including the decays to the J^π=2^+ daughters is very important. The addition of the bound channels increases the fitted $\mathbb{S}_{0^+}$ spectroscopic strength by roughly a factor of two for all resonances. This is of course dependent on our assumed values of $\mathbb{S}_{2^+}$. However, the addition of bound channels will always increase the fitted spectroscopic strength of the unbound channel. At the channel radius the bound channel mixes with the unbound channels, pulling decay strength away from the unbound channel, therefore the spectroscopic strength of the unbound channel must increase in order to reproduce the observed decay width.

For ^{7}He$_{g.s.}$, we include spectroscopic strengths extracted from the fitted reduced widths γ^2_c listed in Ref. [7] (up-facing triangles) and Ref. [8] (down-facing triangles) from single-channel R-matrix fits. The results for $\mathbb{S}_{2^+}$=2 in Fig. 7.10 and Table 7.3 were obtained from fitting the intrinsic lines shapes obtained with the single-channel fits. The authors of these two studies use a different method to extract the spectroscopic factor from the reduced width involving a comparison of the fitted reduced width to that obtained for the ^{5}He resonance which is assumed to be a single-particle resonance. This procedure will not account for the difference in eliminated channels for the two resonances. However their spectroscopic factors are not too different from our $\mathbb{S}_{2^+}$=0.0 value with $\mathbb{S}_{0^+}$=0.619(22) [7] and 0.512(18) [8].

Within the experimental uncertainty, the $\mathbb{S}_{0^+}$ strength is roughly consistent with a constant value if one compares the same $\mathbb{S}_{2^+}$ values and same overlap functions. However, the larger errors bars makes more detailed conclusions impossible.

The present fits show that we cannot extract the $\mathbb{S}_{0^+}$ spectroscopic strength without knowledge of the value for the J^π=2^+ channels. However we can look for consistency with the VMC method as both $\mathbb{S}_{0^+}$ and $\mathbb{S}_{2^+}$ are predicted. The connected small data points in Fig. 7.10(b) show the predicted spectroscopic strength $\mathbb{S}_{0^+}$ obtained from the VMC model. All values are very similar with magnitudes of $\sim$0.526. For the GFMC method only the ^{7}He$_{g.s.}$ result of $\mathbb{S}_{0^+}$=0.532 has been calculated and so this value is plotted as the horizontal

line in Fig. 7.10(a). For comparison the shell-model value of $\mathbb{S}_{0^+}$ is 0.696. In Fig. 7.10(b), the solid data points obtained with the VMC value of $\mathbb{S}_{2^+}$=2 are 30% to 80% larger than VMC predictions. For the GFMC method no value of $\mathbb{S}_{2^+}$ has be predicted yet. To show consistency, the value of $\mathbb{S}_{2^+}$ would have to be small as already the results with $\mathbb{S}_{2^+}$=0 are close to the open data points in Fig. 7.10(a).

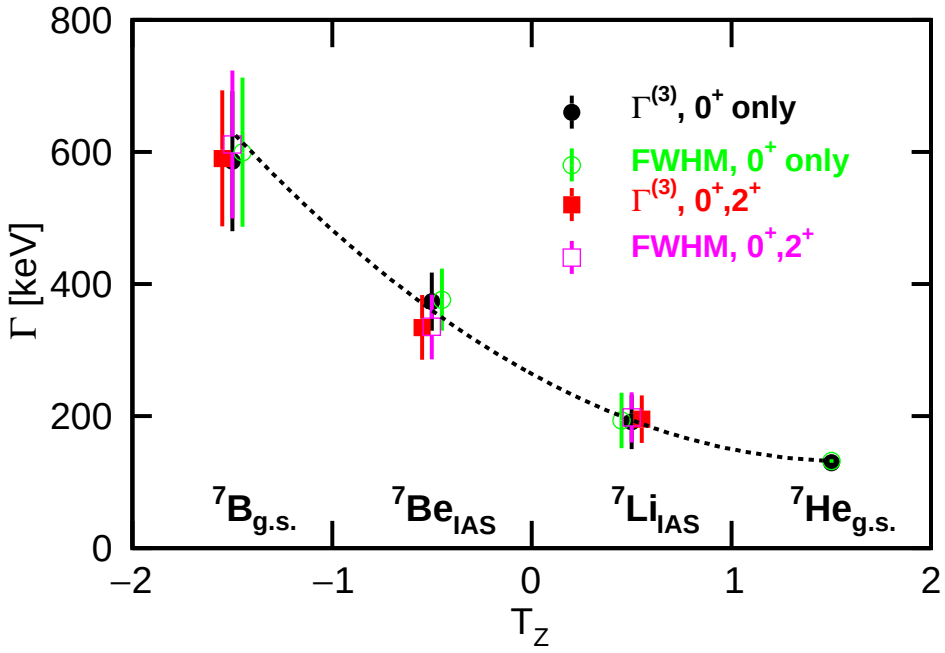

Figure 7.11: (Color Online) Comparison of the width of the $T = 3/2$ resonance for $A = 7$ as a function of T_Z from the FWHM of the R-matrix line shape and extracted from the S-matrix. The contribution of including the $J^\pi = 2^+$ is also shown. The dotted line is a quadratic fit.

The spectroscopic factors constrain the total width of these resonance. Figure 7.11 compares the widths obtained four ways. The decay width can be determined from the FWHM of the fitted intrinsic line shape or from $\Gamma^{(3)}$, the imaginary part of the pole of the S-matrix (see Sec. 7.4). In addition for each of these, we consider the results obtained for the fits with $\mathbb{S}_{2^+}$=0 and 2.0. However, as can be seen from this figure, all ways of determining the width of the resonance yield consistent results. The widths are well fit with a quadratic dependence on T_Z shown as the dotted curve. If a higher-order polynomial was needed in fitting these widths one expects that this would lead to disagreement with the quadratic IMME using the

$E_R^{(3)}$ definition.

7.9 Summary

In this work we have reexamined the $A = 7$, $T = 3/2$ quartet. New measurements of isobaric analog states of ^{7}Be and ^{7}Li, with better statistics and better resolution than previous work, have reduced the uncertainty on their resonance energy by at least a factor of two in both cases. As the intrinsic widths of all four members of this quartet are large, the resonance energy is not a well defined quantity. In order to make a fair comparison we have analyzed all four members with a consistent R-matrix analysis. Regardless of the chosen definition of the resonance energy, with the new measurements for the $|T_Z| = 1/2$ members, the masses are well reproduced by the quadratic form of the isobaric analog mass equation. Furthermore we have extracted the spectroscopic strengths across the multiplet. We find that the extracted spectroscopic factors for decay to the $J^\pi = 0^+$ daughter states are highly dependent upon the assumed strength for configurations associated with the first-excited J^π=2^+ states of these daughters. The latter configurations are bound except for the proton-rich members where they are partially unbound. The strength of both these configurations obtained from the Variational Monte Carlo method were not consistent with our R-matrix analysis of experimental lines shape of the isobaric quartet.

Chapter 8

Assorted States

8.1 ^{9}C

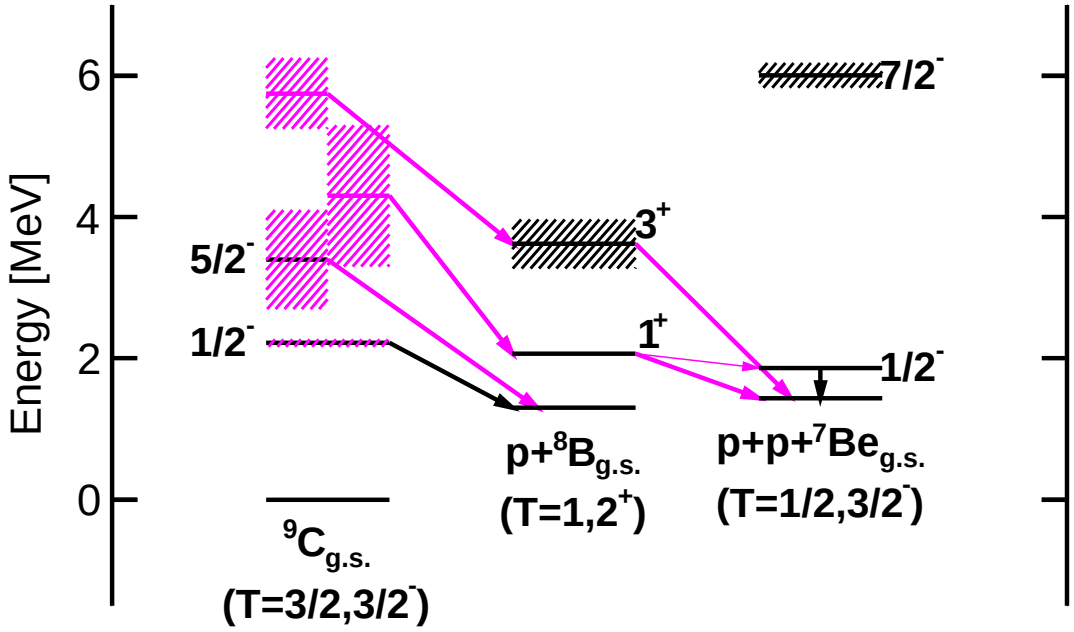

Figure 8.1: Partial level scheme for the proton decay of ^{9}C and ^{8}B. Levels are labeled by their spin and parity (J^{π}) when known. New levels, widths, or decay modes are plotted in magenta.

Excited states of ^{9}C were populated through inelastic scattering of a ^{9}C beam with a ^{9}Be target. A partial level scheme for the one- and two-proton decay of ^{9}C is shown in Fig. 8.1.

Previously known information (energy, width and decay modes) is plotted in black for ^{9}C and the low-lying states in the daughter nuclei. The ground state is the only particle-bound state in ^{9}C, with the first-excited state more than 1 MeV above the proton-decay threshold. The invariant-mass spectrum of ^{9}C from all detected p+^{8}B events is displayed in Fig. 8.2. The two prominent peaks correspond to the known first- and second-excited states with J^π = $1/2^-$ and $5/2^-$ respectively. Both states decay by one-proton emission to the J^π = 2^+ ground state of ^{8}B.

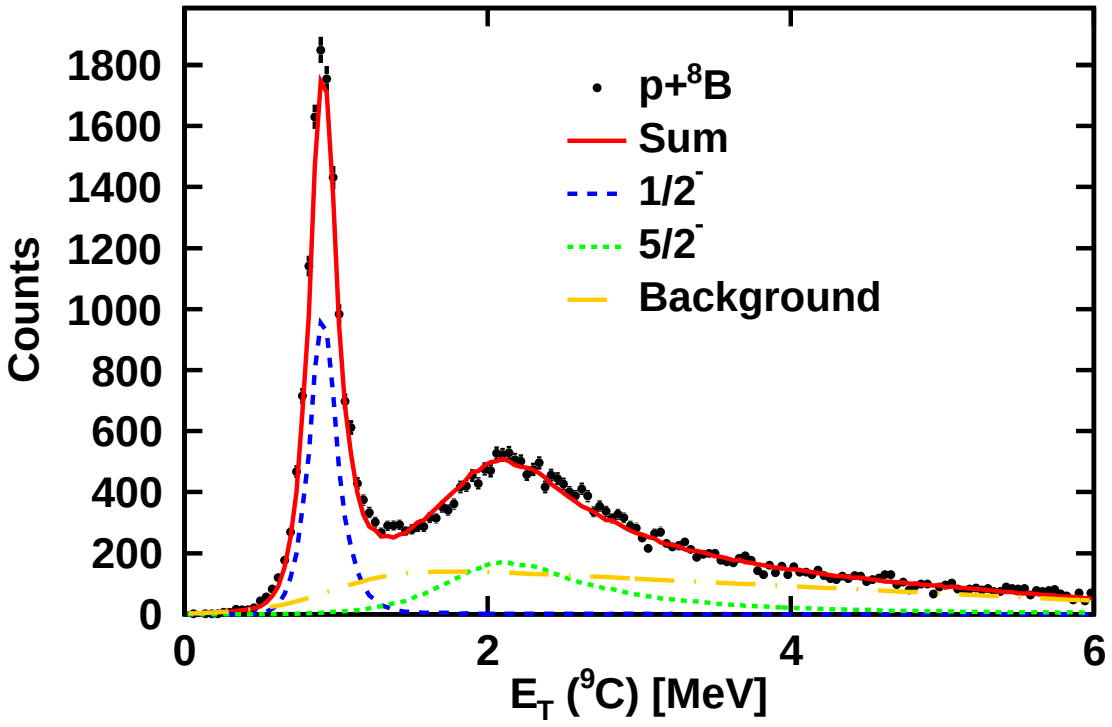

Figure 8.2: Invariant-mass spectrum of ^{9}C from all detected p+^{8}B events.The blue dashed and green dotted lines are R-matrix simulations for the $1/2^-$ and $5/2^-$ states, each curve has been scaled down by a factor of two for clarity. The orange dot-dashed line is one parameteriza0.0tion of the background. The sum of the background and two simulations is plotted as the red solid line.

0. +

In order to extract the level energy and width for each state, the invariant-mass spectrum was fit using the R-matrix, described in Chapter 7. The red solid curve in Fig. 8.2 is the best fit with the excitation energy for the first-excited state fixed at the known value (2.218

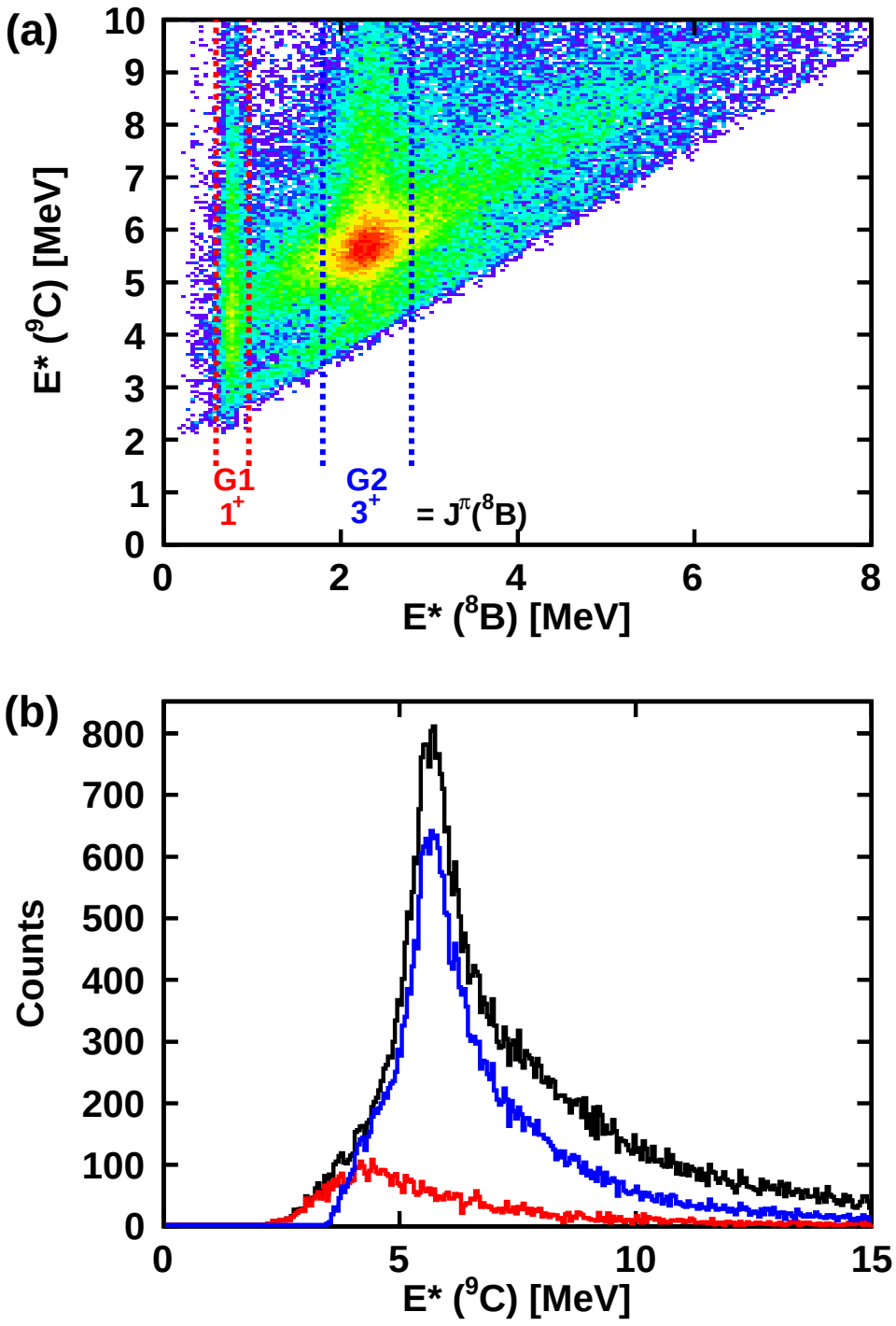

Figure 8.3: (a) Excitation energy spectrum for $2p$+^{7}Be events plotted as a function of the excitation energy for the intermediate (^{8}B) for each p+^{7}Be combination. (b) Excitation energy spectrum for ^{9}C from all detected $2p$+^{7}Be events (black). The red and blue spectra are the excitation energy spectrum for ^{9}C gated on gates G1 and G2, respectively.

(11) MeV [9]) and the energy for the second-excited state extracted from the fit. The fit includes the individual R-matrix simulations of each peak (blue dashed and green dotted lines respectively) as well as a smooth background (yellow dot-dashed line). The background is an inverse Fermi function multiplied with a quadratic to best describe a background with a sharp cutoff, similar to the background chosen for ^{7}B in Chapter 7. The line shapes of the individual peaks are taken from R-matrix line shapes of a given decay energy and width that were input into a Monte Carlo simulation to account for detector resolution and bias. The amplitudes of the line shapes and the parameters for the background were then simultaneously fit for each decay energy and width pair to extract the over-all best fit to the data. The width extracted for the first-excited state is $\Gamma = 52 \pm 11$ keV. The excitation energy of the second-excited state was found to be $E^* = 3.549 \pm 0.020$, with an intrinsic width of $\Gamma = 673 \pm 50$ keV. The extracted width of the first-excited state is much lower than the value of $\Gamma = 100 \pm 20$ keV obtained from (^{3}He,^{6}He) transfer in Ref. [89]. Recent *ab initio* calculations with the Variational Monte Carlo method predict the width to be $\Gamma = 102 \pm 5$ keV [90], which is consistent with the transfer work, but totally inconsistent with our measurement. However more recent results from the Shell Model with the source-term approach (STA) predict a width of $\Gamma_{STA} = 53$ keV, which reproduces our result [91]. The standard approach to the Shell Model also agrees with our result, $\Gamma_{SM} = 58.7$ keV [91].

At $E^* = 1.436$ (18) MeV, ^{9}C becomes unbound with respect to two-proton emission. The black histogram in Fig. 8.3 (b) shows the invariant-mass spectrum from all detected $2p$+^{7}Be events. A wide, asymmetric peak at around 5.5 MeV can be seen. Any excited states of ^{9}C that $2p$ decay will decay sequentially through the excited states of ^{8}B. Therefore we can reconstruct the excitation energy of the ^{8}B intermediate, and determine the decay path through which each state in ^{9}C de-excites, Fig 8.3 (a). Two peaks can be seen, corresponding to the 1^+ and 3^+ excited states in ^{8}B. Gating on these two states, gates G1 and G2, pull out two different peaks from the ^{9}C invariant-mass spectrum. The G1 gate (red histogram) is associated with a state in ^{9}C at 4.40 (2) MeV, decaying through the 1^+ state in ^{8}B, and

the G2 gate (blue histogram) is associated with a state at 5.69 (2) MeV, decaying through the 3^+ state. The 4.40 MeV state was seen previously from (^{3}He,^{6}He) transfer reactions, where they reported only the excitation energy (4.3 MeV) [92]. While no J^π for either state is known, nor are the analogs known in the mirror nucleus ^{9}Li, we can infer that the lower energy state is low spin, and likely $J = 1/2^+$ because it decays predominantly through the 1^+ state and not the 2^+ ground-state in ^{8}B. Similarly the higher energy state is likely high spin, $J \geq 7/2$, because it decays mostly through the 3^+ state.

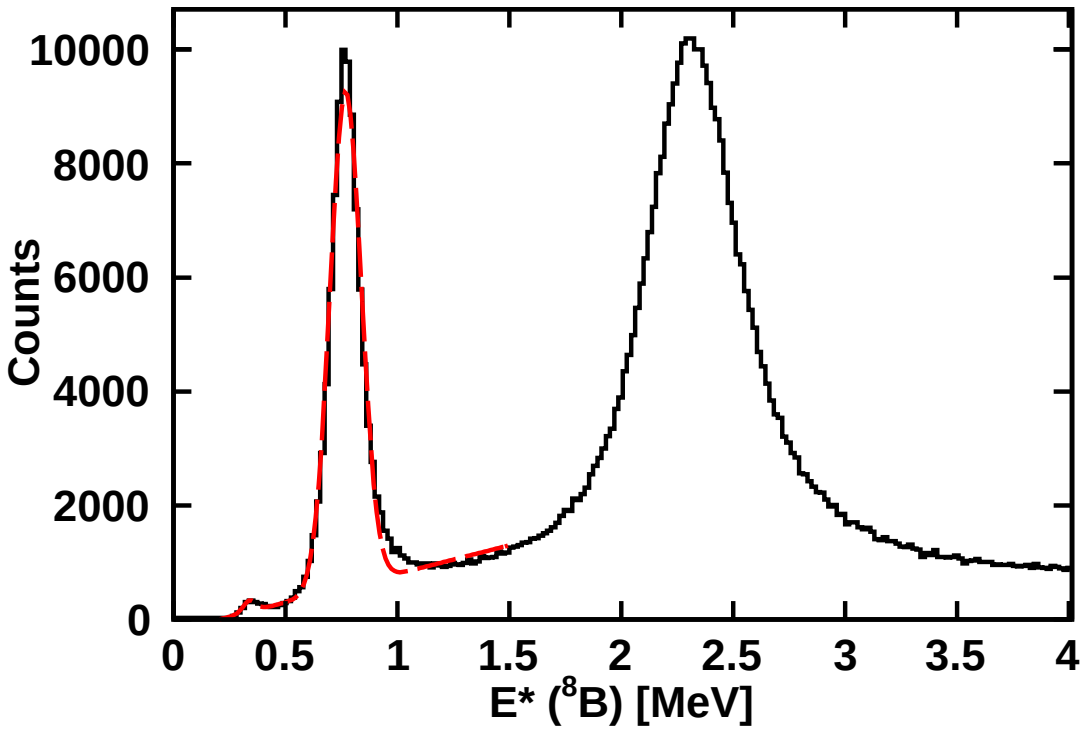

Figure 8.4: Excitation energy spectrum of ^{8}B from all p+^{7}Be events (black solid line). The peaks corresponding to the decay of the 1^+ state are fit with the sum of two Gaussian fits and a linear background (dashed line).

8.2 ^{8}B

The two-proton decay of ^{8}B was discussed previously in Chapter 3, and the one-proton decay to high-lying excited states of ^{7}Be that decay to ^{3}He+α was published previously by

our group [24]. In this section I will discuss the one-proton decay to the particle-bound states of ^{7}Be. A partial level scheme for ^{8}B can be seen in Fig. 8.1. The energy and width of the first two excited states in ^{8}B have been known for a long time [9], however their decay modes were not previously reported. The 1^{+} and 3^{+} levels are both unbound with respect to proton decay to the ground state ($3/2^{-}$) and first-excited state ($1/2^{-}$) of ^{7}Be. The first-excited state of ^{7}Be decays via emission of a 429 keV γ ray to the ground-state. The invariant-mass spectrum for ^{8}B from all p+^{7}Be events can be seen in Fig. 8.4. The two prominent peaks at E^{*} = 0.769 (25) and 2.320 (20) MeV correspond to the first two excited states of ^{8}B. A smaller peak at 0.340 MeV arises from events where we populate the first-excited state in ^{8}B and it decays by one-proton emission to the 429.08 (10) keV first-excited state in ^{7}Be which γ decays. A γ-ray spectrum, gated on this small peak, can be seen in Fig. 8.5. The blue dashed line corresponds to one estimation of the background. The background was generated by gating on events in the $^{9}\mathrm{B} \rightarrow p{+}2\alpha$ channel, which has no bound, excited states that produce γ rays. We can extract a branching ratio for the decay of the 1^{+} state to either the $3/2^{-}$ ground state or $1/2^{-}$ first-excited state in ^{7}Be. By fitting both peaks and extracting the areas, and correcting for the efficiencies of detection, the branching ratio was found to be 1.1 % to the $1/2^{+}$ excited state and 98.9 % to the $3/2^{+}$ ground state of ^{7}Be.

8.3 ^{17}Na

States in ^{17}Na can be populated with a ^{17}Ne beam by charge exchange reactions (exchanging a neutron for a proton) with the target. Prior to this work it was known that ^{17}Na was unbound but its continuum structure had been unexplored. The decay-energy spectrum for $^{17}\mathrm{Na} \rightarrow 3p{+}^{14}\mathrm{O}$ is shown in Fig. 8.6. There is a peak in the spectrum located at E_T = 4.85 (6) MeV that sits on top of a large background. This background is largely due to ^{15}O nuclei which are misidentified as ^{14}O. However no strong resonances were detected in the $3p$+^{15}O

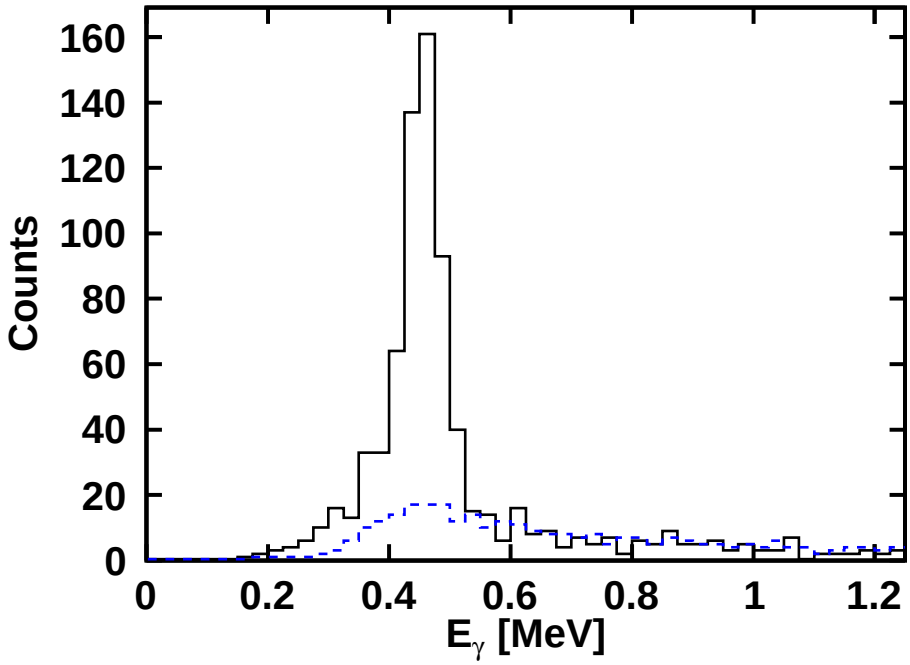

Figure 8.5: The black solid histogram is the γ-ray energy spectrum gated on the small peak in the ^{8}B invariant-mass spectrum. The blue dashed histogram is a CAESAR γ-ray background.

decay channel, so the background in this spectrum is featureless. The mirror nucleus, ^{17}C, has a $3/2^+$ ground state, and $1/2^+$ and $5/2^+$ excited states at 210 and 331 keV respectively [93]. For a $3p$ decay at 4.85 MeV, Monte Carlo simulations of the device resolution predict the full width at half maximum (FWHM) of the reconstructed energy to be 540 keV. The FWHM of the detected peak is 1150 keV. Therefore this peak is either a wide state, or some mixture of all three states (including the ground state), with the average $< E_T > = 4.85$ (6) MeV.

From the average decay energy, an upper limit for the mass excess of ^{17}Na is $\Delta^{17}Na \leq$ 34.72 (6) MeV (blue arrow in Fig. 8.6). The mass excess predicted from systematics is $\Delta^{17}Na = 35.346$ (23) MeV (red arrow in Fig. 8.6) [94]. The measured upper limit on the mass excess is lower than the systematics by $\sim$ 600 keV, however this may be due to a Thomas-Ehrman shift of the $1/2^+$ excited state, which would bring its energy down relative to its position in ^{17}C. Shell model calculations suggest that the $1/2^+$ state has two of the

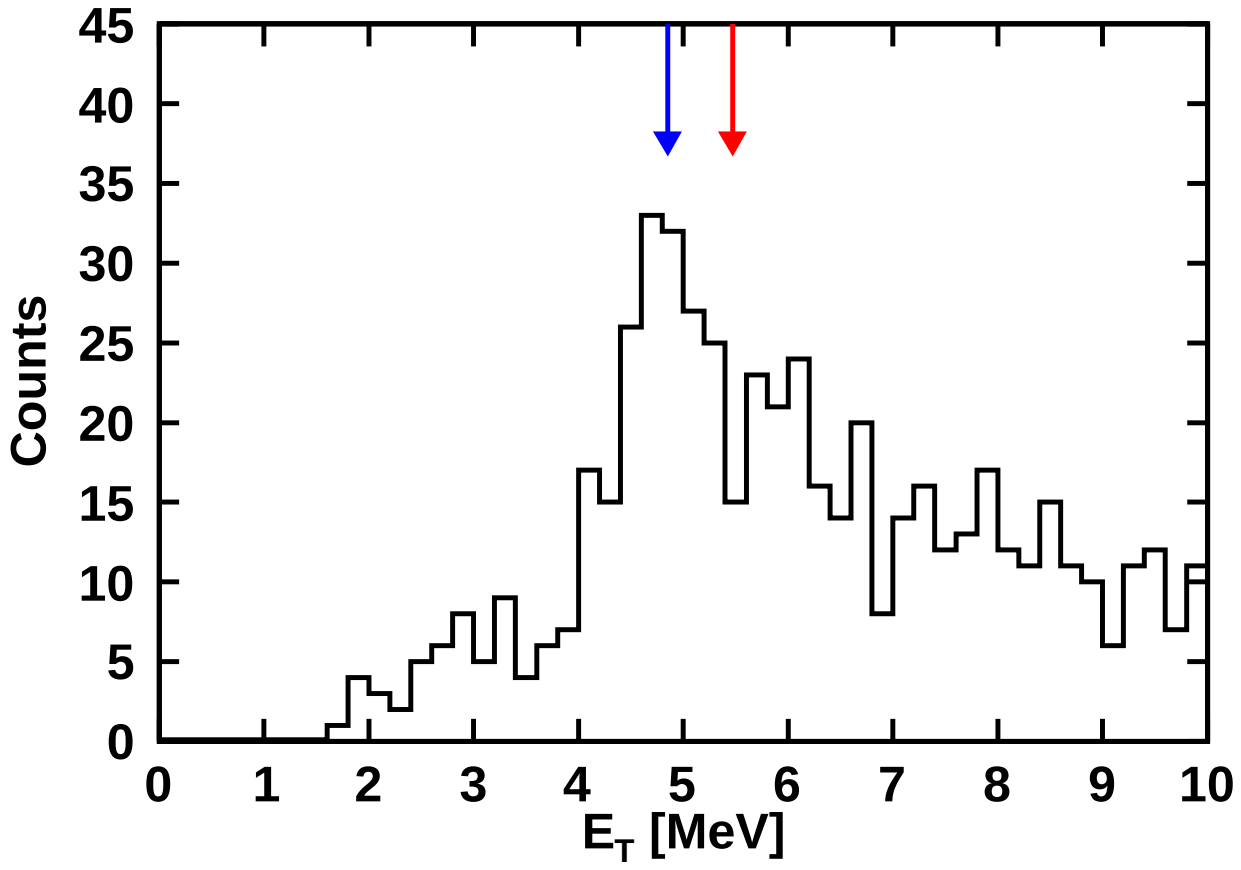

Figure 8.6: Decay energy spectrum of ^{17}Na from all detected $3p$+^{14}O events. The blue arrow marks the average energy of the peak, and the red arrow marks the ground-state energy predicted from mass systematics.

valence $d_{5/2}$ nucleons coupled to 0^+ and the third valence nucleon in the second $s_{1/2}$ orbit [95]. If that third nucleon is a proton, the radial wavefunction will be expanded relative to the wavefunction for a neutron in that orbit, and the energy of the state will be lower. It is possible that the $s_{1/2}$ orbit has moved far enough down in energy that this peak is completely the $1/2^+$ state, and therefore the ground-state is $1/2^+$ instead of being $3/2^+$ as it is in the mirror nucleus. To provide further details, a higher statistics experiment with better resolution is needed.

8.4 ^{17}Ne

With a ^{9}C beam we were able to populate 1- and 2-proton decaying states in ^{9}C through inelastic excitation, Sec. 8.1. With a ^{17}Ne beam we are also able to populate 2-proton decaying excited states in ^{17}Ne through inelastic excitation. The continuum states of ^{17}Ne up to $E^* = 6.5$ MeV were studied almost 20 years ago through the ^{20}Ne(^{3}He,^{6}He)^{17}Ne reaction [96]. They were able to extract energies, spins, and parities for a large number of excited state, but no information about how they decay. In this section we will re-examine the $J^\pi = 5/2^-$ second-excited state in ^{17}Ne.

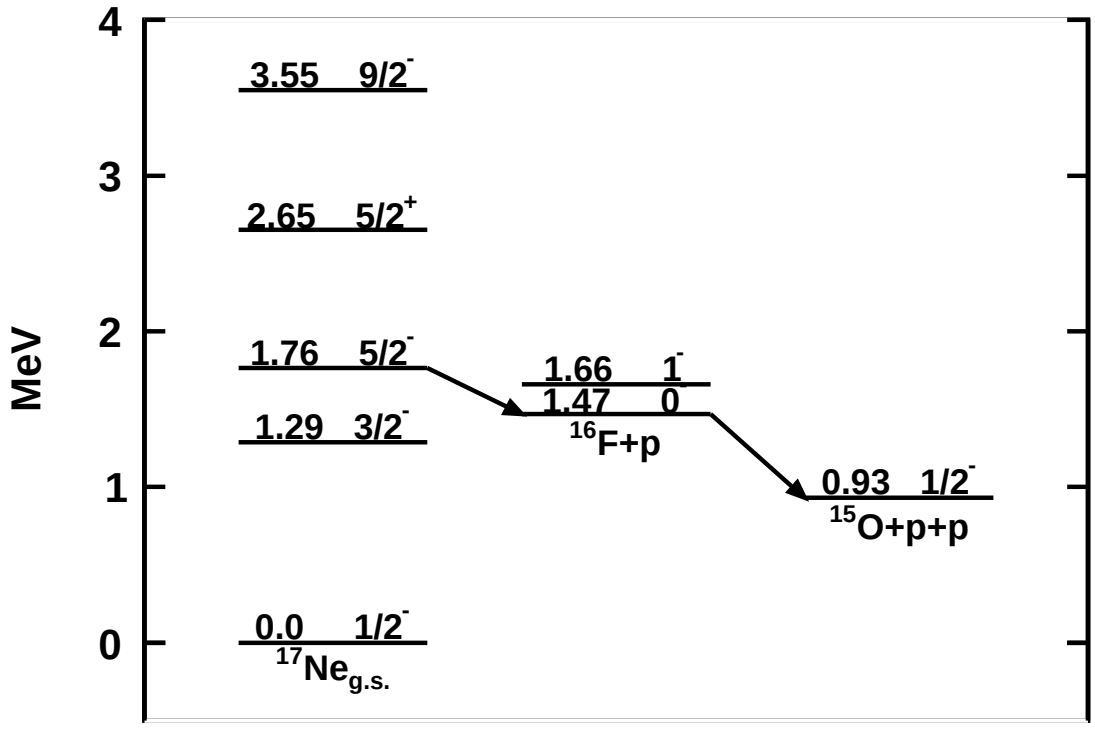

Figure 8.7: Partial level scheme for the $2p$ decay of ^{17}Ne. States are labeled by their spin, parity, and energy relative to the ground state of ^{17}Ne.

Figure 8.7 shows a partial level scheme for ^{17}Ne. While the $3/2^-$ first-excited state is above the $2p$ threshold, it has been shown to decay exclusively by γ-ray emission to the ground-state through the non-observation of the $2p$ decay [97]. They measured the $2p$ decay branch of the $5/2^-$ state, and concluded that based on the lifetimes from a simple barrier

penetration calculation all of the strength had to go through the 0^- ($\tau = 1.4$ fs) intermediate and not the 1^- ($\tau = 300$ ps). This is reasonable given the decay energy to the 1^- is only 100 keV and the angular momentum in both possible decays is $\ell = 2$. From the momentum correlations in the Jacobi coordinate system, see Chapter 1, we can distinguish between these two possible decay paths directly.

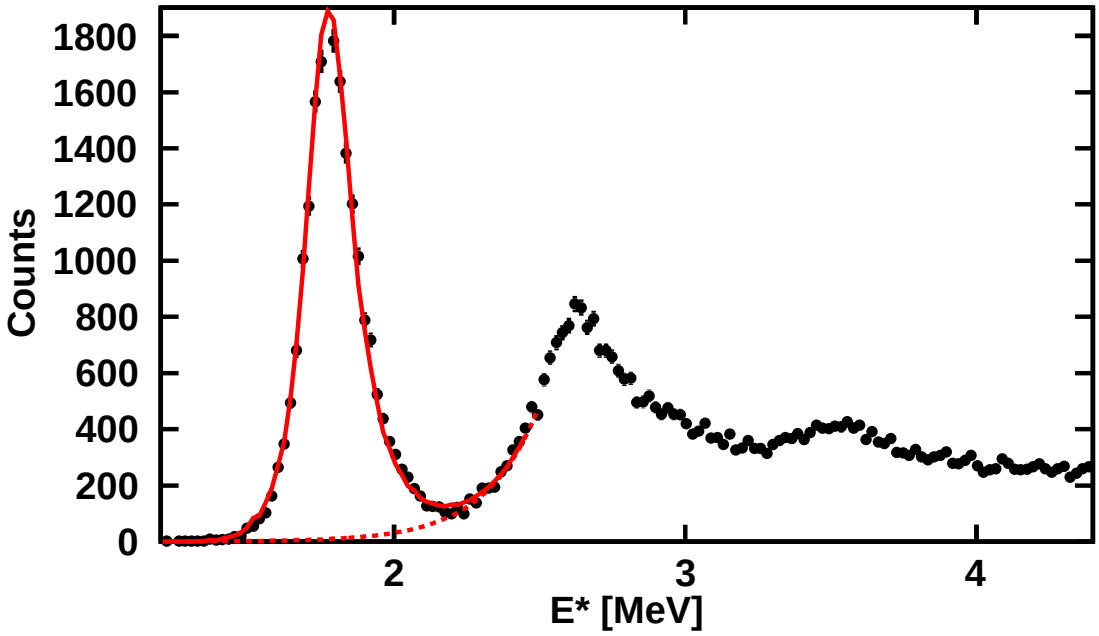

Figure 8.8: Excitation energy spectrum of ^{17}Ne from all detected $2p$+^{15}O events. The solid red curve is an R-matrix fit to the 1.7 MeV ($J^\pi = 5/2^-$) second-excited state of ^{17}Ne with a quadratic background (red dashed line). Peaks corresponding to the $J^\pi = 5/2^+$ and $9/2^-$ states are seen at higher energy.

The invariant-mass spectrum for ^{17}Ne, Fig. 8.8, shows three peaks corresponding to $E^* =$ 1.764 (12), 2.651 (12) and 3.548 (20) MeV states with $J^\pi = 5/2^-$, $5/2^+$ and $9/2^-$ respectively, all seen in [96]. No evidence for the 1.908 (15) MeV $1/2^+$ state is seen. An R-matrix fit of the $5/2^-$, filtered by detector acceptance and resolution via Monte Carlo simulation, was performed with a simple quadratic form assumed for the background contribution. The extracted excitation energy is $E^* = 1.77$ (2) MeV which is consistent with the result from transfer [96]. The lifetime of this state predicted from [97] is $\tau = 1.4$ fs, which corresponds to an intrinsic width of 0.23 eV, far smaller than our detector resolution. Indeed the R-matrix

fit of this state with no intrinsic width is consistent with zero width and thus the lifetime quoted above.

In the Jacobi Y energy variable (E_{core-p}/E_T), the expected signature of a sequential decay is a double peaked spectrum, with one peak corresponding to the decay energy in each step. Figure 8.9 (a) shows the Jacobi Y energy distribution for the $2p$ decay of this state. It has two peaks, one at ~ 0.35 and one at ~ 0.65, which is roughly consistent with the decay through the 0^- intermediate. The energy-angular correlations (Fig. 8.9 (b)) in the Jacobi Y system for this decay exhibit the double-ridge feature seen for sequential decay. Two R-matrix simulations were performed for the decay either through the 0^- or the 1^- intermediates, with the energy-angular correlation spectra in Fig. 8.9 (c) and (d) respectively. Their 1-D energy projections are plotted as the red solid and blue dashed curves in Fig. 8.9 (a). The E_{core-p}/E_T distribution is consistent with the simulation through the 0^-, which confirms the inference of [97].

The most surprising result is the outcome of the simulation of the decay through the 1^-. In that case the decay energy of the two steps are 100 keV and 730 keV, with $\Gamma < 40$ keV for the 1^-. The naive expectation would be for there to be two peaks, one at ~ 0.12 and one at ~ 0.88, however only a single peak at 0.5 is seen. To understand why this is the case, one needs to look at the R-matrix line shape input into the Monte Carlo simulation. Figure 8.10 shows the line shapes as a function of the energy of the first proton for the decay through the (a) 0^- and (b) 1^-. The black curves are the line shapes of the second proton (p_2) as a function of the energy of the first proton (p_1), which are peaked at the energy of the $p+^{16}$F resonance. The red curves are the barrier penetration factors ($P_\ell(p_1)$) for the first protons, which fall off sharply to zero with decreasing energy. The product of these two functions is shown in blue. For the 0^- intermediate the peak of the resonance falls in an energy region where the barrier penetration factor isn't changing that rapidly, and therefore the line shape in the resonance region is not altered significant. However for the 1^- the resonance is in a region where the barrier penetration factor is changing quite rapidly. The

result is the peak of the resonance is highly suppressed relative to the tail, and the decay largely happens through the long tail of the resonance line shape. This is a common feature for near-thresholds decays, often called a "ghost peak", and has been discussed in more detail for the α decay of ^{8}Be [98]. The exact shape depends on the assumed width of the 1^- state, in this case the value of $\Gamma = 40$ keV was taken. If this was significantly more narrow, then the E_{core-p} distribution would again have two peaks.

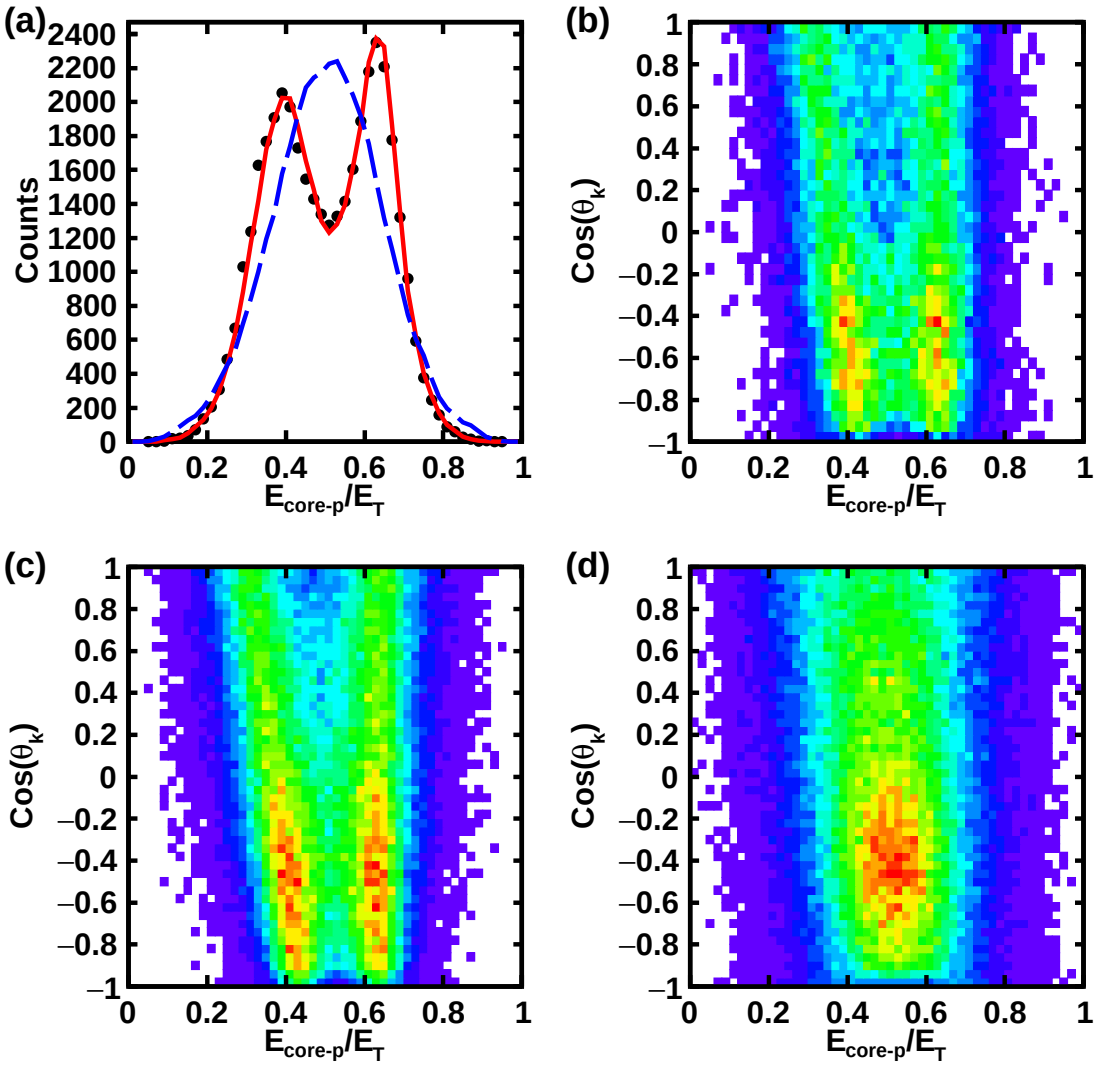

Figure 8.9: (a) Jacobi Y energy variable for the $2p$ decay of ^{17}Ne second-excited state. Red solid (blue dashed) curves are Monte Carlo simulations for the decay through the ground state (first-excited state) of the ^{16}F intermediate. (b) Jacobi Y energy-angular correlations for ^{17}Ne second-excited state. (c) and (d) are Monte Carlo predictions for the decay through the ground and first-excited state of ^{16}F respectively.

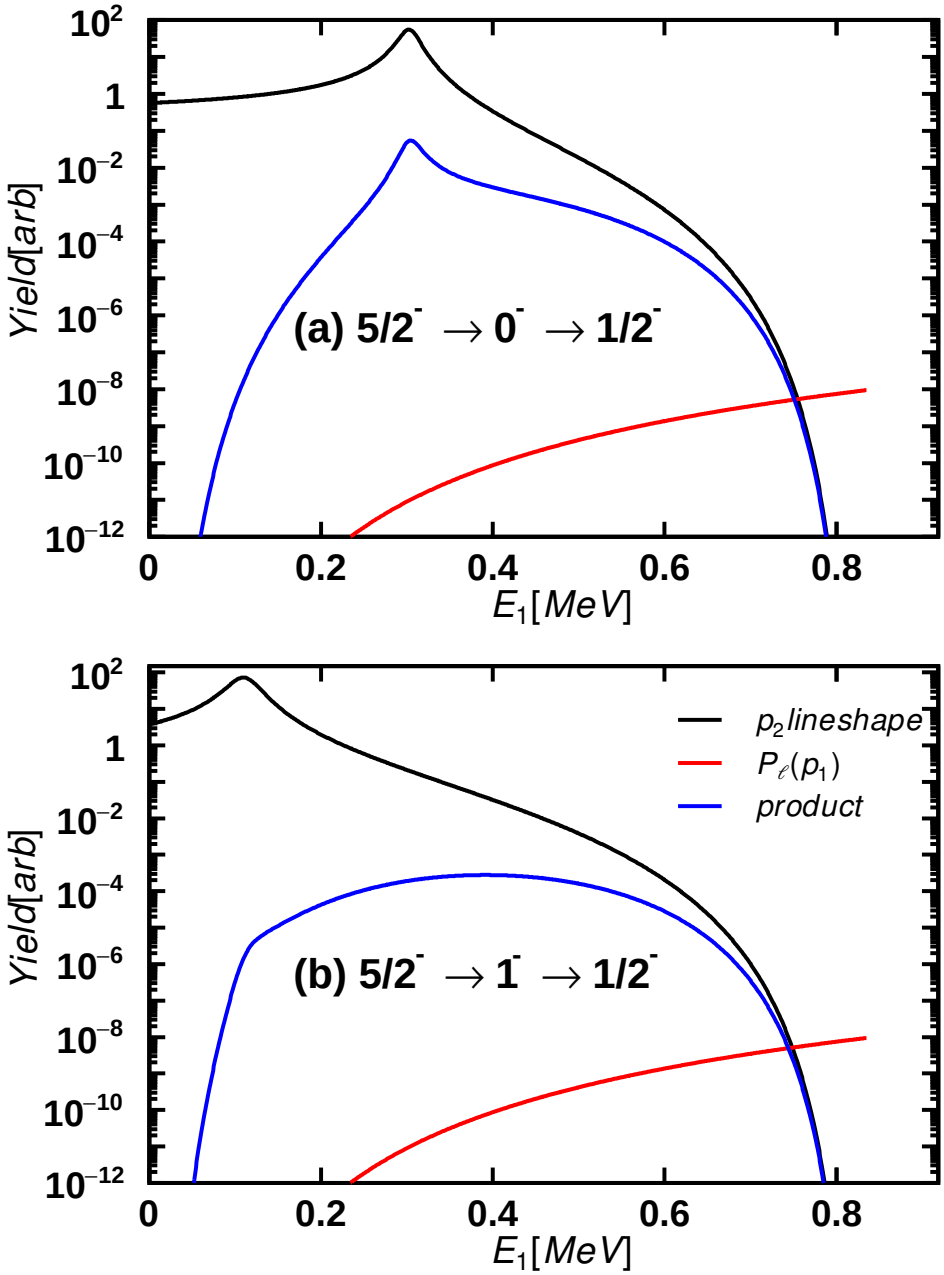

Figure 8.10: R-matrix simulations for the $2p$ decay of ^{17}Ne second-excited state through ^{16}F (a) ground-state and (b) first-excited state. The line shape for the second proton p_2 (black), the barrier penetration factor for the first proton p_1, and their product (blue) are displayed for both decay paths.

Chapter 9

Summary

I have used the invariant-mass method to study the proton-decaying nuclei labeled in Fig. 9.1. In this method, the decay energy and intrinsic width can be determined with high precision for nuclear levels within a few MeV of their decay threshold and have lifetimes shorter than 10^{-20} s ($\Gamma \geq 10$ keV). For longer-lived nuclei, if the lifetime is not longer than a nanoseconds, the decay energy can still be determined, however only an upper limit on the intrinsic width can be measured. By studying these unbound, light nuclei we can better understand their role in the production of elements in our universe.

A summary of the information measured in this work can be found in Table 9.1. As all decay products are measured, this method is ideal for distinguishing the decay mode of a given nuclear level. Both $^{8}\mathrm{B}_{IAS}$ and $^{16}\mathrm{Ne}_{gs}$ were found to decay by direct $2p$ emission. The $^{8}\mathrm{B}_{IAS}$ was the first case proven to directly decay by $2p$ emission to the IAS in the daughter because all other energy-allowed decay modes are forbidden by isospin. In ^{16}Ne, the ground state decayed by $2p$ to the ground state of ^{14}O, but the first-excited state was found to decay by both direct and sequential $2p$, displaying interference effects between the two decay paths. The IAS in ^{16}F was believed to $2p$ decay to the IAS in ^{14}N, analogous to the decay of $^{8}\mathrm{B}_{IAS}$, however it appears that the larger Coulomb barrier in ^{16}F highly suppresses this decay mode. The dominant decay mode for $^{16}\mathrm{F}_{IAS}$ remains unknown. For the $A = 7$ isobar,

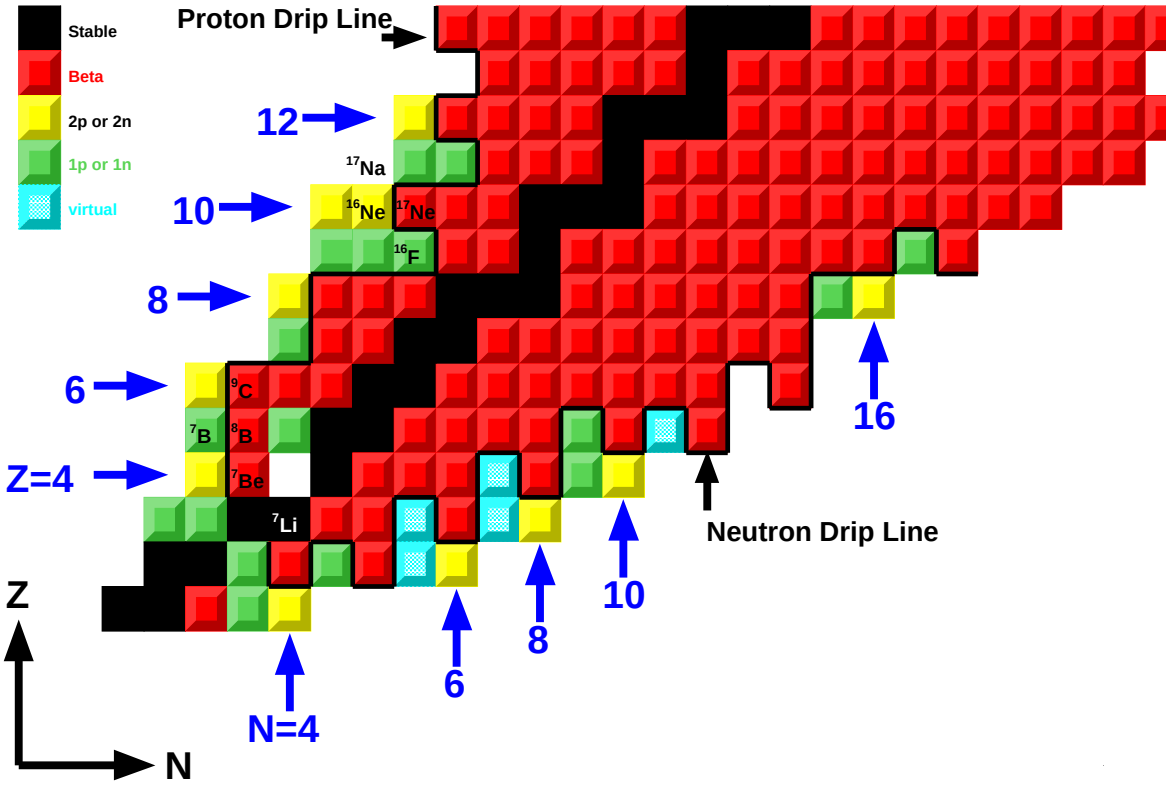

Figure 9.1: Chart of nuclides. Proton number increases towards the top of the figure, and neutron number increases towards the right. Stable nuclei are shown as black squares, and the radioactive nuclei are shown as colored squares, indicating their dominate mode of decay. Nuclei studied in this work are labeled.

new measurements of the masses of three of the four nuclei by the invariant-mass method has nearly eliminated the need for a cubic term in the Isobaric Mass Multiplet Equation. To provide further information on this isobar, new experiments would require more than 1 order of magnitude better resolution to provide constraints tight enough to address the need for a small cubic term as predicted in *ab initio* calculations. We have made the first report on the decay of ^{17}Na, a collection of nucleons 3 neutrons deficient of the lightest, particle-bound sodium isotope.

While this work was focused entirely on nuclei that decay by charged-particle emission, this method has also be used to studying 1- and 2-neutron decay. The field now turns its attention to the Facility for Rare Isotope Beams (FRIB), which will provide more exotic and higher intensity radioactive ion beams than ever before produced on earth. While in this new era experimental advances will be required to improve resolution and efficiency, the invariant-mass method will continue to be a major tool in the study of the most exotic nuclei. Progress will continue to be made with the invariant-mass method on both sides of the nuclear chart.

Table 9.1: New spectroscopic information for nuclear levels discussed in this work. Excitation energies, intrinsic widths and decay modes are provided when measured. For nuclear levels with multiple decay modes, branching ratios are given as intensities out of 100 relative to the dominant decay mode. For ground-state decays, decay energy is given in place of excitation energy.

Nucleus	Excitation Energy (MeV)	Width (keV)	Decay Mode
$^{7}\mathrm{Li}_{IAS}$	11.267 (15)	191 (41)	$^{7}\mathrm{Li}_{IAS} \rightarrow p{+}^{6}\mathrm{He}$, I = 100
			$^{7}\mathrm{Li}_{IAS} \rightarrow n{+}(^{6}\mathrm{Li}_{IAS}) \rightarrow n{+}(^{6}\mathrm{Li}_{g.s.}{+}\gamma)$, I = 88.7
$^{7}\mathrm{Be}_{IAS}$	10.989 (15)	376 (47)	$^{7}\mathrm{Be}_{IAS} \rightarrow p{+}(^{6}\mathrm{Li}_{IAS}) \rightarrow p{+}(^{6}\mathrm{Li}_{g.s.}{+}\gamma)$, I = 100
			$^{7}\mathrm{Be}_{IAS} \rightarrow n{+}^{6}\mathrm{Be}$, I = 9.9
$^{7}\mathrm{B}_{g.s.}$	0.0 [E_r = 2.036 (26)]	599 (113)	$^{7}\mathrm{B}_{g.s.} \rightarrow p{+}(^{6}\mathrm{Be}_{g.s.}) \rightarrow p{+}(2p{+}\alpha)$
$^{8}\mathrm{B}_{1^+}$	0.769 (25)		$^{8}\mathrm{B}_{1^+} \rightarrow p{+}^{7}\mathrm{Be}_{g.s.}$, I = 100
			$^{8}\mathrm{B}_{1^+} \rightarrow p{+}^{7}\mathrm{Be}_{1/2^-}$, I = 1.1
$^{8}\mathrm{B}_{3^+}$	2.320 (20)		$^{8}\mathrm{B}_{1^+} \rightarrow p{+}^{7}\mathrm{Be}_{g.s.}$
$^{8}\mathrm{B}_{IAS}$	10.614 (20)	<60	$^{8}\mathrm{B}_{IAS} \rightarrow 2p{+}(^{6}\mathrm{Li}_{IAS}) \rightarrow 2p{+}(^{6}\mathrm{Li}_{g.s.}{+}\gamma)$, I = 100
			$^{8}\mathrm{B}_{IAS} \rightarrow 2p{+}(^{6}\mathrm{Li}_{3^+}) \rightarrow 2p{+}(d{+}\alpha)$, I = 10
			$^{8}\mathrm{B}_{IAS} \rightarrow 2p{+}^{6}\mathrm{Li}_{g.s.}$, I = 11
			$^{8}\mathrm{B}_{IAS} \rightarrow p{+}^{7}\mathrm{Be}_{g.s.}$, I $\leq$ 7.5
$^{9}\mathrm{C}_{1/2^-}$	2.218 (11)	52 (11)	$^{9}\mathrm{C}_{1/2^-} \rightarrow p{+}^{8}\mathrm{B}$
$^{9}\mathrm{C}_{5/2^-}$	3.549 (20)	673 (50)	$^{9}\mathrm{C}_{5/2^-} \rightarrow p{+}^{8}\mathrm{B}$
$^{9}\mathrm{C}$	4.40 (2)		$^{9}\mathrm{C} \rightarrow p{+}(^{8}\mathrm{B}_{1^+}) \rightarrow p{+}(p{+}^{7}\mathrm{Be})$
$^{9}\mathrm{C}$	5.69 (2)		$^{9}\mathrm{C} \rightarrow p{+}(^{8}\mathrm{B}_{3^+}) \rightarrow p{+}(p{+}^{7}\mathrm{Be})$
$^{16}\mathrm{F}$	7.67 (2)		$^{16}\mathrm{F} \rightarrow 2p{+}^{14}\mathrm{N}^{g.s.}$
$^{16}\mathrm{F}$	10.26 (2)		$^{16}\mathrm{F} \rightarrow 2p{+}^{14}\mathrm{N}^{g.s.}$
$^{16}\mathrm{Ne}_{g.s.}$	0.0 [E_r = 1.466 (20)]	<80	$^{16}\mathrm{Ne}_{g.s.} \rightarrow 2p{+}^{14}\mathrm{O}_{g.s.}$
$^{16}\mathrm{Ne}_{2^+}$	1.69 (2)	150 (50)	$^{16}\mathrm{Ne}_{2^+} \rightarrow 2p{+}^{14}\mathrm{O}_{g.s.}$
			$^{16}\mathrm{Ne}_{2^+} \rightarrow p{+}(^{15}\mathrm{F}_{g.s.}) \rightarrow p{+}(p{+}^{14}\mathrm{O}_{g.s.})$
$^{16}\mathrm{Ne}_{2^+}$	7.60 (4)		Seen in the $2p{+}^{14}$O channel, decay type unknown
$^{16}\mathrm{Ne}$	8.37 (10)	320 (100)	Seen in the $3p{+}^{13}$N channel, likely through $^{14}\mathrm{O}_{2^+}$
$^{16}\mathrm{Ne}$	10.76 (20)	510 (230)	Seen in the $3p{+}^{13}$N channel, likely through $^{14}\mathrm{O}_{2^+}$
$^{17}\mathrm{Ne}_{5/2^-}$	1.764 (12)		$^{17}\mathrm{Ne}_{5/2^-} \rightarrow p{+}(^{16}\mathrm{F}_{g.s.}) \rightarrow p{+}(p{+}^{15}\mathrm{O}_{g.s.})$
$^{17}\mathrm{Ne}_{5/2^+}$	2.651 (12)		Seen in the $2p{+}^{15}$O channel, decay type unknown
$^{17}\mathrm{Ne}_{9/2^-}$	3.548 (20)		Seen in the $2p{+}^{15}$O channel, decay type unknown
$^{17}\mathrm{Na}$	0.0 [$E_r \leq$ 4.85 (6)]		Seen in the $3p{+}^{14}$O, decay type unknown

Bibliography

[1] TUNL Nuclear Data Evaluation Project, "Energy Level Diagram, A=7".

[2] M. Pfützner, M. Karny, L. V. Grigorenko, and K. Riisager, "Radioactive decays at limits of nuclear stability," *Rev. Mod. Phys.*, vol. 84, pp. 567–619, 2012.

[3] L. V. Grigorenko, T. D. Wiser, K. Mercurio, R. J. Charity, R. Shane, L. G. Sobotka, J. M. Elson, A. H. Wuosmaa, A. Banu, M. McCleskey, L. Trache, R. E. Tribble, and M. V. Zhukov, "Three-body decay of ^{6}Be," *Phys. Rev. C*, vol. 80, p. 034602, 2009.

[4] D. Weisshaar, A. Gade, T. Glasmacher, G. Grinyer, D. Bazin, P. Adrich, T. Baugher, J. Cook, C. Diget, S. McDaniel, A. Ratkiewicz, K. Siwek, and K. Walsh, "CAESAR—A high-efficiency CsI(Na) scintillator array for in-beam spectroscopy with fast rare-isotope beams," *Nuclear Instruments and Methods in Physics Research Section A: Accelerators, Spectrometers, Detectors and Associated Equipment*, vol. 624, no. 3, pp. 615 – 623, 2010.

[5] K. W. Brown, R. J. Charity, L. G. Sobotka, Z. Chajecki, L. V. Grigorenko, I. A. Egorova, Y. L. Parfenova, M. V. Zhukov, S. Bedoor, W. W. Buhro, J. M. Elson, W. G. Lynch, J. Manfredi, D. G. McNeel, W. Reviol, R. Shane, R. H. Showalter, M. B. Tsang, J. R. Winkelbauer, and A. H. Wuosmaa, "Observation of long-range three-body coulomb effects in the decay of ^{16}Ne," *Phys. Rev. Lett.*, vol. 113, p. 232501, 2014.

[6] I. Brida, S. C. Pieper, and R. B. Wiringa, "Quantum Monte Carlo calculations of spectroscopic overlaps in A $\leqslant$ 7 nuclei," *Phys. Rev. C*, vol. 84, p. 024319, 2011.

[7] Y. Aksyutina, H. Johansson, T. Aumann, K. Boretzky, M. Borge, A. Chatillon, L. Chulkov, D. Cortina-Gil, U. D. Pramanik, H. Emling, C. Forssn, H. Fynbo, H. Geissel, G. Ickert, B. Jonson, R. Kulessa, C. Langer, M. Lantz, T. LeBleis, A. Lindahl, K. Mahata, M. Meister, G. Mnzenberg, T. Nilsson, G. Nyman, R. Palit, S. Paschalis, W. Prokopowicz, R. Reifarth, A. Richter, K. Riisager, G. Schrieder, H. Simon, K. Smmerer, O. Tengblad, H. Weick, and M. Zhukov, "Properties of the ^{7}He ground state from ^{8}He neutron knockout," *Physics Letters B*, vol. 679, no. 3, pp. 191 – 196, 2009.

[8] Z. Cao, Y. Ye, J. Xiao, L. Lv, D. Jiang, T. Zheng, H. Hua, Z. Li, X. Li, Y. Ge, J. Lou, R. Qiao, Q. Li, H. You, R. Chen, D. Pang, H. Sakurai, H. Otsu, M. Nishimura, S. Sakaguchi, H. Baba, Y. Togano, K. Yoneda, C. Li, S. Wang, H. Wang, K. Li, T. Nakamura, Y. Nakayama, Y. Kondo, S. Deguchi, Y. Satou, and K. Tshoo, "Recoil proton tagged knockout reaction for ^{8}He," *Physics Letters B*, vol. 707, no. 1, pp. 46 – 51, 2012.

[9] Evaluated Nuclear Structure Data File (ENSDF), http://www.nndc.bnl.gov/ensdf/.

[10] J. Carlson, S. Gandolfi, F. Pederiva, S. C. Pieper, R. Schiavilla, K. E. Schmidt, and R. B. Wiringa, "Quantum monte carlo methods for nuclear physics," *Rev. Mod. Phys.*, vol. 87, pp. 1067–1118, 2015.

[11] S. Hofmann, W. Reisdorf, G. Münzenberg, F. P. Heßberger, J. R. H. Schneider, and P. Armbruster, "Proton radioactivity of ^{151}Lu," *Zeitschrift für Physik A Atoms and Nuclei*, vol. 305, no. 2, pp. 111–123, 1982.

[12] V. Goldansky, "Two-proton radioactivity," *Nuclear Physics*, vol. 27, no. 4, pp. 648 – 664, 1961.

[13] D. F. Geesaman, R. L. McGrath, P. M. S. Lesser, P. P. Urone, and B. VerWest, "Particle decay of ^{6}Be," *Phys. Rev. C*, vol. 15, pp. 1835–1838, 1977.

[14] R. J. Charity, J. M. Elson, J. Manfredi, R. Shane, L. G. Sobotka, Z. Chajecki, D. Coupland, H. Iwasaki, M. Kilburn, J. Lee, W. G. Lynch, A. Sanetullaev, M. B. Tsang,

J. Winkelbauer, M. Youngs, S. T. Marley, D. V. Shetty, A. H. Wuosmaa, T. K. Ghosh, and M. E. Howard, "$2p$-$2p$ decay of ^{8}C and isospin-allowed $2p$ decay of the isobaric-analog state in ^{8}B," *Phys. Rev. C*, vol. 82, p. 041304, 2010.

[15] G. R. Burleson, G. S. Blanpied, G. H. Daw, A. J. Viescas, C. L. Morris, H. A. Thiessen, S. J. Greene, W. J. Braithwaite, W. B. Cottingame, D. B. Holtkamp, I. B. Moore, and C. F. Moore, "Isospin quintets in the 1p and s-d shells," *Phys. Rev. C*, vol. 22, pp. 1180–1183, 1980.

[16] K. Föhl, R. Bilger, H. Clement, J. Gräter, R. Meier, J. Pätzold, D. Schapler, G. J. Wagner, O. Wilhelm, W. Kluge, R. Wieser, M. Schepkin, R. Abela, F. Foroughi, and D. Renker, "Pionic double charge exchange on N=Z doubly closed shell nuclei," *Phys. Rev. Lett.*, vol. 79, pp. 3849–3852, 1997.

[17] G. J. KeKelis, M. S. Zisman, D. K. Scott, R. Jahn, D. J. Vieira, J. Cerny, and F. Ajzenberg-Selove, "Masses of the unbound nuclei ^{16}Ne, ^{15}F, and ^{12}O," *Phys. Rev. C*, vol. 17, pp. 1929–1938, 1978.

[18] C. J. Woodward, R. E. Tribble, and D. M. Tanner, "Mass of ^{16}Ne," *Phys. Rev. C*, vol. 27, pp. 27–30, 1983.

[19] M. Wallace, M. Famiano, M.-J. van Goethem, A. Rogers, W. Lynch, J. Clifford, F. Delaunay, J. Lee, S. Labostov, M. Mocko, L. Morris, A. Moroni, B. Nett, D. Oostdyk, R. Krishnasamy, M. Tsang, R. de Souza, S. Hudan, L. Sobotka, R. Charity, J. Elson, and G. Engel, "The high resolution array (HiRA) for rare isotope beam experiments," *Nuclear Instruments and Methods in Physics Research Section A: Accelerators, Spectrometers, Detectors and Associated Equipment*, vol. 583, no. 23, pp. 302 – 312, 2007.

[20] G. L. Engel, M. Sadasivam, M. Nethi, J. M. Elson, L. G. Sobotka, and R. J. Charity, "A multi-channel integrated circuit for use in low- and intermediate-energy nuclear physics—HINP16C," *Nuclear Instruments and Methods in Physics Research Section*

A: Accelerators, Spectrometers, Detectors and Associated Equipment, vol. 573, no. 3, pp. 418 – 426, 2007.

[21] http://www.micronsemiconductor.co.uk/.

[22] O. Bochkarev, L. Chulkov, A. Korsheninniicov, E. Kuz'min, I. Mukha, and G. Yankov, "Democratic decay of ^{6}Be states," *Nuclear Physics A*, vol. 505, no. 2, pp. 215 – 240, 1989.

[23] M. F. Jager, R. J. Charity, J. M. Elson, J. Manfredi, M. H. Mahzoon, L. G. Sobotka, M. McCleskey, R. G. Pizzone, B. T. Roeder, A. Spiridon, E. Simmons, L. Trache, and M. Kurokawa, "Two-proton decay of ^{12}O and its isobaric analog state in ^{12}N," *Phys. Rev. C*, vol. 86, p. 011304, 2012.

[24] R. J. Charity, J. M. Elson, J. Manfredi, R. Shane, L. G. Sobotka, B. A. Brown, Z. Chajecki, D. Coupland, H. Iwasaki, M. Kilburn, J. Lee, W. G. Lynch, A. Sanetullaev, M. B. Tsang, J. Winkelbauer, M. Youngs, S. T. Marley, D. V. Shetty, A. H. Wuosmaa, T. K. Ghosh, and M. E. Howard, "Investigations of three-, four-, and five-particle decay channels of levels in light nuclei created using a ^{9}C beam," *Phys. Rev. C*, vol. 84, p. 014320, 2011.

[25] I. A. Egorova, R. J. Charity, L. V. Grigorenko, Z. Chajecki, D. Coupland, J. M. Elson, T. K. Ghosh, M. E. Howard, H. Iwasaki, M. Kilburn, J. Lee, W. G. Lynch, J. Manfredi, S. T. Marley, A. Sanetullaev, R. Shane, D. V. Shetty, L. G. Sobotka, M. B. Tsang, J. Winkelbauer, A. H. Wuosmaa, M. Youngs, and M. V. Zhukov, "Democratic decay of ^{6}Be exposed by correlations," *Phys. Rev. Lett.*, vol. 109, p. 202502, 2012.

[26] L. V. Grigorenko, I. A. Egorova, M. V. Zhukov, R. J. Charity, and K. Miernik, "Two-proton radioactivity and three-body decay. v. improved momentum distributions," *Phys. Rev. C*, vol. 82, p. 014615, 2010.

[27] L. V. Grigorenko, I. A. Egorova, R. J. Charity, and M. V. Zhukov, "Sensitivity of three-body decays to the reactions mechanism and the initial structure by example of ^{6}Be," *Phys. Rev. C*, vol. 86, p. 061602, 2012.

[28] V. I. Goldansky, "On neutron-deficient isotopes of light nuclei and the phenomena of proton and two-proton radioactivity," *Nucl. Phys.*, vol. 19, pp. 482–495, 1960.

[29] S. Zaytsev and G. Gasaneo, "Solving a three-body continuum coulomb problem with quasi-sturmian functions," *J. At. Mol. Sci.*, vol. 4, p. 302, 2013.

[30] C. W. McCurdy, M. Baertschy, and T. N. Rescigno, "Solving the three-body coulomb breakup problem using exterior complex scaling," *Journal of Physics B: Atomic, Molecular and Optical Physics*, vol. 37, no. 17, p. R137, 2004.

[31] L. Hilico, B. Grémaud, T. Jonckheere, N. Billy, and D. Delande, "Quantum three-body coulomb problem in two dimensions," *Phys. Rev. A*, vol. 66, p. 022101, 2002.

[32] S. Kilic, J.-P. Karr, and L. Hilico, "Coulombic and radiative decay rates of the resonances of the exotic molecular ions $pp\mu$, $pp\pi$, $dd\mu$, $dd\pi$, and $dt\mu$," *Phys. Rev. A*, vol. 70, p. 042506, 2004.

[33] J. Madroñero, L. Hilico, B. Grémaud, D. Delande, and A. Buchleitner, "The driven three body coulomb problem," *Mathematical Structures in Computer Science*, vol. 17, pp. 225–246, 2007.

[34] M. J. Ambrosio, L. U. Ancarani, D. M. Mitnik, F. D. Colavecchia, and G. Gasaneo, "A generalized sturmian treatment of (e, 3e) processes described as a three-body coulomb problem," *Few-Body Systems*, 2014.

[35] E. Olsen, M. Pfützner, N. Birge, M. Brown, W. Nazarewicz, and A. Perhac, "Landscape of two-proton radioactivity," *Phys. Rev. Lett.*, vol. 110, p. 222501, 2013.

[36] I. A. Egorova, R. J. Charity, L. V. Grigorenko, Z. Chajecki, D. Coupland, J. M. Elson, T. K. Ghosh, M. E. Howard, H. Iwasaki, M. Kilburn, J. Lee, W. G. Lynch, J. Manfredi, S. T. Marley, A. Sanetullaev, R. Shane, D. V. Shetty, L. G. Sobotka, M. B. Tsang, J. Winkelbauer, A. H. Wuosmaa, M. Youngs, and M. V. Zhukov, "Democratic decay of ^{6}Be exposed by correlations," *Phys. Rev. Lett.*, vol. 109, p. 202502, 2012.

[37] A. Fomichev, V. Chudoba, I. Egorova, S. Ershov, M. Golovkov, A. Gorshkov, V. Gorshkov, L. Grigorenko, G. Kamiski, S. Krupko, I. Mukha, Y. Parfenova, S. Sidorchuk, R. Slepnev, L. Standyo, S. Stepantsov, G. Ter-Akopian, R. Wolski, and M. Zhukov, "Isovector soft dipole mode in ^{6}Be," *Physics Letters B*, vol. 708, no. 12, pp. 6 – 13, 2012.

[38] L. V. Grigorenko, I. A. Egorova, R. J. Charity, and M. V. Zhukov, "Sensitivity of three-body decays to the reactions mechanism and the initial structure by example of ^{6}Be," *Phys. Rev. C*, vol. 86, p. 061602, 2012.

[39] P. Ascher, L. Audirac, N. Adimi, B. Blank, C. Borcea, B. A. Brown, I. Companis, F. Delalee, C. E. Demonchy, F. de Oliveira Santos, J. Giovinazzo, S. Grévy, L. V. Grigorenko, T. Kurtukian-Nieto, S. Leblanc, J.-L. Pedroza, L. Perrot, J. Pibernat, L. Serani, P. C. Srivastava, and J.-C. Thomas, "Direct observation of two protons in the decay of ^{54}Zn," *Phys. Rev. Lett.*, vol. 107, p. 102502, 2011.

[40] K. Miernik, W. Dominik, Z. Janas, M. Pfützner, L. Grigorenko, C. R. Bingham, H. Czyrkowski, M. Cwiok, I. G. Darby, R. Dabrowski, T. Ginter, R. Grzywacz, M. Karny, A. Korgul, W. Kusmierz, S. N. Liddick, M. Rajabali, K. Rykaczewski, and A. Stolz, "Two-proton correlations in the decay of ^{45}Fe," *Phys. Rev. Lett.*, vol. 99, p. 192501, 2007.

[41] L. V. Grigorenko, I. A. Egorova, M. V. Zhukov, R. J. Charity, and K. Miernik, "Two-proton radioactivity and three-body decay. v. improved momentum distributions," *Phys.*

Rev. C, vol. 82, p. 014615, 2010.

[42] R. Holt, B. Zeidman, D. Malbrough, T. Marks, B. Preedom, M. Baker, R. Burman, M. Cooper, R. Heffner, D. Lee, R. Redwine, and J. Spencer, "Pion non-analog double charge exchange: ^{16}O(π^+, π)^{16}Ne," *Physics Letters B*, vol. 69, no. 1, pp. 55 – 57, 1977.

[43] I. Mukha, K. Sümmerer, L. Acosta, M. A. G. Alvarez, E. Casarejos, A. Chatillon, D. Cortina-Gil, I. A. Egorova, J. M. Espino, A. Fomichev, J. E. García-Ramos, H. Geissel, J. Gómez-Camacho, L. Grigorenko, J. Hofmann, O. Kiselev, A. Korsheninnikov, N. Kurz, Y. A. Litvinov, E. Litvinova, I. Martel, C. Nociforo, W. Ott, M. Pfützner, C. Rodríguez-Tajes, E. Roeckl, M. Stanoiu, N. K. Timofeyuk, H. Weick, and P. J. Woods, "Spectroscopy of proton-unbound nuclei by tracking their decay products in-flight: One- and two- proton decays of ^{15}F,^{16}Ne, and ^{19}Na," *Phys. Rev. C*, vol. 82, p. 054315, 2010.

[44] F. Wamers, J. Marganiec, F. Aksouh, Y. Aksyutina, H. Álvarez-Pol, T. Aumann, S. Beceiro-Novo, K. Boretzky, M. J. G. Borge, M. Chartier, A. Chatillon, L. V. Chulkov, D. Cortina-Gil, H. Emling, O. Ershova, L. M. Fraile, H. O. U. Fynbo, D. Galaviz, H. Geissel, M. Heil, D. H. H. Hoffmann, H. T. Johansson, B. Jonson, C. Karagiannis, O. A. Kiselev, J. V. Kratz, R. Kulessa, N. Kurz, C. Langer, M. Lantz, T. Le Bleis, R. Lemmon, Y. A. Litvinov, K. Mahata, C. Müntz, T. Nilsson, C. Nociforo, G. Nyman, W. Ott, V. Panin, S. Paschalis, A. Perea, R. Plag, R. Reifarth, A. Richter, C. Rodriguez-Tajes, D. Rossi, K. Riisager, D. Savran, G. Schrieder, H. Simon, J. Stroth, K. Sümmerer, O. Tengblad, H. Weick, C. Wimmer, and M. V. Zhukov, "First observation of the unbound nucleus ^{15}Ne," *Phys. Rev. Lett.*, vol. 112, p. 132502, 2014.

[45] Y. Kikuchi, T. Matsumoto, K. Minomo, and K. Ogata, "Two neutron decay from the 2^+_1 state of ^{6}He," *Phys. Rev. C*, vol. 88, p. 021602, 2013.

[46] L. V. Grigorenko, I. G. Mukha, and M. V. Zhukov, "Lifetime and fragment correlations for the two-neutron decay of ^{26}**O** ground state," *Phys. Rev. Lett.*, vol. 111, p. 042501, 2013.

[47] K. Hagino and H. Sagawa, "Correlated two-neutron emission in the decay of the unbound nucleus ^{26}O," *Phys. Rev. C*, vol. 89, p. 014331, 2014.

[48] L. V. Grigorenko, I. G. Mukha, I. J. Thompson, and M. V. Zhukov, "Two-proton widths of ^{12}O,^{16}Ne, and three-body mechanism of thomas-ehrman shift," *Phys. Rev. Lett.*, vol. 88, p. 042502, 2002.

[49] L. V. Grigorenko, Y. L. Parfenova, and M. V. Zhukov, "Possibility to study a two-proton halo in ^{17}Ne," *Phys. Rev. C*, vol. 71, p. 051604, 2005.

[50] V. Z. Goldberg, G. G. Chubarian, G. Tabacaru, L. Trache, R. E. Tribble, A. Aprahamian, G. V. Rogachev, B. B. Skorodumov, and X. D. Tang, "Low-lying levels in ^{15}F and the shell model potential for drip-line nuclei," *Phys. Rev. C*, vol. 69, p. 031302, 2004.

[51] D. Gogny, P. Pires, and R. D. Tourreil, "A smooth realistic local nucleon-nucleon force suitable for nuclear hartree-fock calculations," *Physics Letters B*, vol. 32, no. 7, pp. 591 – 595, 1970.

[52] L. V. Grigorenko, R. C. Johnson, I. G. Mukha, I. J. Thompson, and M. V. Zhukov, "Two-proton radioactivity and three-body decay: General problems and theoretical approach," *Phys. Rev. C*, vol. 64, p. 054002, 2001.

[53] A. A. Korsheninnikov, "Analysis of the properties of three-particle decays of nuclei with A=12 and 16 in the K-harmonics method," *Sov. J. Nucl. Phys. (Yad. Fiz.)*, vol. 52, p. 827, 1990.

[54] A. Azhari, R. A. Kryger, and M. Thoennessen, "Decay of the ^{12}O ground state," *Phys. Rev. C*, vol. 58, pp. 2568–2570, 1998.

[55] F. C. Barker, "R-matrix formulas for three-body decay widths," *Phys. Rev. C*, vol. 68, p. 054602, 2003.

[56] H. T. Fortune and R. Sherr, "Width of ^{12}O(g.s.)," *Phys. Rev. C*, vol. 68, p. 034309, 2003.

[57] M. F. Jager, R. J. Charity, J. M. Elson, J. Manfredi, M. H. Mahzoon, L. G. Sobotka, M. McCleskey, R. G. Pizzone, B. T. Roeder, A. Spiridon, E. Simmons, L. Trache, and M. Kurokawa, "Two-proton decay of ^{12}O and its isobaric analog state in ^{12}N," *Phys. Rev. C*, vol. 86, p. 011304, 2012.

[58] M. J. Chromik, P. G. Thirolf, M. Thoennessen, B. A. Brown, T. Davinson, D. Gassmann, P. Heckman, J. Prisciandaro, P. Reiter, E. Tryggestad, and P. J. Woods, "Two-proton spectroscopy of low-lying states in ^{17}Ne," *Phys. Rev. C*, vol. 66, p. 024313, 2002.

[59] L. V. Grigorenko and M. V. Zhukov, "Two-proton radioactivity and three-body decay. iii. integral formulas for decay widths in a simplified semianalytical approach," *Phys. Rev. C*, vol. 76, p. 014008, 2007.

[60] H. T. Fortune, "Constraints on energies of ^{15}F(g.s.), ^{15}O($\frac{1}{2}^+, T = \frac{3}{2}$), and ^{16}F($0^+, T = 2$)," *Phys. Rev. C*, vol. 74, p. 054310, 2006.

[61] F. Q. Guo, J. Powell, D. W. Lee, D. Leitner, M. A. McMahan, D. M. Moltz, J. P. O'Neil, K. Perajarvi, L. Phair, C. A. Ramsey, X. J. Xu, and J. Cerny, "Reexamination of the energy levels of ^{15}F by ^{14}O+^{1}H elastic resonance scattering," *Phys. Rev. C*, vol. 72, p. 034312, 2005.

[62] A. H. Wuosmaa, B. B. Back, S. Baker, B. A. Brown, C. M. Deibel, P. Fallon, C. R. Hoffman, B. P. Kay, H. Y. Lee, J. C. Lighthall, A. O. Macchiavelli, S. T. Marley, R. C.

Pardo, K. E. Rehm, J. P. Schiffer, D. V. Shetty, and M. Wiedeking, "$^{15}\mathbf{C}(d,p)^{16}\mathbf{C}$ reaction and exotic behavior in $^{16}\mathbf{C}$," *Phys. Rev. Lett.*, vol. 105, p. 132501, 2010.

[63] L. V. Grigorenko, T. A. Golubkova, and M. V. Zhukov, "Thomas-ehrman effect in a three-body model: The ^{16}Ne case," *Phys. Rev. C*, vol. 91, p. 024325, 2015.

[64] L. V. Grigorenko and M. V. Zhukov, "Two-proton radioactivity and three-body decay. IV. Connection to quasiclassical formulation," *Phys. Rev. C*, vol. 76, p. 014009, 2007.

[65] K. Ogawa, H. Nakada, S. Hino, and R. Motegi, "Thomas-ehrman shifts in nuclei around ^{16}O and role of residual nuclear interaction," *Physics Letters B*, vol. 464, no. 3-4, pp. 157 – 163, 1999.

[66] J. Marganiec, F. Wamers, F. Aksouh, Y. Aksyutina, H. lvarez Pol, T. Aumann, S. Beceiro-Novo, K. Boretzky, M. Borge, M. Chartier, A. Chatillon, L. Chulkov, D. Cortina-Gil, H. Emling, O. Ershova, L. Fraile, H. Fynbo, D. Galaviz, H. Geissel, M. Heil, D. Hoffmann, J. Hoffmann, H. Johansson, B. Jonson, C. Karagiannis, O. Kiselev, J. Kratz, R. Kulessa, N. Kurz, C. Langer, M. Lantz, T. Le Bleis, R. Lemmon, Y. Litvinov, K. Mahata, C. Mntz, T. Nilsson, C. Nociforo, G. Nyman, W. Ott, V. Panin, S. Paschalis, A. Perea, R. Plag, R. Reifarth, A. Richter, C. Rodriguez-Tajes, D. Rossi, K. Riisager, D. Savran, G. Schrieder, H. Simon, J. Stroth, K. Smmerer, O. Tengblad, H. Weick, M. Wiescher, C. Wimmer, and M. Zhukov, "Studies of continuum states in ^{16}Ne using three-body correlation techniques," *The European Physical Journal A*, vol. 51, no. 1, 2015.

[67] M. Wang, G. Audi, A. Wapstra, F. Kondev, M. MacCormick, X. Xu, and B. Pfeiffer, "The AME2012 atomic mass evaluation," *Chinese Physics C*, vol. 36, no. 12, p. 1603, 2012.

[68] W. Benenson and E. Kashy, "Isobaric quartets in nuclei," *Rev. Mod. Phys.*, vol. 51, pp. 527–540, 1979.

[69] Y. H. Lam, B. Blank, N. A. Smirnova, J. B. Bueb, and M. S. Antony, "The isobaric multiplet mass equation for revisited," *Atomic Data and Nuclear Data Tables*, vol. 99, no. 6, pp. 680 – 703, 2013.

[70] A. M. Lane and R. G. Thomas, "R-matrix theory of nuclear reactions," *Rev. Mod. Phys*, vol. 30, p. 257, 1958.

[71] G. Presser, R. Bass, and K. Krüger, "The reactions ^{6}Li(n, p) ^{6}He(0) and ^{6}Li(n, n') ^{6}Li(3.56)," *Nuclear Physics A*, vol. 131, no. 3, pp. 679 – 697, 1969.

[72] C. Détraz, J. Cerny, and R. H. Pehl, "Observation of $t = \frac{3}{2}$ levels in ^{7}Li-^{7}Be and the uncharacterized nuclei ^{7}He, ^{7}B, and ^{8}He," *Phys. Rev. Lett.*, vol. 14, pp. 708–710, 1965.

[73] R. L. McGrath, J. Cerny, and E. Norbeck, "Unbound nuclide ^{7}B," *Phys. Rev. Lett.*, vol. 19, pp. 1442–1444, 1967.

[74] W. D. Harrison, "Structure of ^{7}Be: (ii). the ^{6}Li(p, p)^{6}Li and ^{4}He(^{3}He, p)^{6}Li reactions," *Nuclear Physics A*, vol. 92, no. 2, pp. 260 – 272, 1967.

[75] H. Brunnader, J. C. Hardy, and J. Cerny, "Carbon-10 and mass measurements for light nuclei," *Phys. Rev.*, vol. 174, pp. 1247–1249, 1968.

[76] R. Sherr and G. Bertsch, "Coulomb energy systematics and the missing $J^{\pi}= (1/2)^{+}$ state in ^{9}B," *Phys. Rev. C*, vol. 32, pp. 1809–1816, 1985.

[77] F. C. Barker, "The first excited state of ^{9}B," *Aust. J. Phys*, vol. 40, p. 307, 1987.

[78] I. A. Egorova, R. J. Charity, L. V. Grigorenko, Z. Chajecki, D. Coupland, J. M. Elson, T. K. Ghosh, M. E. Howard, H. Iwasaki, M. Kilburn, J. Lee, W. G. Lynch, J. Manfredi, S. T. Marley, A. Sanetullaev, R. Shane, D. V. Shetty, L. G. Sobotka, M. B. Tsang, J. Winkelbauer, A. H. Wuosmaa, M. Youngs, and M. V. Zhukov, "Democratic decay of ^{6}Be exposed by correlations," *Phys. Rev. Lett.*, vol. 109, p. 202502, 2012.

[79] J. F. Ziegler, J. P. Biersack, and U. Littmark, *The Stopping and Range of Ions in Solids*. New York: Pergamon Press, 1985. The code SRIM can be found at www.srim.org.

[80] R. Anne, J. Herault, R. Bimbot, H. Gauvin, C. Bastin, and F. Hubert, "Multiple angular scattering of heavy ions (^{16,17}O, ^{40}Ar, ^{86}Kr and ^{100}Mo) at intermediate energies (20-90 mev/u).," *Nucl. Instrum. Methods B*, vol. 34, p. 295, 1988.

[81] R. B. Wiringa, V. G. J. Stoks, and R. Schiavilla, "Accurate nucleon-nucleon potential with charge-independence breaking," *Phys. Rev. C*, vol. 51, pp. 38–51, 1995.

[82] R. B. Wiringa. private communication.

[83] B. S. Pudliner, V. R. Pandharipande, J. Carlson, and R. B. Wiringa, "Quantum monte carlo calculations of $A \leq 6$ nuclei," *Phys. Rev. Lett.*, vol. 74, pp. 4396–4399, 1995.

[84] B. A. Brown and W. D. Rae, "Nushell@msu," tech. rep., MSU NSCL, 2007.

[85] S. Cohen and D. Kurath, "Effective interactions for the *1p* shell.," *Nuclear Physics*, vol. 73, p. 1, 1965.

[86] S. Cohen and D. Kurath, "Spectroscopic factors for the 1p shell," *Nuclear Physics A*, vol. 101, no. 1, pp. 1 – 16, 1967.

[87] K. W. Brown, W. W. Buhro, R. J. Charity, J. M. Elson, W. Reviol, L. G. Sobotka, Z. Chajecki, W. G. Lynch, J. Manfredi, R. Shane, R. H. Showalter, M. B. Tsang, D. Weisshaar, J. R. Winkelbauer, S. Bedoor, and A. H. Wuosmaa, "Two-proton decay from the isobaric analog state in ^{8}B," *Phys. Rev. C*, vol. 90, p. 027304, 2014.

[88] M. MacCormick and G. Audi, "Evaluated experimental isobaric analogue states from to and associated {IMME} coefficients," *Nuclear Physics A*, vol. 925, no. 0, pp. 61 – 95, 2014.

[89] W. Benenson and E. Kashy, "First excited A = 9 isospin quartet," *Phys. Rev. C*, vol. 10, pp. 2633–2635, 1974.

[90] K. M. Nollett, "*Ab initio* calculations of nuclear widths via an integral relation," *Phys. Rev. C*, vol. 86, p. 044330, 2012.

[91] N. K. Timofeyuk, "Widths of low-lying nucleon resonances in light nuclei in the source-term approach," *Phys. Rev. C*, vol. 92, p. 034330, 2015.

[92] M. S. Golovkov, V. Z. Goldberg, L. S. Danelyan, V. I. Dukhanov, I. L. Kuleshov, A. E. Pakhomov, I. N. Serikov, V. A. Timofeev, and V. N. Unezhev, "Population of states of the nuclei ^{9}B and ^{13}O in the (^{3}He, ^{6}He) reaction," *Yad.Fiz.*, vol. 53, p. 888, 1991.

[93] Z. Elekes, Z. Dombrdi, R. Kanungo, H. Baba, Z. Flp, J. Gibelin, . Horvth, E. Ideguchi, Y. Ichikawa, N. Iwasa, H. Iwasaki, S. Kanno, S. Kawai, Y. Kondo, T. Motobayashi, M. Notani, T. Ohnishi, A. Ozawa, H. Sakurai, S. Shimoura, E. Takeshita, S. Takeuchi, I. Tanihata, Y. Togano, C. Wu, Y. Yamaguchi, Y. Yanagisawa, A. Yoshida, and K. Yoshida, "Low-lying excited states in ^{17,19}C," *Physics Letters B*, vol. 614, no. 34, pp. 174 – 180, 2005.

[94] J. Tian, N. Wang, C. Li, and J. Li, "Improved kelson-garvey mass relations for proton-rich nuclei," *Phys. Rev. C*, vol. 87, p. 014313, 2013.

[95] H. G. Bohlen, R. Kalpakchieva, W. von Oertzen, T. N. Massey, A. A. Ogloblin, G. de Angelis, M. Milin, C. Schulz, T. Kokalova, and C. Wheldon, "Spectroscopy of ^{17}C and $(sd)^3$ structures in heavy carbon isotopes," *The European Physical Journal A*, vol. 31, no. 3, pp. 279–302, 2007.

[96] V. Guimarães, S. Kubono, N. Ikeda, I. Katayama, T. Nomura, M. H. Tanaka, Y. Fuchi, H. Kawashima, S. Kato, H. Toyokawa, C. C. Yun, T. Niizeki, T. Kubo, M. Ohura, and M. Hosaka, "Nuclear structure of ^{17}Ne by the three-neutron pickup (^{3}He,^{6}He) reaction," *Phys. Rev. C*, vol. 58, pp. 116–126, 1998.

[97] M. J. Chromik, P. G. Thirolf, M. Thoennessen, B. A. Brown, T. Davinson, D. Gassmann, P. Heckman, J. Prisciandaro, P. Reiter, E. Tryggestad, and P. J. Woods, "Two-proton spectroscopy of low-lying states in ^{17}Ne," *Phys. Rev. C*, vol. 66, p. 024313, 2002.

[98] J. Manfredi, R. J. Charity, K. Mercurio, R. Shane, L. G. Sobotka, A. H. Wuosmaa, A. Banu, L. Trache, and R. E. Tribble, "α decay of the excited states in ^{12}C at 7.65 and 9.64 mev," *Phys. Rev. C*, vol. 85, p. 037603, 2012.